

DESIGN, MODELING AND CONTROL OF A HYBRID UAV

A THESIS SUBMITTED TO
THE GRADUATE SCHOOL OF NATURAL AND APPLIED SCIENCES
OF
MIDDLE EAST TECHNICAL UNIVERSITY

BY

ABDURRAHİM MURATOĞLU

IN PARTIAL FULFILLMENT OF THE REQUIREMENTS
FOR
THE DEGREE OF MASTER OF SCIENCE
IN
AEROSPACE ENGINEERING

SEPTEMBER 2019

Approval of the thesis:

DESIGN, MODELING AND CONTROL OF A HYBRID UAV

submitted by **ABDURRAHİM MURATOĞLU** in partial fulfillment of the requirements for the degree of **Master of Science in Aerospace Engineering Department, Middle East Technical University** by,

Prof. Dr. Halil Kalıpçılar
Dean, Graduate School of **Natural and Applied Sciences**

Prof. Dr. İsmail H. Tuncer
Head of Department, **Aerospace Engineering**

Prof. Dr. Ozan Tekinalp
Supervisor, **Aerospace Engineering, METU**

Examining Committee Members:

Prof. Dr. Dilek Funda Kurtuluş
Aerospace Engineering, METU

Prof. Dr. Ozan Tekinalp
Aerospace Engineering, METU

Prof. Dr. Coşku Kasnakoğlu
Electrical and Electronics Engineering, TOBB ETU

Assoc. Prof. Dr. İlkay Yavrucuk
Aerospace Engineering, METU

Assist. Prof. Dr. Ali Türker Kutay
Aerospace Engineering, METU

Date: 11.09.2019

I hereby declare that all information in this document has been obtained and presented in accordance with academic rules and ethical conduct. I also declare that, as required by these rules and conduct, I have fully cited and referenced all material and results that are not original to this work.

Name, Surname: Abdurrahim Muratođlu

Signature:

ABSTRACT

DESIGN, MODELING AND CONTROL OF A HYBRID UAV

Muratođlu, Abdurrahim
Master of Science, Aerospace Engineering
Supervisor: Prof. Dr. Ozan Tekinalp

September 2019, 129 pages

Vertical takeoff and landing (VTOL) vehicles that can fly like conventional airplanes after the takeoff, provide a promising area to find applications in the future. These hybrid vehicles combine the advantages of rotary-wing and fixed-wing aircraft configurations such as having capability of hovering flight, takeoff and landing without utilizing a runway, long range, high speed flight with reasonable endurance. In this study, a tilt-rotor tricopter VTOL UAV having a conventional fixed-wing airframe is designed. Nonlinear mathematical model of the vehicle is generated by calculating propulsive and aerodynamics-based equations of motion. For a better approximation, dynamic model of the propulsion system is obtained by performing wind tunnel experiments. Moreover, the nonlinear system is linearized at suitable trim conditions for stability analysis and to develop linear controllers. Flight simulations were performed with the developed linear controllers in MATLAB/Simulink. Simulation results have been reported and the results were discussed.

Keywords: UAV, VTOL, Tilt-rotor, Tricopter, Flight Control

ÖZ

HİBRİT HAVA ARACININ TASARIMI, MODELLENMESİ VE KONTROLÜ

Muratođlu, Abdurrahim
Yüksek Lisans, Havacılık ve Uzay Mühendisliđi
Tez Danışmanı: Prof. Dr. Ozan Tekinalp

Eylül 2019, 129 sayfa

Dikine inen ve kalkan (DİK) ve sonrasında konvansiyonel uçaklar gibi uçabilen araçlar, ileride uygulama alanı bulması için önemli bir alandır. Bu tarz melez araçlar, döner kanatlı ve sabit kanatlı araçların sahip olduđu havada sabit durabilme, piste ihtiyaç duymadan iniş kalkış yapabilme, yüksek hız, uzun uçuş süresi ve geniş menzil üstünlüklerini bir araya getirmektedir. Bu tezde, bir konvansiyonel sabit kanatlı çatkılı, yatar rotorlu trikopter DİK İHA tasarlanmıştır. İtkisel ve aerodinamik tabanlı hareket denklemleri hesaplanarak aracın doğrusal olmayan matematiksel modeli oluşturulmuştur. İtki sisteminin dinamik modeli rüzgar tüneli deneyleri ile ortaya çıkarılmıştır. Sonrasında, bu doğrusaldışı model, kararlılık analizi ve doğrusal kontrolcü geliştirilmesi amacıyla, uygun trim noktalarında doğrusallaştırılmıştır. MATLAB/Simulink ortamında, geliştirilen doğrusal kontrolcülerle birlikte uçuş benzetimleri gerçekleştirilmiştir, sonuçları sunulmuştur.

Anahtar Kelimeler: İHA, DİK, Yatar-rotor, Trikopter, Uçuş Kontrolü

To my beloved family

ACKNOWLEDGEMENTS

I would like to express my deepest gratitude to my supervisor Prof. Dr. Ozan Tekinalp for his support, guidance, advice, criticism, encouragements and insights throughout the research. Similarly, I would like to thank to Asst. Prof. Dr. Ali Türker Kutay for his support, and invaluable remarks.

I am grateful to my colleagues Ali Tefvik Büyükkoçak, Süleyman Altınışik, Derya Kaya, Metehan Yayla, Heyecan Utke Koyuncuoğlu, Ömer Ataş and Özcan Yırtıcı for their precious comments and helps.

I wish specially thank to Saffet Gökuç for his supports, guidance and helps throughout design, production and flight tests of the UAV subjected to this thesis. I also thank to Emir Koca, Ercan Öztürk, Eren Ünal, Kerim Erdem Alp, Oğuzhan Aydın, Denizcan Elçi, Emre Saylam and Ahmet Uyar for their helps throughout the production of the UAV. I also would like to thank Alpay Demircan.

Last and most, I would like to thank my beloved mother, father and siblings for everything they have done in my whole life. Likewise, to my valuable brother Abdullah, for his supports throughout the study. Especially, I would like to thank my dear wife Elif who supported and motivated me all the time.

TABLE OF CONTENTS

ABSTRACT	v
ÖZ	vi
ACKNOWLEDGEMENTS	viii
TABLE OF CONTENTS	ix
LIST OF TABLES	xiii
LIST OF FIGURES	xv
LIST OF ABBREVIATIONS	xix
LIST OF SYMBOLS	xx
CHAPTERS	
1. INTRODUCTION	1
1.1 Motivation	1
1.2 Literature Review	2
1.2.1 Airframe Configurations	2
1.2.2 Tilt-rotor Control Methodologies.....	10
1.3 Contributions	11
1.4 Outline	12
2. DESIGN OF THE HYBRID UAV	13
2.1 Propulsion Geometry	13
2.2 Wing and Tail Geometry	14
2.3 Airfoil Selection	15
2.4 Wing and Tail Sizing.....	18
2.5 Fuselage Design	22

2.6	Propulsion Choice	23
2.7	Rotor Placement	23
2.8	Control Surface Sizing	24
2.9	Design Parameters	25
3.	THEORY AND MODELING	29
3.1	Reference Frames and Coordinate Systems	29
3.1.1	Inertial Reference Frame \mathbf{F}_I (Inertial Axes, $O_I X_I Y_I Z_I$)	29
3.1.2	Earth-Fixed Reference Frame \mathbf{F}_E (Earth Axes, $O_E X_E Y_E Z_E$)	30
3.1.3	Vehicle-Carried Reference Frame \mathbf{F}_V (Axes, $O_V x_V y_V z_V$)	31
3.1.4	Air-Trajectory Reference Frame \mathbf{F}_W (Wind Axes, $O_W x_W y_W z_W$)	31
3.1.5	Body-Fixed Reference Frame \mathbf{F}_B (Body Axes, $O_B x_B y_B z_B$)	32
3.1.6	Stability Axes \mathbf{F}_S ($O_S x_S y_S z_S$)	33
3.2	Attitude Parametrization	33
3.2.1	Euler Angles (ϕ, θ, ψ)	33
3.2.2	Transformation via Euler Angles	34
3.3	Equations of Motion	37
3.4	Mathematical Model of Multirotor Module	41
3.4.1	Propulsion Model	41
3.4.2	Multirotor (Propulsive) Model	51
3.5	Mathematical Model of Fixed-Wing Module	55
3.5.1	Sign Conventions	55
3.5.2	Aerodynamic Simulation of the Fixed-Wing Model	57

3.5.3	Aerodynamic Coefficients	60
3.5.4	Aerodynamic Control Derivatives	63
3.5.5	Nondimensional and Dimensional Stability Derivatives	64
3.6	Combining Multicopter and Fixed-Wing Models	67
3.7	Throttle Model and Actuator Models	68
4.	TRIMMING, LINEARIZATION AND STABILITY ANALYSIS	69
4.1	Trimming	69
4.2	Linearization	71
4.2.1	Linear Model of Multicopter	74
4.2.2	Linear Model of Fixed-Wing Module	76
4.3	Stability Analysis	77
4.3.1	Multicopter Module	77
4.3.2	Fixed-Wing Module	78
4.3.2.1	Short Period and Roll Mode Approximations	79
5.	CONTROL OF THE VEHICLE	81
5.1	Concepts of Operations	81
5.2	Controllability and Observability	83
5.3	Controller Design	83
5.3.1	Proportional – Derivative (PD) Controller	84
5.3.2	Linear Quadratic Regulator (LQR) Controller	86
5.3.3	Linear Quadratic Tracker (LQT) Controller	88
5.4	Actuation Calculation	89
5.4.1	Control Mixing	91
5.5	Gain Scheduling	93

5.6	Simulation Results	94
5.6.1	Multicopter Flight Simulations.....	95
5.6.2	Fixed-Wing Flight Simulations	102
5.6.3	Transition Flight Simulations	107
6.	CONCLUSION.....	113
	REFERENCES	115
	APPENDICES	
A.	Flight Testing	125

LIST OF TABLES

TABLES

Table 1.1. Comparison of the UAV configurations	4
Table 2.1. Standard atmosphere table for altitudes of 0 and 1000 m.....	16
Table 2.2. Geometric and Sizing parameters	25
Table 2.3. Mass budget of the aerial vehicle.....	26
Table 3.1. Experimental data of a propulsion system (a motor and a propeller pair)	42
Table 3.2. Measurement data of motor-propeller supplied by the manufacturer.....	43
Table 3.3. Measurement parameters of wind tunnel experiment.....	46
Table 3.4. Variation of measurement parameters for 7000 rpm at 90° tilt case.....	50
Table 3.5. Effect of control surfaces on the vehicle attitude.....	56
Table 3.6. Simulation conditions for variable ranges	58
Table 3.7. Variation of aerodynamic coefficients with respect to variables.....	61
Table 3.8. Values of calculated aerodynamic control derivatives	64
Table 3.9. Nondimensional longitudinal derivatives	65
Table 3.10. Nondimensional lateral derivatives.....	65
Table 3.11. Nondimensional stability derivatives of longitudinal parameters.....	65
Table 3.12. Nondimensional stability derivatives of lateral parameters.....	66
Table 4.1. Predetermined state parameters in trim condition.....	70
Table 4.2. Predetermined control variables in trim condition.....	70
Table 4.3. Trim variables for flight modes	70
Table 4.4. Transfer functions of tricopter with respect to force inputs.....	77
Table 4.5. Transfer functions of tricopter with respect to moment inputs.....	78
Table 4.6. Longitudinal characteristics of fixed-wing module of the vehicle	78
Table 4.7. Dutch-roll mode characteristics of the fixed-wing module	79
Table 4.8. Roll and spiral mode characteristics of the fixed-wing module.....	79
Table 5.1. Tuned gain parameters for tricopter.....	85
Table 5.2. Tuned gain parameters for fixed-wing aircraft	85
Table 5.3. Controller gains of multicopter module for $0 < \delta_i < 10$	93

Table 5.4. Controller gains of fixed-wing module for $0 < \delta_i < 10$	93
Table 5.5. Controller gains of multicopter module for $10 < \delta_i < 20$	93
Table 5.6. Controller gains of fixed-wing module for $10 < \delta_i < 20$	93

LIST OF FIGURES

FIGURES

Figure 1.1. Various classes of UAVs; a) <i>fixed-wing, airplane (TAI, Anka)</i> [4] b) <i>fixed-wing, airplane (Dassault, Neuron)</i> [5] c) <i>rotary-wing, helicopter (NG, MQ-8B)</i> [6] d) <i>rotary wing, tandem rotors (DPI, DP-14 Hawk)</i> [7] e) <i>rotary wing, quadrotor (DJI, Phantom-3)</i> [8] f) <i>flapping-wing, bird (Festo, Smartbird)</i> [9] g) <i>hybrid (Korean Air – KARI, TR-60)</i> [10] h) <i>LTA Blimp (NG, LEMV)</i> [11].....	3
Figure 1.2. Examples of hybrid UAVs; a) <i>tail-sitter (Aerovel, Flexrotor)</i> [12] b) <i>dual-system (Arcturus, Jump-20)</i> [13] c) <i>tilt-wing (NASA, GL-10)</i> [14] d) <i>tilt-rotor (Bell, Eagle Eye)</i> [15]	5
Figure 1.3. Tilt-rotor UAVs; a) <i>Bell, Eagle Eye</i> [31] b) <i>KARI, TR-100</i> [32]	7
Figure 1.4. Tilt-rotor and coaxial ducted fan airframes; a) <i>TURAC</i> [40] b) <i>Y4TR</i> [41].....	8
Figure 1.5. All coaxial tilt-rotor: <i>FireFly6</i> [42]	8
Figure 1.6. Tilt-rotor configurations; a) <i>Tri-tilt-rotor (Papachristos et al.)</i> [47] b) <i>Önen's configuration</i> [48]	9
Figure 1.7. Dual tilt-rotor hybrid tricopter designs; a) <i>Orange Hawk</i> [55] b) <i>Design of Chao et al.</i> [56] c) <i>Proposal of Monterroso</i> [57]	10
Figure 2.1. Rotor configuration of tricopter	14
Figure 2.2. Configuration layout of hybrid aerial vehicle.....	15
Figure 2.3. Airfoil geometries of Clark-Y (upper) and NACA 2412.....	17
Figure 2.4. C_l and C_l/C_d versus α comparison at $Re=340.000$	17
Figure 2.5. Airfoil geometry of NACA 0012.....	18
Figure 2.6. C_l and C_l/C_d versus α curves of NACA 0012 at $Re=340.000$	18
Figure 2.7. Wing-tail geometry and sizing	21
Figure 2.8. Bottom and side view of the fuselage.....	22
Figure 2.9. A 3D view of the fuselage	22
Figure 2.10. Configuration layout with rotor settlement.....	24
Figure 2.11. Illustration of control surfaces placed on wing and tail.....	25

Figure 2.12. The final view of the designed vehicle in a CAD software	27
Figure 2.13. The view of the hybrid vehicle after the construction.....	27
Figure 3.1. Earth-fixed and Earth-centered reference frame	30
Figure 3.2. Illustration of vehicle-carried reference frame	31
Figure 3.3. Illustration of air-trajectory reference frame	32
Figure 3.4. Illustration of body-fixed reference frame	32
Figure 3.5. Illustration of stability axes	33
Figure 3.6. Force and moment vectors given in body-fixed reference frame.....	37
Figure 3.7. Thrust value generated by the propulsion system	42
Figure 3.8. Torque value generated by the propulsion system	43
Figure 3.9. Produced thrust data by manufacturer and load cell measurement	44
Figure 3.10. Produced torque data by manufacturer and load cell measurement.....	44
Figure 3.11. Experimental setup and its orientation in the wind tunnel with 30° tilt angle (case a and b) and 90° (case c) tilt angle	46
Figure 3.12. The wind tunnel used for the measurements [82]	47
Figure 3.13. Produced net thrust vs wind speed for different rpm values at 0° tilt ...	48
Figure 3.14. Produced net thrust vs wind speed for different rpm values at 30° tilt .	48
Figure 3.15. Produced net thrust vs wind speed for different rpm values at 60° tilt .	49
Figure 3.16. Produced net thrust vs wind speed for different rpm values at 90° tilt .	49
Figure 3.17. Illustration of a propulsion system (a single motor-propeller pair)	51
Figure 3.18. Tricopter configuration	52
Figure 3.19. Top and front view with sizing parameters	52
Figure 3.20. Altitude and attitude motion control	53
Figure 3.21. Propulsive model (tilt-rotor tricopter) of the hybrid UAV	54
Figure 3.22. Convention for angle of attack and sideslip angle	55
Figure 3.23. Sign convention for control surface deflections.....	56
Figure 3.24. 3D mesh view of the wing, horizontal and vertical tails	59
Figure 3.25. 3D view of the XFLR5 model with produced lift and streamlines (with $\alpha = 10^\circ$ assigned).....	59

Figure 3.26. (a) C_X and (b) C_L versus α and β with no control surface deflection..	62
Figure 3.27. (a) C_Y and (b) C_M versus α and β with no control surface deflection	62
Figure 3.28. (a) C_Z and (b) C_N versus α and β with no control surface deflection.	63
Figure 3.29. Aerodynamic model of Fixed-wing module.....	66
Figure 3.30. Mathematical nonlinear model of the hybrid UAV	67
Figure 3.31. Experimental throttle data and fitted curve	68
Figure 5.1. System block diagram	84
Figure 5.2. System block diagram with a PD controller for a control channel.....	84
Figure 5.3. System diagram with LQR controller.....	87
Figure 5.4. System Diagram with LQT.....	88
Figure 5.5. Control mixing by using control effectiveness factor.....	92
Figure 5.6. Simulation block diagram.....	94
Figure 5.7. Roll reference response with PD controller.....	96
Figure 5.8. Rotor rpms and tilt angles in roll response with PD controller	96
Figure 5.9. Pitch reference response with PD controller	97
Figure 5.10. Rotor rpms and tilt angles in pitch response with PD controller.....	97
Figure 5.11. Yaw reference response with PD controller	98
Figure 5.12. Rotor rpms and tilt angles in yaw response with PD controller	98
Figure 5.13. Altitude reference response with PD controller.....	99
Figure 5.14. Rotor rpms and tilt angles in altitude response with PD controller.....	99
Figure 5.15. Roll reference response for PD, LQR and LQT controllers	100
Figure 5.16. Pitch reference response for PD, LQR and LQT controllers.....	100
Figure 5.17. Yaw reference response for PD, LQR and LQT controllers	101
Figure 5.18. Altitude ref. response for PD, LQR and LQT controllers	101
Figure 5.19. Forward flight simulation with no propulsion with PD controllers.....	102
Figure 5.20. Forward flight simulation with no propulsion with PD controllers.....	103
Figure 5.21. Roll response with no propulsion with PD controllers.....	104
Figure 5.22. Roll response with no propulsion with PD controllers.....	105
Figure 5.23. Pitch response with no propulsion with PD controllers	106

Figure 5.24. Pitch response with no propulsion with PD controllers	106
Figure 5.25. Attitude and altitude results for forward transition	108
Figure 5.26. Position and velocity results for forward transition	108
Figure 5.27. Actuator and aerodynamic angle results for forward transition	109
Figure 5.28. Attitude and altitude results for back-transition.....	110
Figure 5.29. Position and velocity results for back-transition.....	110
Figure 5.30. Actuator and aerodynamic angle results for back-transition.....	111
Figure A.1. Flight path of the performed flight test	126
Figure A.2. Altitude data	126
Figure A.3. Roll angle variation	127
Figure A.4. Pitch angle variation.....	127
Figure A.5. Yaw angle variation.....	127
Figure A.6. Data for the position in body z-axis	128
Figure A.7. Variation of velocity in inertial axes	128
Figure A.8. Variation of airspeed	128
Figure A.9. Pilot control commands sent by a remote controller.....	129
Figure A.10. Pictures from flight test	129

LIST OF ABBREVIATIONS

ABBREVIATIONS

A/C	Aircraft
R/C	Remote Controlled
PID	Proportional-Integrator-Derivative
LQR	Linear Quadratic Regulator
LQT	Linear Quadratic Tracker
UAV	Unmanned Aerial Vehicle
VTOL	Vertical Takeoff and Landing
FW	Fixed-Wing
AR	Aspect Ratio
HT	Horizontal Tail
VT	Vertical Tail
DoF	Degrees of Freedom
NED	North-East-Down
2D	2-Dimensional
3D	3-Dimensional
CFD	Computational Fluid Dynamics
VLM	Vortex-Lattice Method
rpm	Rotations per Minute
c.g.	Center of Gravity
EoM	Equations of Motion

LIST OF SYMBOLS

SYMBOLS

g	Gravitational acceleration
m	Vehicle mass
I_{xx}, I_{yy}, I_{zz}	Moments of inertia about (x, y, z) axes
I_{xy}, I_{yz}, I_{xz}	Products of inertia
W	Weight of the vehicle
S	Reference wing area
b	Span of the vehicle
c, \bar{c}	Chord length of wing, mean aerodynamic chord
c_r, c_t	Lengths of root and tip chords
λ	Taper ratio
V_{HT}, V_{VT}	Volume ratios of horizontal and vertical tails
l_{HT}, l_{VT}	Moment arms of horizontal and vertical tails
h_{HT}	Height of vertical tail
F_I, F_E	Inertial and earth-fixed reference frames
F_V, F_W	Vehicle-carried and air-trajectory reference frames
F_B, F_S	Body-fixed and stability reference frames
L_{BV}	Transformation matrix from F_V to F_B
I_B	Inertia matrix in F_B
α, β	Aerodynamic angles, angle of attack and sideslip angle
φ, θ, ψ	Euler angles (roll, pitch, yaw)
$\delta_a, \delta_e, \delta_r$	Deflection angles of aileron, elevator and rudder
δ	Differential tilt angles of front rotors
δ_t	Mean tilt angle of front rotors
δ_1, δ_2	Tilt angles of first and second front rotors
Ω	Rotor RPM

x_E, y_E, z_E	Coordinates of c.g. of the vehicle relative to f_e
ρ	Air density
\mathbf{V}	Airspeed vector of c.g. of the vehicle
$\boldsymbol{\omega}$	Angular velocity vector about c.g. of the vehicle
u, v, w	Scalar components of \mathbf{V} in F_B
p, q, r	Scalar components of $\boldsymbol{\omega}$ in F_B
T	Force produced by a rotor
Q	Torque produced by a rotor
k_f, k_t	Force and torque coefficients of a rotor
\mathbf{F}	Resultant force vector acting on c.g. of the aerial vehicle
\mathbf{G}	Resultant moment vector acting on c.g. of the aerial vehicle
X_A, Y_A, Z_A	Aerodynamic forces in F_B
L_A, M_A, N_A	Aerodynamic moments in F_B
X_P, Y_P, Z_P	Propulsive forces in F_B
L_P, M_P, N_P	Propulsive moments in F_B
F_x, F_y, F_z	Scalar components of \mathbf{F} in F_B
M_x, M_y, M_z	Scalar components of \mathbf{G} in F_B
C_X, C_Y, C_Z	Nondimensional drag, side and lift force coefficients in F_B
C_l, C_m, C_n	Nondimensional roll, pitch and yaw moment coefficients in F_B
$C_{X\alpha}$	Stability derivative, $\partial C_X / \partial \alpha$
$C_{l\beta}$	Stability derivative, $\partial C_l / \partial \beta$
$C_{m\delta_e}$	Control derivative, $\partial C_m / \partial \delta_e$
\mathbf{x}, \mathbf{u}	State vector and control input vector
$\mathbf{A}, \mathbf{B}, \mathbf{C}, \mathbf{D}$	State-space matrices of linear system
\mathbf{K}	State feedback gain matrix
K_p, K_d	Proportional and derivative gains of a PID controller
\mathbf{Q}, \mathbf{R}	Weighting matrices

CHAPTER 1

INTRODUCTION

The main scope of this thesis is to design, develop and control a novel hybrid Unmanned Aerial Vehicle (UAV), a tilt-rotor tricopter with a conventional fixed wing airframe configuration, which can takeoff and land vertically and fly like an airplane.

In this chapter, the motivation of the study is presented. Literature review for both airframe configurations and control systems, indicating the previous studies and progresses performed in this field have been outlined. Contributions of the thesis is provided and the chapter is concluded with the thesis outline.

1.1 Motivation

Today, drones have taken their parts in daily life and in the society, surveillance and military applications. Drones are fascinating aerial robots that can handle a variety of tasks and thus, attracted a great research interest and investments. Various kinds of UAVs are designed, produced and used. Commonly existing configurations are Horizontal Takeoff and Landing (HTOL) and Vertical Takeoff and Landing (VTOL) as like being in aviation world, conventional aircrafts and helicopters have irreplaceable position. The two configurations have different flight characteristics, advantages and disadvantages. Thus, combining these configurations will bring forth some benefits. Extended flight range, increased flight speed, takeoff without a runway need and hover flight capability are some of the benefits. Therefore, hybrid vehicles became one of the major studies and research areas in aviation sector. The hybrid UAV technologies still need to be thrived and improved.

There are various configurations of hybrid UAVs such as, dual system, tilt-wing and tilt-rotor configurations. Each has its own characteristics due to the structural, aerodynamic and propulsive difference in configurations. Tilt-rotor VTOL UAVs can be accounted more advantageous over the others, for instance, they are more weight efficient because the tilting rotors are used in all flight phases unlike the dual systems. Additionally, aerodynamically and structurally they can be more efficient in VTOL and hovering flight phases due to not tilting the wings. Because of the above-mentioned specialties, tilt-rotor VTOL UAVs sound reasonable to keep research on them.

1.2 Literature Review

1.2.1 Airframe Configurations

Unmanned Aerial Vehicles (UAV) have been popular, after the aviation age has started, especially in the past several decades. It is desired and advantageous to take the human factor away from the aerial vehicles. Especially taking away death and injury risks, simplifying and reducing costs of construction, operation and maintenance, miniaturizing sizes, diversifying usage area are some of the advantages of aerial vehicles. The advancements in the technology especially in electronics and sensor technology has improved the UAV technologies, and they started to play a bigger role in daily life. Mapping, surveying, search and rescue, communication, transportation, meteorology, agriculture and filming are some of the civil-commercial areas of usage [1]. Surveillance, spying, marking, bombing target hitting practicing can be given as several examples of security-military applications.

Depending on the nature of the mission, configurations of aircrafts change, in other words, some configurations of the aircrafts are not suitable for specific missions [2]. For example, for observatory hovering flights, helicopters, for high speed and long-range flights, airplanes are needed. UAVs may be categorized under, fixed-wing,

rotary-wing, flapping-wing, lighter than air (LTA), and hybrid configurations [1]. There are also other types of UAVs that is not suitable to be classified under the specified configurations. Various classes of UAVs have been illustrated in Figure 1.1.

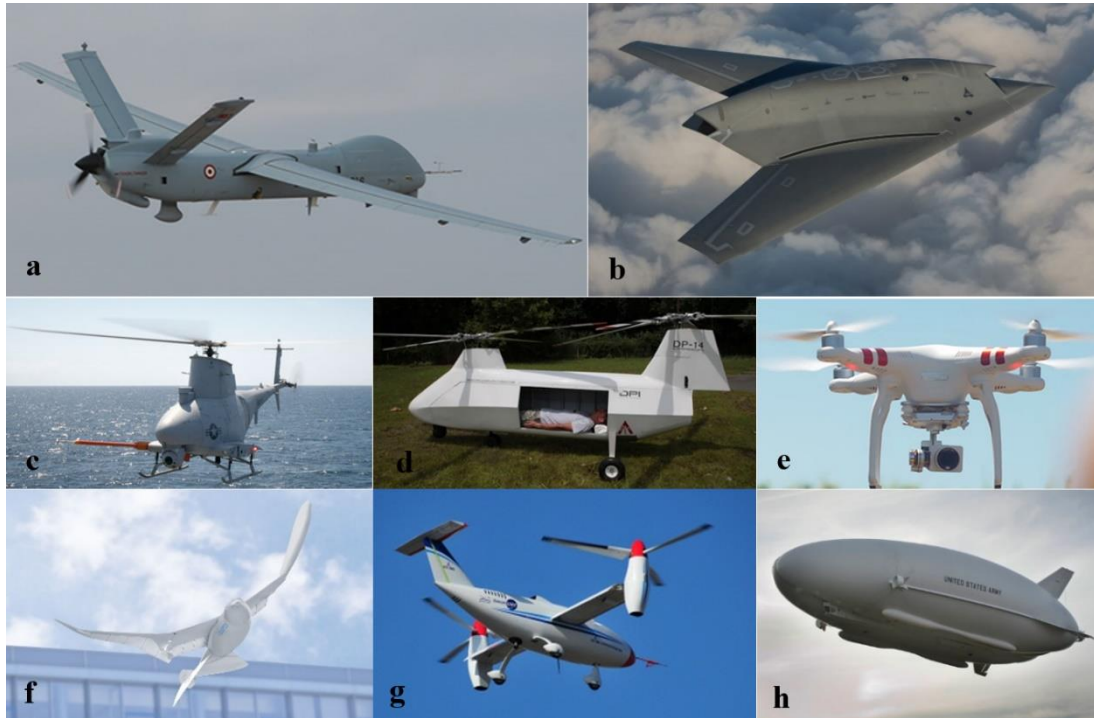
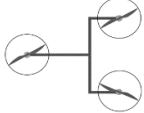


Figure 1.1. Various classes of UAVs; **a)** fixed-wing, airplane (TAI, Anka) [4] **b)** fixed-wing, airplane (Dassault, Neuron) [5] **c)** rotary-wing, helicopter (NG, MQ-8B) [6] **d)** rotary wing, tandem rotors (DPI, DP-14 Hawk) [7] **e)** rotary wing, quadrotor (DJI, Phantom-3) [8] **f)** flapping-wing, bird (Festo, Smartbird) [9] **g)** hybrid (Korean Air – KARI, TR-60) [10] **h)** LTA Blimp (NG, LEMV) [11]

Each class of configuration inherently has its own advantages and disadvantages due to structural, aerodynamic, propulsive and stability characteristics. Fixed-wing aerial vehicles can fly further with high speeds, and increased payload capacities. They are more controllable due to stable flight characteristics. But they also need to have sufficient amount of horizontal velocity to provide required vertical lift force. This means a runway or special launching systems (not very applicable for large

dimensions) which increases operating and maintenance costs. On the other side, rotary-wing aerial vehicles are highly maneuverable and capable of hover flights which are especially needed at the runway absence and at usages and transportations of urban areas. Unfortunately, they don't have the specified abilities of the fixed-wing aerial vehicles. By developing hybrid UAVs, the disadvantages of rotary and fixed-wing classes can be eliminated and advantages of them can be combined together. In Table 1.1, the comparison of some characteristics of fixed-wing, rotary-wing and hybrid configurations were summarized.

Table 1.1. Comparison of the UAV configurations [1,3]

Capabilities	Fixed-Wing 	Rotary-Wing 	Hybrid Vehicle 
Range	Long	Short	Long
Endurance	High	Short	High
Speed	High	Low	Medium – High
Stability	Stable	Unstable	Depends on Flight Mode
Maneuverability	Low	High	Depends on Flight Mode
Hover	Cannot	Can	Can
Runway	Needed	No Need	No Need

As seen in the Table 1.1, Hybrid UAVs (or fixed-wing VTOL) piece together the benefits of the rotary-wing and fixed-wing vehicles, hence increase the mission capabilities and extends the range of functionalities. Drop-off and pick-up of payloads, hovering surveillance, operations over rugged terrains, planetary observations like Martian observation missions and many other conditions necessitate bypassing runway requirement, which raises the significance of the hybrid aerial vehicles that also have long range, high endurance and speedy flight capabilities. Thus, they attract and keep the attention for decades and many studies have been made on this field.

Numerous conceptual designs of hybrid configurations were developed, produced and operated. Hybrid UAVs can be categorized under tail-sitter, dual-systems, tilt-wing, tilt-rotor configurations [4]. In Figure 1.2 examples of the indicated configurations are shown.

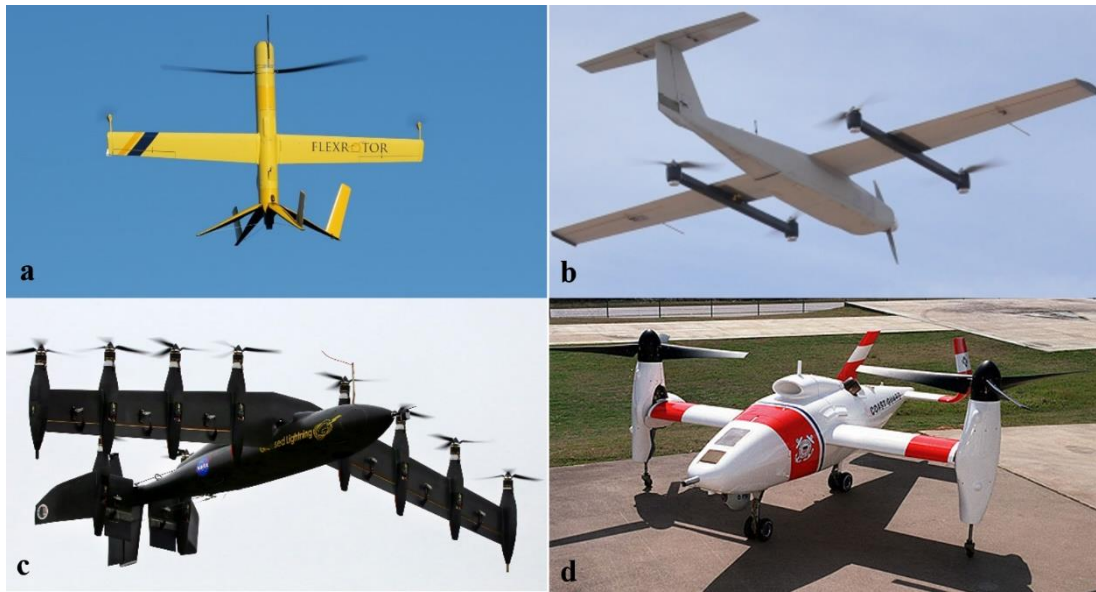


Figure 1.2. Examples of hybrid UAVs; **a**) tail-sitter (*Aerovel, Flexrotor*) [12] **b**) dual-system (*Arcturus, Jump-20*) [13] **c**) tilt-wing (*NASA, GL-10*) [14] **d**) tilt-rotor (*Bell, Eagle Eye*) [15]

Tail-sitter vehicles have fixed wing and tail module carrying out the takeoff and landing, simply by sitting on their tail supplying vertical thrust with single or multiple propellers or ducted fans that mounted in the body X direction. They have a simpler mechanical design since they don't need actuators to rotate the rotors or wings but they perform transition by tilting the bodies. This provides convenience in weight, mechanics and structure [16]. However, they are more delicate to wind gusts and crosswinds since the body, wings and tail are more exposed to horizontally blowing wind. Also, transition and control are the challenges that encountered. Zhao and Bil [17] presented a VTOL ducted fan tail-sitter UAV, Matsumoto et al. [18] proposed a tail-sitter design with a single propeller, Kubo [19] proposed a design with counter-

rotating twin propeller, Hochstenbach and Notteboom [20] presented a quadcopter tail-sitter design.

Dual-system configuration has fixed propellers that supply vertical lift and horizontal thrust/push. A quadrotor combined with a pusher/tractor propeller fixed-wing UAV is the most common example that is seen. They have easier transition phase due to simultaneously applicable vertical and horizontal forces. However, since the lifting systems are only used in vertical takeoff and landing phase, they turn into useless load in cruising flight mode causing extra drag, weight and more energy consumption [16]. Latitude HQ, Hybrid Quadrotor Technology [21], SkyPowler 2, VTOL transformer UAV [22] and ALTI Transition [23] are good examples of hybrid UAVs of quadrotor with fixed-wing body configuration, in the market.

Tilt-wing UAVs have tilting wings together with the mounted multiple rotors. Again, like tail-sitter configurations, they are sensitive to wind in VTOL mode since the wings are tilted upward. But they have better aerodynamic characteristics in VTOL and transition phases compared to tilt-rotors, since the downwash effect of the rotors are minimized by rotor-wing combination [24]. HARVee [25] and AVIGLE [26] are examples of tilt-wing VTOL UAVs with conventional airplane airframe (one pair of wings), SUAVI [27] and QTW VTOL UAV [28] are examples of tandem tilt-wing UAV configuration.

Tilt-rotor configurations take an important part in hybrid VTOL UAVs and many research studies have been made about them. They use tilt-rotors to supply lift in vertical flight mode and thrust in cruising flight mode. Transition is performed by tilting the rotors at a desired rate. Tilt-rotors can be mainly categorized as dual rotors and multi rotors. In dual tilt-rotor configurations, there are two tilting rotors which commonly placed at the wingtips. Due to position of rotors and tilting mechanisms, the wings must be structurally enduring, thus shorter in span and lower in aspect ratio [16]. Also, since the rotors are placed over the wings there is an interference caused by blockage of the wings to the flow stream of the propeller [24]. Due to these

challenges, in the perspective of aerodynamics, stability and controllability dual tilt-rotors can be counted disadvantageous compared to multi tilt-rotor hybrid systems. Bell Eagle Eye [29] and KARI TR-100 and its scaled version TR-60 dual tilt-rotor hybrid UAVs [30], have been illustrated in Figure 1.3.

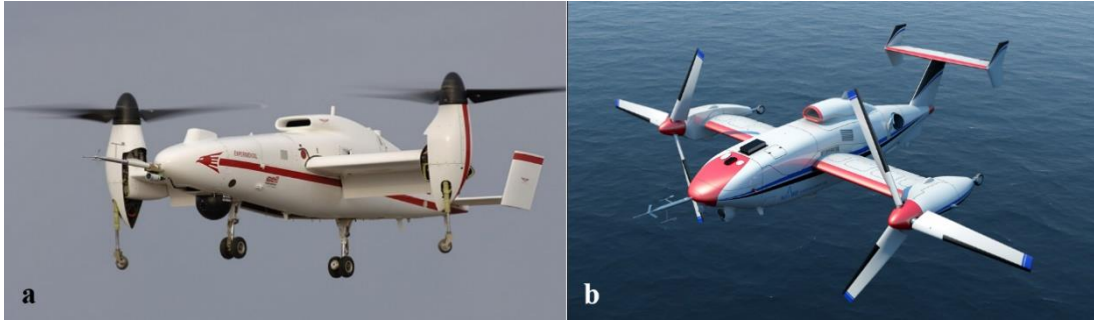


Figure 1.3. Tilt-rotor UAVs; *a) Bell, Eagle Eye [31] b) KARI, TR-100 [32]*

By using a rear propeller in addition to dual propellers at the front, the center of gravity could be placed between lifting rotors and then the stability and control of the aerial vehicle could be increased in vertical flight mode [33]. Also, this case allows the dual propellers to be placed ahead of the wings and to be prevented the rotor-wing interference. However, increasing the rotors at the back of the aerial vehicles like quadrotors etc. will increase weight and drag in horizontal flight mode.

In case of odd number of rotors, there will be a resultant yaw moment due to reaction torque of uncompensated rotation of the rotors. This can be prevented by using either coaxial counter-rotating rotors at the rear, or by doubling all the three propellers. Also, by inserting tilting mechanism to the rear rotor or by using differential tilt of the front two rotors yawing moment can be controlled. Examples of all the four cases exist in the literature. Özdemir et al. [34-36] designed a UAV called TURAÇ with two front tilting propellers and a larger and fixed coaxial ducted fan at the back. The design has wing-body configuration. Also, Collins presented very similar design for Martian exploration missions [37-38]. BirdEyeView Aerobotics company developed a Y6

configuration with 3 coaxial rotors, 6 in total, where the two pairs in the front tilts (dependently, i.e. tilting angle is same for both pairs) and the one at the back is fixed. This also has wing-body configuration [39]. In Figure 1.4 and Figure 1.5 coaxial tilt-rotor configurations and all coaxial tilt-rotor configurations are shown.

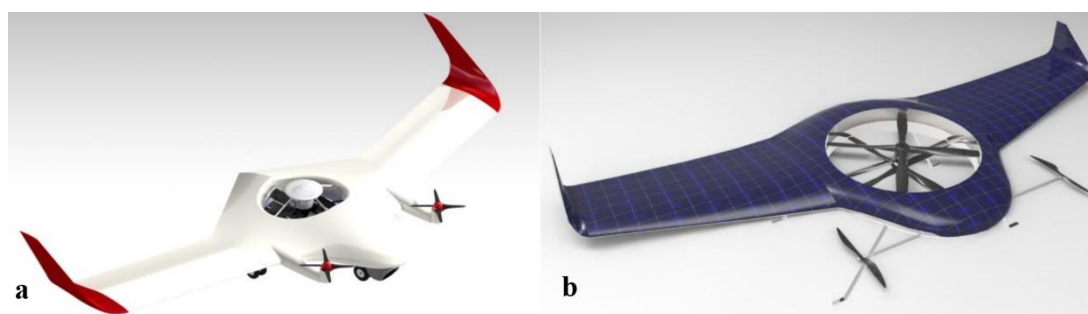


Figure 1.4. Tilt-rotor and coaxial ducted fan airframes; *a) TURAC* [40] *b) Y4TR* [41]



Figure 1.5. All coaxial tilt-rotor: *FireFly6* [42]

Hybrid aerial vehicle researches are also conducted in the Middle East Technical University (METU). Armutcuoğlu et al. [43] proposed ducted tilting propellers at the front and another fixed ducted propeller structured to the fuselage at the aft. The tilting mechanism of the ducted propellers at wingtips is driven together dependently. The yaw motion in vertical flight is controlled by thrust vectoring the ducted aft propeller. The design has conventional fixed-wing airplane configuration. Önen et al. [44,45] developed a hybrid tricopter with dependently tilting two front rotors and another tilting rotor at the back to control yaw motion in vertical flight mode. The UAV has a fixed-wing with inverted V-tail configuration. Also, Papachristos et al. [46] developed

a similar design with three tilt-rotors where all the rotors have tilting capability. In Figure 1.6, the works of Papachristos and Önen with tricopter configurations is presented.

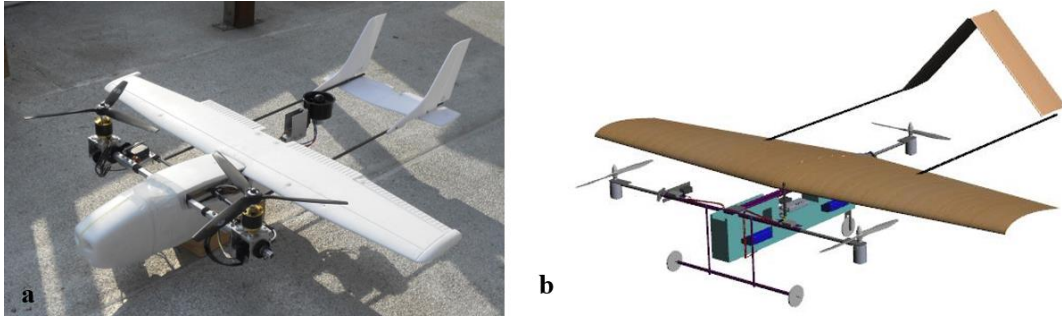


Figure 1.6. Tilt-rotor configurations; *a) Tri-tilt-rotor (Papachristos et al.) [47]*
b) Önen's configuration [48]

Finally, the researches on the configuration with two independently tilting rotors in the front and a fixed rotor at the back are as the following. IAI Panther and Mini Panther UAVs have front independently tilting rotor systems and another fixed rotor with a specific angle at the back. It has a body of fixed-wing with H-tail configuration [49,50]. The Orange Hawk project developed by S. Carlson, has two front tilt-rotors and a fixed rotor at the back directed upward with 10 degrees of tilt towards to nose of the vehicle. The design is equipped with a wing-body airframe [51]. Finally, Chao et al. [50,52] proposed the same propulsive configuration with a fixed-wing and H-tail airframe. Later on, it has come to be known that Monterroso [53] had come up with same concept, with the design of Chao et al. [50,52]. On the other hand, Ta et al. [54] and Summers [3] proposed similar tilt-rotor tricopter with a conventional airframe configuration but they only focused on longitudinal flight characteristics. In Figure 1.7 tilt-rotor tricopter hybrid vehicles were illustrated.

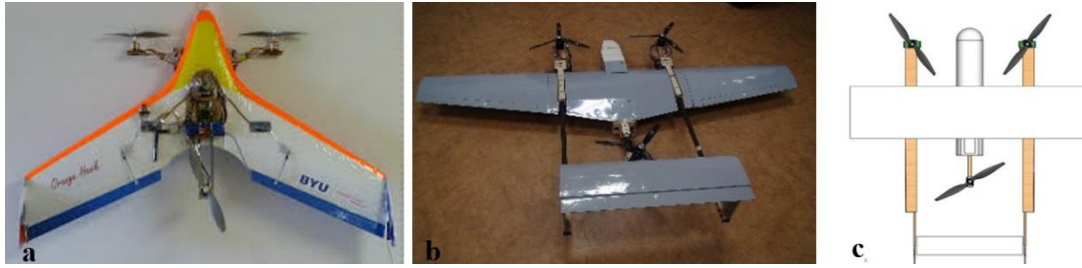


Figure 1.7. Dual tilt-rotor hybrid tricopter designs; **a)** *Orange Hawk* [55] **b)** *Design of Chao et al.* [56] **c)** *Proposal of Monterroso* [57]

1.2.2 Tilt-rotor Control Methodologies

Hybrid UAV dynamics are governed by nonlinear equations of motion, especially in hovering multi-rotor and transition modes the vehicle dynamics are inherently unstable. Thus, feedback controllers must be used to stabilize the system [58]. Both linear and nonlinear controllers are studied and implemented in the literature. Nonlinear controllers comprise a broader range of operation thus give a better response at different operating points such as disturbances and various state parameters. But since the need to very accurate nonlinear dynamical model and since their design and stability analysis are more tedious than linear controllers, the linear controllers are more preferred in practical applications [24]. The linear controllers are sufficient around the operating point of the linearized system. However, tilt-rotor hybrid UAVs have three different operation phases, hovering, transitioning and cruising, and since the trim conditions are different for the three cases, a single linear controller cannot stabilize the whole vehicle dynamics [16]. To solve this problem, a nonlinear controller can be used or gain scheduling between different linear controllers can be provided.

Backstepping, sliding mode, nonlinear dynamic model inversion and gain scheduling are among the **nonlinear control** techniques of tilt-rotor / tilt-wing UAVs. Some group of researchers, at University of Technology of Compiègne developed a backstepping controller [59], at Indian Institute of Technology designed a

backstepping based PD controller [60,61] for dual tilt-rotor UAVs and another group at University of Technology of Compiè presented a backstepping controller based on Lyapunov design for a quad tilt-rotor UAV [62]. A sliding mode controller is presented for quad tilt-wing UAV at Sabancı University by Öner et al. [63] and dynamic model inversion controller designed and proposed for tilt-rotor UAVs at Gyeongsang National University and at Beihang University [64,65]. Finally, Sato et al. [66,67] at Japan Aerospace Exploration Agency, Papachristos et al. [68] at University of Patras and ETH Zurich, Hernandez-Garcia [69] and Summers [3] presented gain scheduling controllers for tilting hybrid UAVs.

Proportional Integral Derivative (PID) and Linear Quadratic Regulator (LQR) are commonly used linear controllers in tilt-rotor UAV researches. Papachristos et al. implemented PID controller to a dual tilt-rotor [70] and to a tri tilt-rotor [71] UAVs. Also, Çetinsoy et al. [72] developed a PID controller for quad tilt-wing UAV. For the LQR controller, Öner et al. [73] presented it for the vertical flight for quad tilt-wing UAV, Önen [44] developed it for vertical flight of a tilt-rotor tri-copter UAV, Papachristos et al. [74] demonstrated it for their tri tilt-rotor UAV again in vertical flight mode.

The dual-tilt-rotor tri-copter configurations with a fixed wing airframe has a few examples and studied only by classical PID controllers. Transitioning between hovering flight and cruising flight modes is not elaborated. Thus, this topic is still need to be further studied.

1.3 Contributions

The contributions of this thesis may be presented as:

- A novel tilt-rotor hybrid UAV is designed and developed which has a wide flight characteristics and capabilities relative to rotary-wing and fixed-wing UAVs.

- A specific fixed-wing airplane is designed to extract its mathematical model to work on flight control algorithms and to have a test vehicle to validate developed flight control algorithms
- Mathematical model of the hybrid vehicle is derived
- Dynamical model of propulsion system is derived by performing wind tunnel experiments corresponding to varying wind speeds
- Various controllers are designed for different flight modes of the vehicle.
- Control mixer is proposed that distribute the controls through actuators in.

1.4 Outline

In Chapter, introduction through UAVs and VTOL concepts are addressed. A literature review on UAVs and hybrid UAVs, airframes and control techniques that are used in hybrid vehicles are provided.

In Chapter 2, the design process of the hybrid UAV is put forward including geometry and airfoil selection, wing and tail sizing, fuselage design, propulsion choice and rotor settlement.

In Chapter 3, some theoretical information and methodology over related topics that used through the study of the thesis is given. A full mathematical nonlinear model of the hybrid UAV is derived.

In Chapter 4, the trimming and linearization of the model is performed in order to analyze the stability and to develop linear controllers.

In Chapter 5, various controllers are developed for the simulation of the system. PD, LQR and LQT controllers are proposed. Control mixer that distributing the control commands over the actuators is provided. Simulation results on the developed nonlinear mathematical model with the designed control systems are given. The comments and observations on provided results are mentioned.

In Chapter 6, conclusion remarks and future studies are presented.

CHAPTER 2

DESIGN OF THE HYBRID UAV

In this chapter, design process of the hybrid UAV is presented to be extracted and analyzed its mathematical nonlinear and linear models. Configuration selection, wing tail, fuselage design, sizing and positioning, rotor selection and placement are reported. Control surfaces are specified. Finally, all the mass, geometric and design parameters are reported.

2.1 Propulsion Geometry

One of the purposes of this thesis is to design and develop a hybrid UAV having a tilt-rotor configuration. Tilt-rotor VTOL UAVs have some advantages over other configurations such as better transition phase characteristics compared to tail-sitter vehicles, reduced unused actuator number in either hovering or cruising flight modes as regards dual-system UAVs and better structural and aerodynamic properties compared to tilt-wing configurations as explained in Chapter 1.

Different types of tilt-rotor UAVs are available regarding to its rotor number and type. Dual-rotor, tri-rotor, quad-rotor, hexa-rotor with either single or coaxial rotors are examples of tilt-rotor configuration. Again, tri-rotor configuration is chosen since, it has reduced number of actuators which provides lower drag, less weight and energy consumption compared to other multi-rotor UAVs, also, provides much better stability and structural advantage and thus better aerodynamic characteristics compared to dual-rotor UAVs. In short, a tri-copter configuration having two independently tilting rotors in the front and another fixed one at the rear is chosen. Considering the rotors fall into the corners of an isosceles triangular the c.g. of the tri-copter is at the median of the triangle. The tri-copter is illustrated in Figure 2.1.

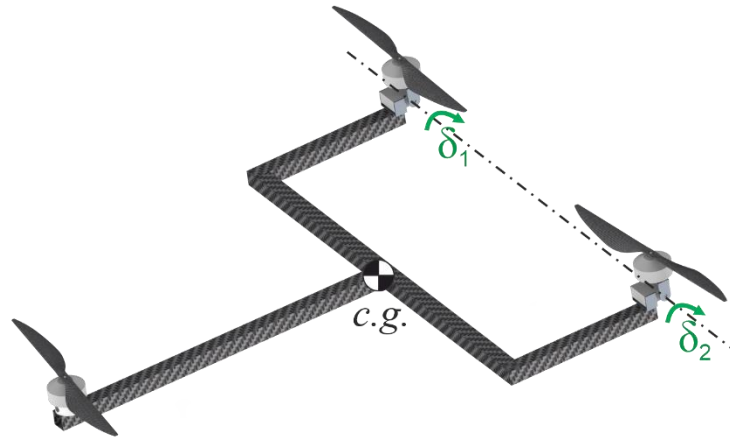


Figure 2.1. Rotor configuration of tricopter

2.2 Wing and Tail Geometry

Since this vehicle is not designed for a specific mission and it is an experimental study that aiming to extract a mathematical model, validate simulations and work on control and stability of the vehicle, it is not an optimal design in terms of aerodynamics, weight and energy consumption. It is desired to design an easy-to-produce UAV. Thus, the wing is selected as rectangular type, unswept and untapered, with no dihedral and twist, which is easier to make calculations, design and production. In addition, the wing is decided to be high wing, due to the propellers have enough ground clearance and it is a more stable configuration in lateral motion [75]. Also, the UAV can take off and land on its fuselage. A conventional type of tail with rectangular horizontal part, has been specified which provides adequate stability and control having light weight, simple geometry and easy production [76].

After specifying the propulsive configuration, a conventional monoplane airplane module is specified to be used. A standard fixed-wing airplane is easy to design and construct. It has also no examples with tilt-rotor tricopter configuration to the best of our knowledge. Placing tilt-rotors at the tip of the wings causes to use lower wing

span, aspect ratio and thicker airfoil selection thus, causing poor structural and aerodynamic characteristics. Also, moment arm for roll motion becomes increased and during a vertical landing the vehicle possesses possible dangers such as striking propellers to ground. Therefore, front tilt-rotors are specified to be set on beams ahead of wings at both sides of the fuselage. A conceptual design is shown in Figure 2.2.

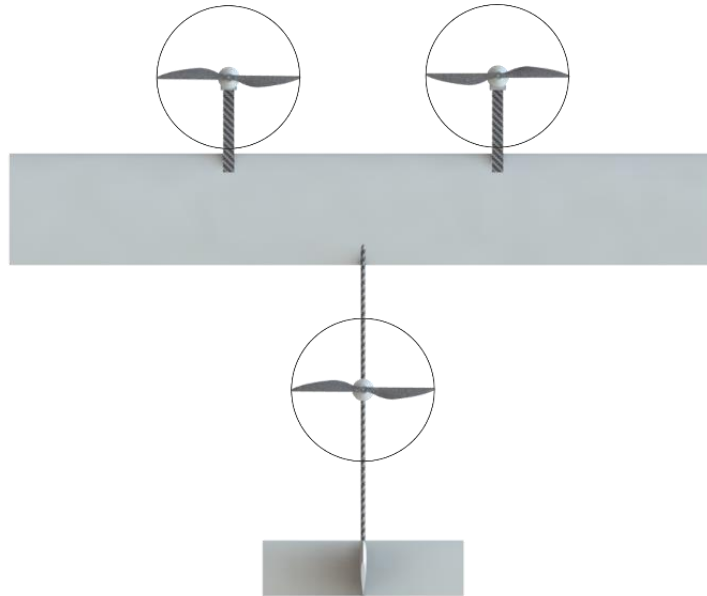


Figure 2.2. Configuration layout of hybrid aerial vehicle

2.3 Airfoil Selection

Airfoil selection process is an important step in which the thickness ratio (affecting the structural strength) drag, weight, stall characteristics (especially at high angle of attack flights) lift to drag ratio, etc. parameters effects the overall aerodynamic performance. Airfoil selection depends on the mission requirements and flight envelope of the aerial vehicle as well. The designed UAV will have a low speed cruising flight around 17–19 m/s. To calculate Reynolds number range for Ankara (altitude is nearly 1000 m), the parameters of standard atmosphere table is used which is shown in Table 2.1.

Table 2.1. Standard atmosphere table for altitudes of 0 and 1000 m

Altitude (m)	Density, ρ (kg/m ³)	Dynamic Viscosity, μ (kg/m.s)
0	1.225	1.789×10^{-5}
1000	1.112	1.758×10^{-5}

$$Re = \frac{\rho V \bar{c}}{\mu} \quad (2.1)$$

$$V_{stall} = 10 \text{ m/s}, V_{cruise} = 17 - 19 \text{ m/s}, \bar{c} = 0.3 \text{ m}$$

Using the given Reynolds number formula and above-specified velocities for 0.3 m chord length, Reynolds number range is calculated approximately between 320.000 – 360.000. Numerous airfoils were analyzed for the specified Reynolds number range and the analysis is constrained on two final airfoils, NACA2412 and Clark-Y. In low Reynolds number range, NACA2412 and Clark-Y are good examples of airfoils and commonly used on R/C airplanes. Normalized Clark-Y and NACA 2412 airfoils are shown in Figure 2.3. 2D aerodynamic data of airfoils are obtained by using XFLR5 software. XFLR5 is an extensively used software for low Reynolds number airfoil analyzes which is based on XFOIL algorithm. Also, XFOIL analyzes potential flow around airfoils by combining a panel method and an integral boundary layer formulation. The algorithm provides pretty accurate results at low Reynolds number and its accuracy is well accepted [77]. The airfoil analyzes were performed at $Re=340.000$ as an average value for the proposed cruising flight speed.

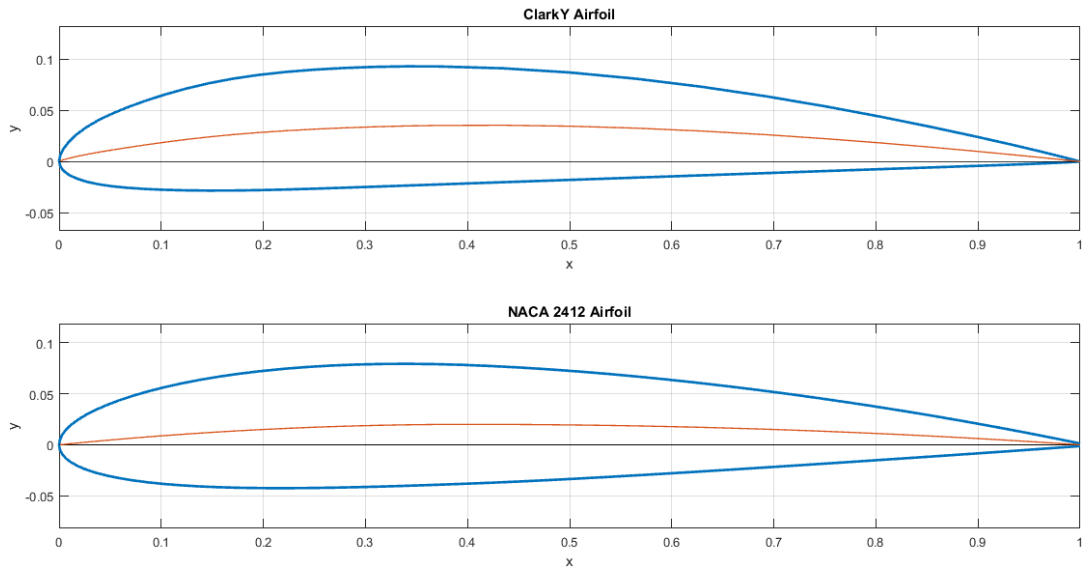


Figure 2.3. Airfoil geometries of Clark-Y (upper) and NACA 2412

Comparatively, both airfoils have quite similar thickness ratio, but Clark-Y has slightly higher lift coefficient (C_l) and lift to drag ratio (C_l/C_d). The C_l and C_l/C_d comparison of the airfoils are shown in Figure 2.4. As seen in C_l vs α plot, Clark-Y has a better and flatter stall characteristic. In addition, it is also a flat-bottom airfoil that helps to ease the wing construction [78]. Thus, Clark-Y airfoil is selected to be employed in the wing design process.

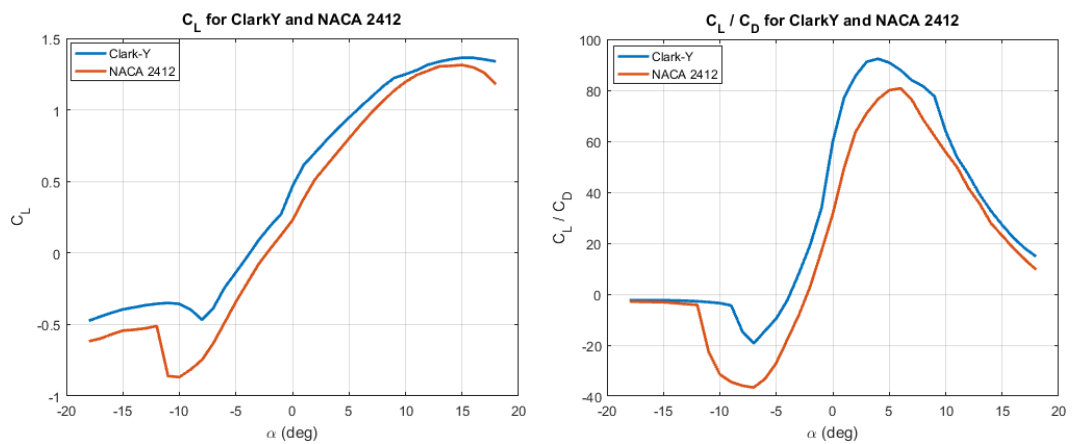


Figure 2.4. C_l and C_l/C_d versus α comparison at $Re=340.000$

Additionally, for the horizontal and vertical tails, a thin (12% maximum thickness at 30% of chord) symmetrical NACA 0012 airfoil is decided to be used owing to its similar thickness ratio. Because tail thickness ratio is usually similar to wing thickness ratio in low speed aircrafts [76]. The normalized airfoil geometry, C_l and C_l/C_d plots are given in Figures 2.5 and 2.6.

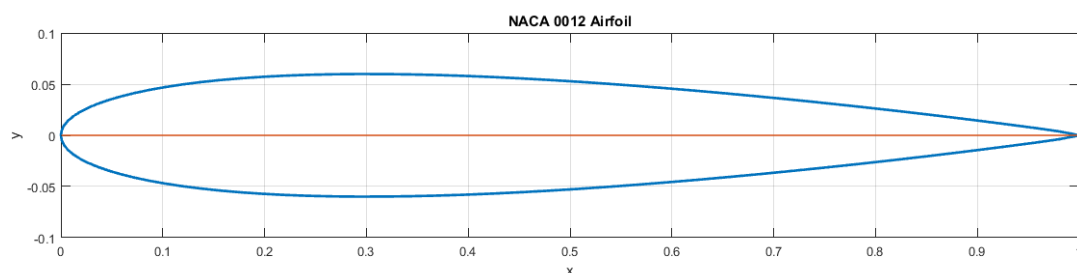


Figure 2.5. Airfoil geometry of NACA 0012

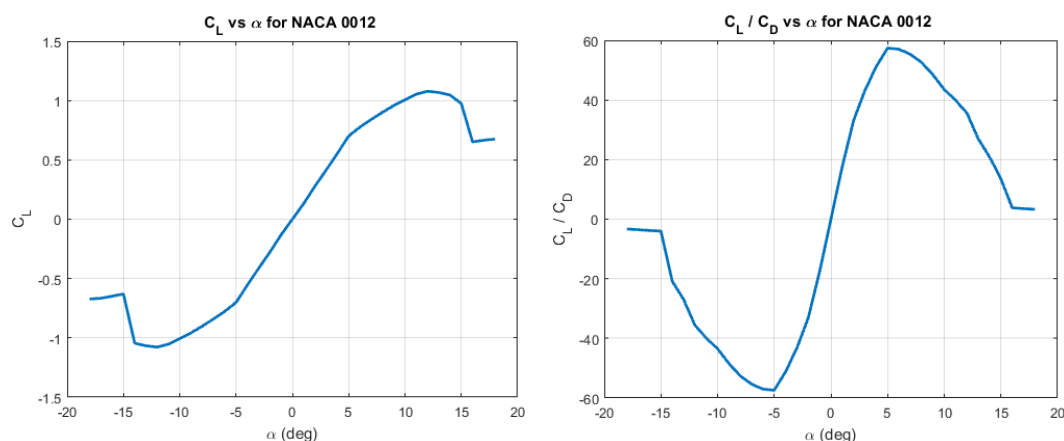


Figure 2.6. C_l and C_l/C_d versus α curves of NACA 0012 at $Re=340.000$

2.4 Wing and Tail Sizing

According to the SHT-IHA regulations of Directorate General of Civil Aviation (DGCA), UAVs weighting between 0.5 kg and 4 kg are categorized under class IHA0 and have more flexible operational constraints. Thus, estimated and the desired maximum takeoff weight is specified to be 4 kg.

The reference wing area will be determined by using estimated stall speed and maximum lift coefficient. Required maximum lift coefficient is calculated for stall angle. Some of lift coefficient and predetermined speed parameters are as follows.

$$C_{l_{\alpha=2^\circ}} \cong 0.7 \quad \text{and} \quad C_{l_{\max}} \cong 1.37 \quad \text{at} \quad \text{Re}=340.000$$

$$V_{\text{cruise}} = 18 \text{ m/s} \quad \text{and} \quad V_{\text{stall}} = 10 \text{ m/s}$$

The maximum lift coefficient of a clean (no flaps) and unswept wing (3D) will usually be 90% of its airfoil's maximum lift as obtained by the 2D airfoil data at similar Reynolds number [75,86].

Assuming 3D effects, the lift coefficient of the wing may be calculated as:

$$C_{L_{\max}} = 0.9 \times C_{l_{\max}} \quad (2.2)$$

and

$$C_{L_{\max}} = 0.9 \times 1.37 = 1.233 \quad (2.3)$$

The required minimum reference wing area is determined as:

$$S_{\min} = \frac{W}{\frac{1}{2} \rho V_{\text{stall}}^2 C_{L_{\max}}} \cong 0.58 \text{ m}^2 \quad (2.4)$$

For a rectangular wing and predetermined 0.3 m chord length, the wing span is calculated as:

$$b_{\text{Wing}} = \frac{S}{c_{\text{Wing}}} = \frac{0.58 \text{ m}^2}{0.3 \text{ m}} \cong 1.94 \text{ m} \quad (2.5)$$

Subsequently, the aspect ratio (AR) of the wing is calculated to be:

$$AR_{\text{Wing}} = \frac{b_{\text{Wing}}^2}{S} \cong 6.45 \quad (2.6)$$

It is a pretty average choice for a hybrid UAV in terms of structural and aerodynamic requirements. Higher AR values would cause longer wing span, resulting harder

control in hover flight mode causing the vehicle to expose more side winds. On the other hand, less AR values, would cause poor aerodynamics in cruising flight mode. Also, wing incidence angle is selected to be 2 degrees which is an option for most initial design work, and general aviation and homebuilt aircrafts [76].

For the horizontal and vertical tails, the design parameters are as follows. Horizontal and vertical tail volume ratios selected between ratios of sailplane and homebuilt aircrafts, from the provided Table 4.3 in the reference [76]:

$$V_{HT} = 0.55 \quad \text{and} \quad V_{VT} = 0.025$$

Considering the propeller settlement areas, the moment arms of the tails are:

$$l_{HT} = 1.07 \text{ m} \quad \text{and} \quad l_{VT} = 1.1 \text{ m}$$

Using the following formula, the tail sizing may be calculated as:

$$S_{HT} = \frac{V_{HT} \times S}{l_{HT} / c_{wing}} \cong 0.09 \text{ m}^2 \quad (2.7)$$

$$S_{VT} = \frac{V_{VT} \times S}{l_{VT} / b_{wing}} \cong 0.025 \text{ m}^2 \quad (2.8)$$

Lower aspect ratio wings have higher stall angle [75] thus, AR_{HT} is specified to be:

$$AR_{HT} = 4$$

Also, the vertical tail has no taper ratio like the main wing. The horizontal tail span is calculated as:

$$b_{HT} = \sqrt{AR_{HT} S_{HT}} = \sqrt{4 \times 0.089} = 0.6 \text{ m} . \quad (2.9)$$

Then, again for a rectangular horizontal stabilizer, the chord length is calculated as:

$$c_{HT} = \frac{S_{HT}}{b_{HT}} = 0.15 \text{ m} . \quad (2.10)$$

Similarly, for the vertical tail the height is calculated as:

$$h_{VT} = \sqrt{AR_{VT}S_{VT}} = \sqrt{1.6 \times 0.025} = 0.2 \text{ m}. \quad (2.11)$$

Unlike wing and horizontal tail, vertical tail taper ratio (λ) is specified [75,76] to be:

$$\lambda = 0.6$$

The root chord length (c_r) of the vertical tail, is kept same, as:

$$c_{r_{VT}} = 0.15 \text{ m}$$

$$c_{t_{VT}} = \lambda_{VT} c_{r_{VT}} = 0.6 \times 0.15 = 0.09 \text{ m} \quad (2.12)$$

After all these sizing calculations are done, the wing and tail geometries sizes remains as indicated in Figure 2.7.

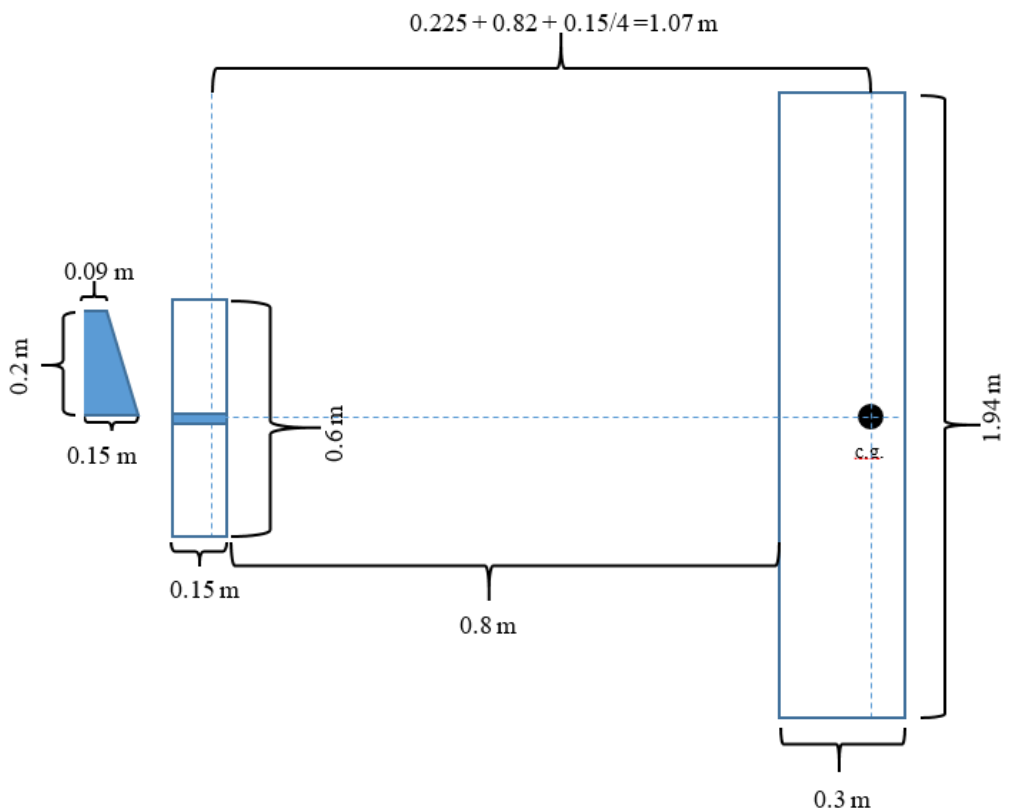


Figure 2.7. Wing-tail geometry and sizing

2.5 Fuselage Design

The sizing of the fuselage is determined by considering to contain flight controller, batteries, airspeed sensor, telemetry module and other avionic equipment. The fuselage is long enough and permits the adjustment of c.g. by moving the batteries. A rectangular – trapezoid prism shaped fuselage is designed. It is easy to construct the fuselage by combining plaques of materials such as foam. The wing will be placed on the carved places on sides of the fuselage. The design is shown in Figure 2.8 and 2.9.

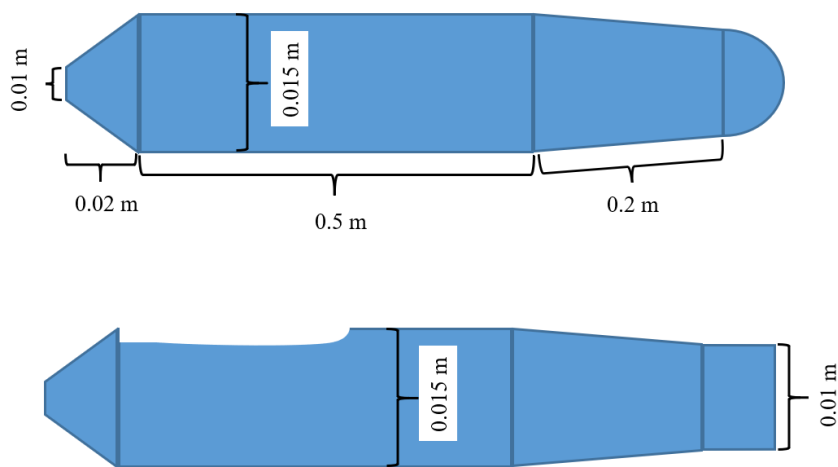


Figure 2.8. Bottom and side view of the fuselage

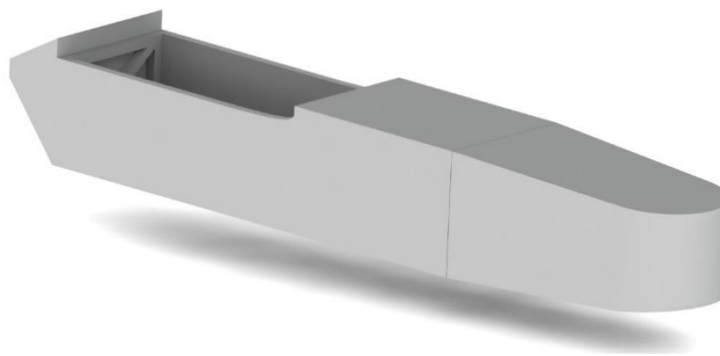


Figure 2.9. A 3D view of the fuselage

2.6 Propulsion Choice

Design optimization is out of the scope of the study. Motor-propeller combination and tilt-servos will be chosen to be relatively higher than necessary force and torque requirements, to prevent the vehicle from actuator saturation. In order of keeping the pitch angle at zero while tilting the rotors during the transition phase, more thrust is needed to stabilize the altitude. Therefore, the propellers are desired to supply more than twice of the estimated weight of the vehicle. 15-inch diameter with 5 pitch rate propellers (15x5) have been specified, such that a motor-propeller pair can supply up to 3 kg thrust while rotating at 8000 rpms.

2.7 Rotor Placement

The tilt-rotors will not be placed at the tip of the wings, otherwise, the moment arm for the rotors would be too high for 1.94 m span of wings, and a structural fortification would be needed that causing extra weight unfortunately. The tilt-rotors will be set on beams getting out the leading edge of the wing on both sides. After, determining wing-tail geometry, sizing, and the propeller diameter, the c.g. of the tricopter is overlapped with the c.g. of the fixed-wing module which was determined to be at the quarter chord of the wing. The layout with rotor settlement is shown in Figure 2.10.

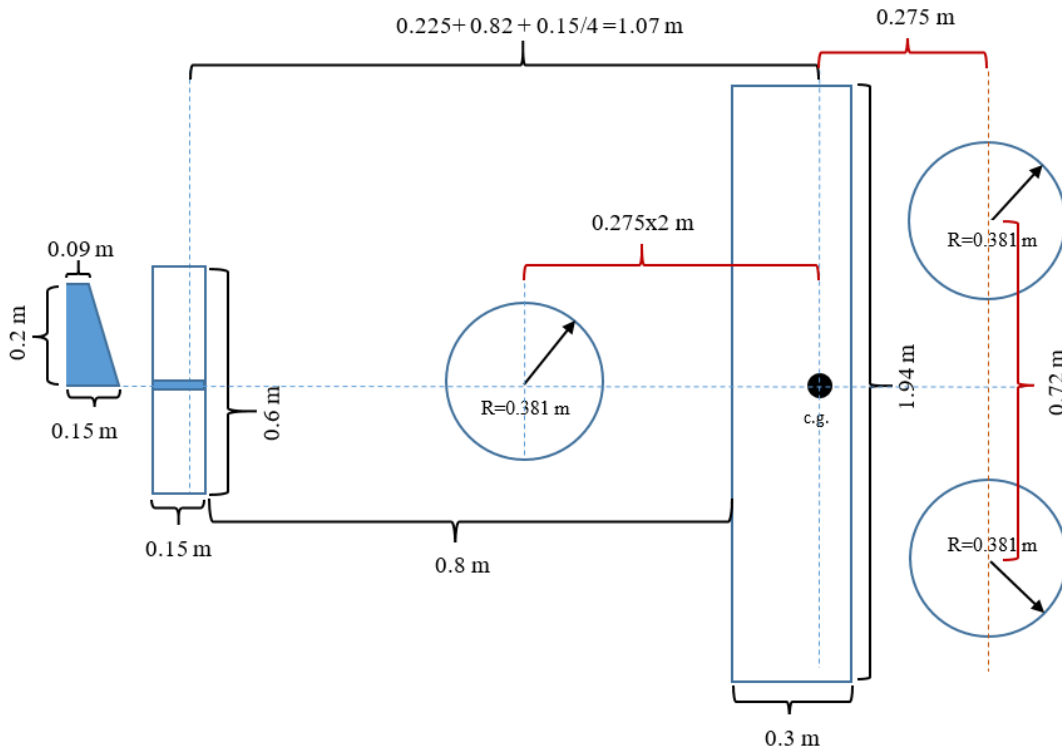


Figure 2.10. Configuration layout with rotor settlement

2.8 Control Surface Sizing

For a fixed-wing conventional aircraft, the primary control surfaces are ailerons, elevator and rudder which correspond to the control of roll, pitch and yaw motions, respectively. The longitudinal length (chord) for ailerons are typically about 15-25% of the wing chord. Also, for elevators and rudders, this ratio is about 25-50% of the tail chord [76]. Thus, aileron chord length is specified as quarter of the wing chord. Similarly, the elevator and rudder chord length are also specified as quarter of the tail chord.

Along the span, the ailerons typically extend approximately from half to the 90% of the wing span. Some aircrafts have ailerons that reach to wing tips which provides a control effectiveness due to the vortex flow at the tips [76]. For this design, the ailerons

are determined to have length of 55 cm in a rectangular shape, reaching to wing tips. The elevator is also specified rectangularly and it extends the entire span of the horizontal tail. Finally, the rudder is tapered with the same ratio of the vertical tail ($\lambda = 0.6$) and they are same in span size. They are illustrated in Figure 2.11.

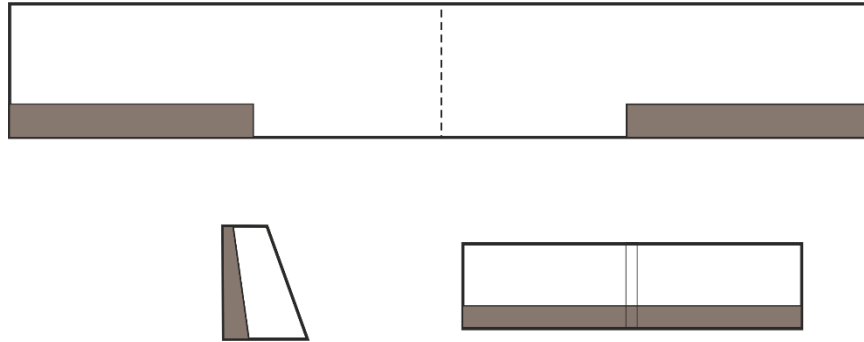


Figure 2.11. Illustration of control surfaces placed on wing and tail

2.9 Design Parameters

The sizing, geometry, mass and some other parameters obtained at the end of design process is provided. Geometric and sizing parameters of fixed-wing module is given in Table 2.2.

Table 2.2. Geometric and Sizing parameters

Parameters	Wing	Horizontal Tail	Vertical Tail
Airfoil	Clark-Y	NACA 0012	NACA 0012
Span (m)	1.94	0.6	0.2
Root Chord (m)	0.3	0.15	0.15
Tip Chord (m)	0.3	0.15	0.09
Area (m ²)	0.58	0.09	0.025
Aspect Ratio	6.45	4	1.6
Taper Ratio	1	1	0.6
Incidence Angle (deg)	2	0	0
Twist Angle (deg)	0	0	0
Sweep Angle (deg)	0	0	0

The mass is estimated to be approximately 4 kg including structural materials, actuators and avionics equipment. The mass budget is shown in Table 2.3 with the details.

Table 2.3. Mass budget of the aerial vehicle

Tricopter Module					Fixed-Wing Module				
Name	Nr	Weight	Subtotal	Unit	Name	Nr	Weight	Subtotal	Unit
Motor	3	250	750	g	Servo	4	30	120	g
ESC	3	50	150	g	Body	1	1000	1000	g
Servo	2	70	140	g	Electronics	1	200	200	g
Propeller	3	30	90	g				0	g
Pixhawk 2	1	40	40	g				0	g
Antenna	1	50	50	g				0	g
GPS	1	60	60	g				0	g
Battery	1	900	900	g				0	g
Cabling	1	500	500	g					
Total			2680	g	Total			1320	g
TOTAL					4000				
					g				

At the end of the design process, the vehicle is built in detail including the weights of the constructional operational materials, in a 3D CAD software. Moments of inertia and products of inertia in body-fixed reference frame was calculated by the software and reported.

$$I_B = \begin{bmatrix} I_{xx} & -I_{xy} & -I_{xz} \\ -I_{yx} & I_{yy} & -I_{yz} \\ -I_{zx} & -I_{yx} & I_{zz} \end{bmatrix} = \begin{bmatrix} 0.3632 & -0.0001 & -0.0048 \\ -0.0001 & 0.3022 & -0.0006 \\ -0.0048 & -0.0006 & 0.6358 \end{bmatrix} \text{ kg.m}^2 \quad (2.13)$$

Finally, the 3D CAD view of the designed hybrid UAV is illustrated in Figure 2.12. Also, a picture of the vehicle after the manufacturing is given in Figure 2.13. The stability characteristics of the designed vehicle will be investigated in Chapter 4.

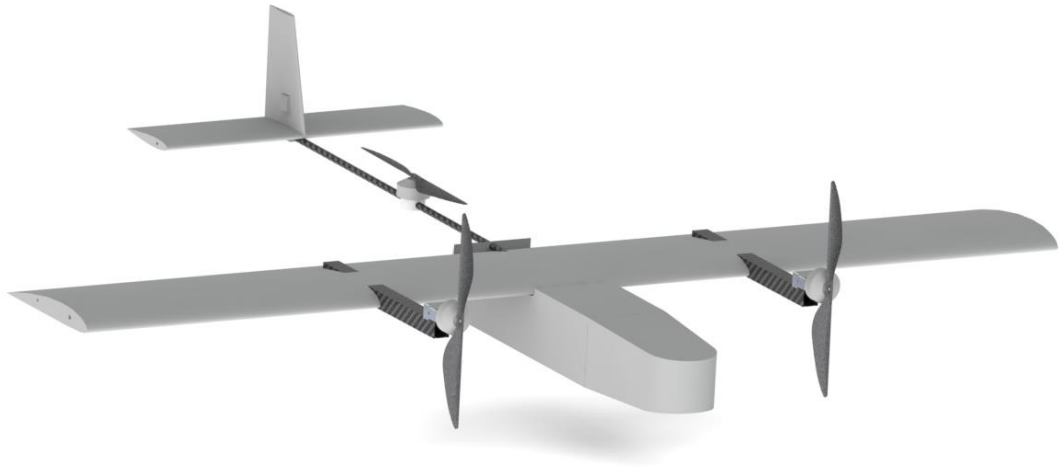


Figure 2.12. The final view of the designed vehicle in a CAD software



Figure 2.13. The view of the hybrid vehicle after the construction

CHAPTER 3

THEORY AND MODELING

In this chapter some basic concepts in Flight Dynamics such as, reference frames, attitude parametrization, 6 DoF equations of motion and notation convention are described. Nonlinear mathematical model of the hybrid aerial vehicle is derived in detail and presented including propulsive and aerodynamic characteristics of multirotor and fixed-wing modules.

3.1 Reference Frames and Coordinate Systems

Vectors are perceived differently from different observing points and thus they must be defined according to a reference (frame). A reference frame is a notion that vector quantities such as forces, velocities and accelerations are defined relative to it. A coordinate system is a tool that placed into a reference frame for measuring the quantities. Inertial, body-fixed, vehicle-carried and Earth-fixed frame of references and coordinate systems are very commonly employed concepts in Flight Dynamics [79]. All the defined reference frames are right-handed.

3.1.1 Inertial Reference Frame \mathbb{F}_I (Inertial Axes, $O_I X_I Y_I Z_I$)

It is the frame of reference that assumed to be fixed (or in relative motion) relative to distant stars and in inertial frame Newton's second equation $\mathbf{F} = m\mathbf{a}$ is valid. If \mathbf{a} was defined in a rotating reference frame it would not be true and there should have been terms that express the rotation of the reference frame relative to the inertial frame [79].

3.1.2 Earth-Fixed Reference Frame F_E (Earth Axes, $O_E X_E Y_E Z_E$)

This is generally used as inertial frame in low speed applications such as aircraft dynamics, since the rotation of the Earth relative to the inertial frame is insignificant. However, for high velocity applications such as spacecraft dynamics it becomes not negligible. O_E is attached on the surface of a perfect round Earth anywhere, X_E axis points towards the north, Y_E axis points towards the east and the Z_E axis points towards the center of the Earth.

When the rotation of the Earth is important, the Earth-centered reference frame F_{EC} is used. The origin O_{EC} is at the center of the Earth, X_{EC} - Y_{EC} constitutes the plane of equator and the Z_{EC} points toward the north pole. The frames of reference are illustrated in Figure 3.1.

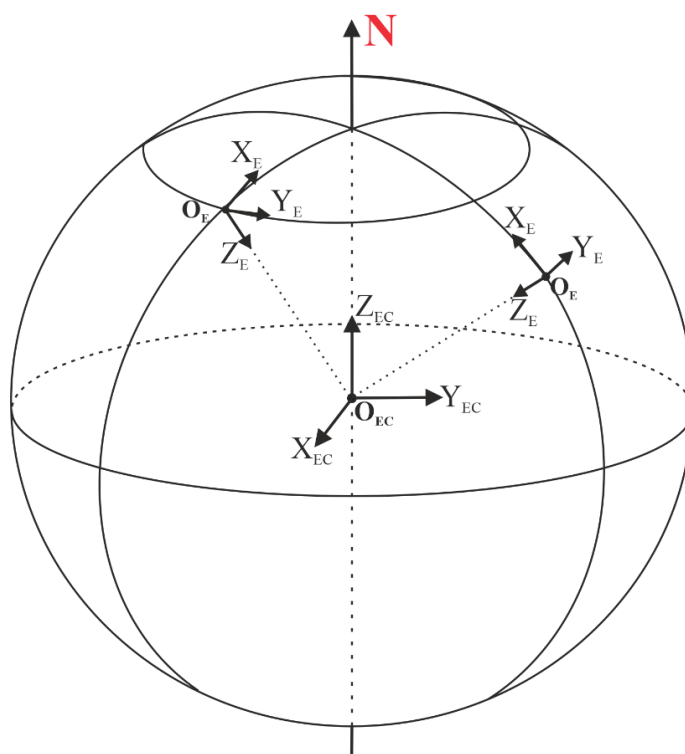


Figure 3.1. Earth-fixed and Earth-centered reference frame

3.1.3 Vehicle-Carried Reference Frame F_V (Axes, O_V, x_V, y_V, z_V)

It is also known as North-East-Down (NED) reference frame. The origin O_V is attached to the c.g. of a vehicle and moves with it. The axes x_V, y_V, z_V are directed towards the north, the east and the center of the Earth, respectively. The curvature of the Earth is negligible and is assumed as a flat Earth. The reference frame is illustrated in Figure 3.2.

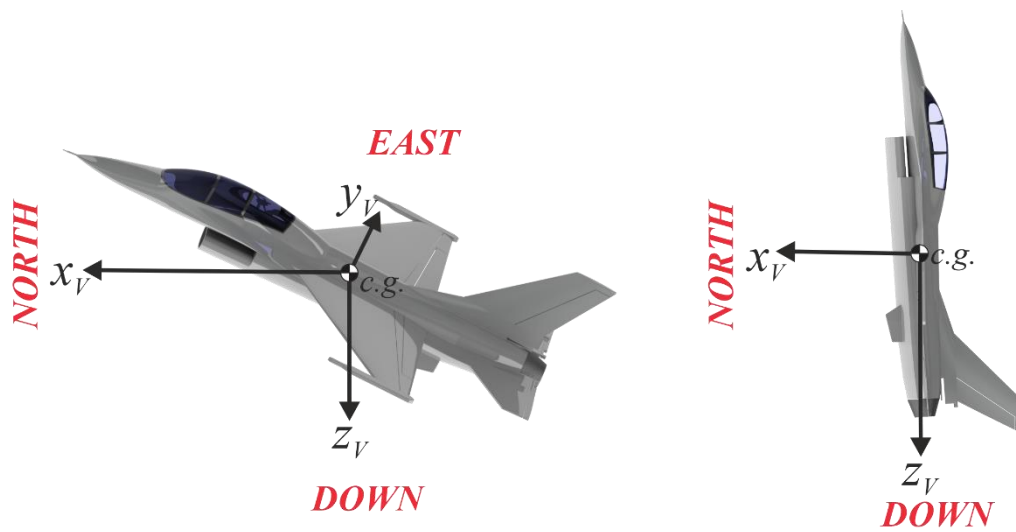


Figure 3.2. Illustration of vehicle-carried reference frame

3.1.4 Air-Trajectory Reference Frame F_W (Wind Axes, O_W, x_W, y_W, z_W)

The origin O_W is attached at the c.g. of a vehicle and x_W axis is aligned with the velocity vector \mathbf{V} relative to the air. The z_W axis is in the plane of symmetry of an aircraft and y_W axis takes its place so that to form a right-handed coordinate system. The wind-fixed reference frame is illustrated in Figure 3.3.

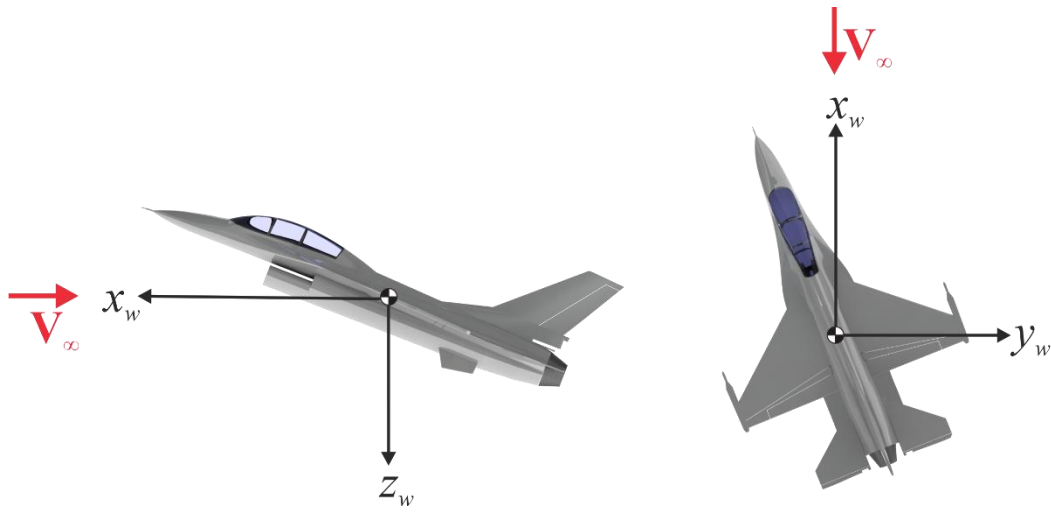


Figure 3.3. Illustration of air-trajectory reference frame

3.1.5 Body-Fixed Reference Frame F_B (Body Axes, $O_B x_B y_B z_B$)

The origin O_B is attached at the c.g. of a vehicle and x_B axis is directed towards the nose of the aircraft. The z_B axis lies in plane of symmetry of the aircraft and y_B axis takes its place so that to form a right-handed coordinate system. The body-fixed reference frame is illustrated in Figure 3.4.

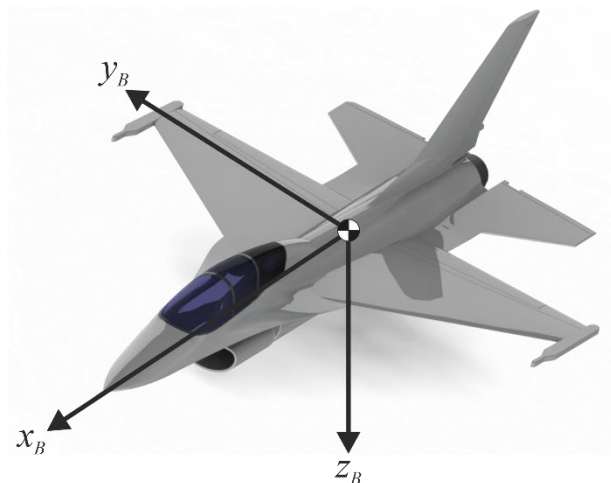


Figure 3.4. Illustration of body-fixed reference frame

3.1.6 Stability Axes $F_s (O_s x_s y_s z_s)$

Stability axes are a form of body axes generally used in small disturbance analyzes. If body x_B axis is aligned with the projection of airspeed vector \mathbf{V} on symmetry plane of a vehicle via rotating it around y_B axis, then it turns into stability axes. It is illustrated in Figure 3.5.

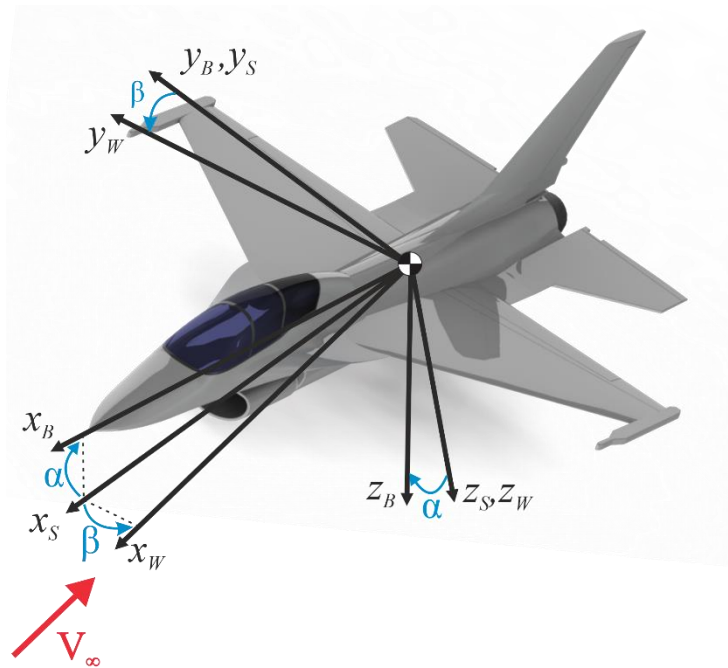


Figure 3.5. Illustration of stability axes

3.2 Attitude Parametrization

3.2.1 Euler Angles (ϕ, θ, ψ)

In three-dimensional Euclidean space, the orientation of any object or reference frame can be expressed relative to another by defining three angles that are called Euler angles (ϕ, θ, ψ) , roll, pitch and yaw, respectively. To avoid ambiguities, interval for the Euler angles are determined as follows:

$$\begin{aligned}
-\pi &\leq \phi < \pi \\
-\frac{\pi}{2} &\leq \theta \leq \frac{\pi}{2} \\
-\pi &\leq \psi < \pi
\end{aligned}$$

Using Euler angles most of the orientations can be represented uniquely. But there are some cases where the Euler angles becomes non-unique. To overcome this issue, quaternions may be used.

In flight dynamics, the vehicle Euler angles which are a special case of Euler angles that are used to rotate or transform the vehicle-carried reference frame \mathbf{F}_V to the body-fixed reference frame. The rotations should be performed in a sequence such that:

1st rotation is around z_V axis of vehicle-carried frame \mathbf{F}_V , by angle $\psi : \mathbf{F}_V \rightarrow \mathbf{F}_1$

2nd rotation is around y_1 axis of first intermediate frame \mathbf{F}_1 , by angle $\theta : \mathbf{F}_1 \rightarrow \mathbf{F}_2$

3rd rotation is around x_2 axis of second intermediate frame \mathbf{F}_2 , by angle $\phi : \mathbf{F}_2 \rightarrow \mathbf{F}_B$

3.2.2 Transformation via Euler Angles

A vector specified in a reference frame could be expressed in another by transforming it using Euler angles based transformation matrices. It should be noted that; always transformation and rotation is not the same thing. The same vector is represented in another frame by transforming it, however if it is rotated the vector becomes modified. Transforming a vector into another reference frame is equivalent to rotating the frame of reference. [80]

Let $\mathbf{V} = [V_x \ V_y \ V_z]^T$ be a vector in vehicle-carried reference frame and let's transform it into body-fixed coordinate system.

$$\begin{bmatrix} Vx_v \\ Vy_v \\ Vz_v \end{bmatrix} \begin{array}{l} \text{rotate c.s. around } Z_v \text{ of } \mathbf{F}_v \\ \text{using } \mathbf{L}_3 \rightarrow \\ \text{by angle } \psi \end{array} \begin{bmatrix} Vx_1 \\ Vy_1 \\ Vz_1 \end{bmatrix} \begin{array}{l} \text{rotate c.s. around } Y_1 \text{ of } \mathbf{F}_1 \\ \text{using } \mathbf{L}_2 \rightarrow \\ \text{by angle } \theta \end{array} \begin{bmatrix} Vx_2 \\ Vy_2 \\ Vz_2 \end{bmatrix}$$

$$\begin{bmatrix} Vx_2 \\ Vy_2 \\ Vz_2 \end{bmatrix} \begin{array}{l} \text{rotate the around } X_v \text{ of } \mathbf{F}_2 \\ \text{using } \mathbf{L}_1 \rightarrow \\ \text{by angle } \phi \end{array} \begin{bmatrix} Vx_B \\ Vy_B \\ Vz_B \end{bmatrix}$$

$$\mathbf{L}_1 = \begin{bmatrix} 1 & 0 & 0 \\ 0 & \cos \phi & \sin \phi \\ 0 & -\sin \phi & \cos \phi \end{bmatrix} \quad (3.1)$$

$$\mathbf{L}_2 = \begin{bmatrix} \cos \theta & 0 & -\sin \theta \\ 0 & 1 & 0 \\ \sin \theta & 0 & \cos \theta \end{bmatrix} \quad (3.2)$$

$$\mathbf{L}_3 = \begin{bmatrix} \cos \psi & \sin \psi & 0 \\ -\sin \psi & \cos \psi & 0 \\ 0 & 0 & 1 \end{bmatrix} \quad (3.3)$$

The overall transformation matrix for transforming a vector from the vehicle-carried coordinate system to the body-fixed coordinate system is obtained by multiplying in order.

$$\mathbf{V}_B = \mathbf{L}_{BV} \mathbf{V}_V \quad (3.4)$$

where \mathbf{L}_{BV} is given by,

$$\mathbf{L}_{BV} = \mathbf{L}_1(\phi) \mathbf{L}_2(\theta) \mathbf{L}_3(\psi) \quad (3.5)$$

or it can be given explicitly as in Equation (3.6).

$$\mathbf{L}_{BV} = \begin{bmatrix} \cos \theta \cos \psi & \cos \theta \sin \psi & -\sin \theta \\ \sin \phi \sin \theta \cos \psi - \cos \phi \sin \psi & \sin \phi \sin \theta \sin \psi + \cos \phi \cos \psi & \sin \phi \cos \theta \\ \cos \phi \sin \theta \cos \psi + \sin \phi \sin \psi & \cos \phi \sin \theta \sin \psi - \sin \phi \cos \psi & \cos \phi \cos \theta \end{bmatrix} \quad (3.6)$$

The overall transformation matrix is shown in Equation (3.6). This transformation can be generalized to any rotation between reference frames. The rotation between wind and body axes is shown as given below.

$$\mathbf{V}_B = \mathbf{L}_{BW} \mathbf{V}_W \quad (3.7)$$

where \mathbf{L}_{BW} is given by,

$$\mathbf{L}_{BW} = \mathbf{L}_2(\alpha)\mathbf{L}_3(-\beta) = \begin{bmatrix} \cos \alpha \cos \beta & -\cos \alpha \sin \beta & -\sin \alpha \\ \sin \beta & \cos \beta & 0 \\ \sin \alpha \cos \beta & -\sin \alpha \sin \beta & \cos \alpha \end{bmatrix} \quad (3.8)$$

where α and β are aerodynamic angles, which are called as angle of attack and side slip angle, can be calculated as given in Equations (3.9) and (3.10).

$$\alpha = \tan^{-1} \frac{w}{u}, \quad -\pi \leq \alpha \leq \pi \quad (3.9)$$

$$\beta = \sin^{-1} \frac{v}{|\mathbf{V}|}, \quad -\pi \leq \beta \leq \pi \quad (3.10)$$

There are some properties of transformation matrices. The inverse of a transformation matrix inverts the direction of transformation.

$$\mathbf{L}_{BV} = \mathbf{L}_{VB}^{-1} \quad \text{and} \quad \mathbf{L}_{VB} = \mathbf{L}_{BV}^{-1} \quad (3.11)$$

Transpose of a transformation matrix is equal to its inverse as follows:

$$\mathbf{L}_{BV}^{-1} = \mathbf{L}_{BV}^T \quad (3.12)$$

Multiplication of it and its inverse gives identity matrix.

$$\mathbf{L}_{BV} \mathbf{L}_{BV}^{-1} = \mathbf{I} \quad (3.13)$$

3.3 Equations of Motion

To study and analyze dynamics of a physical system, its mathematical model must be extracted. Owing to the mathematical models, 6 DoF equations of motion, dynamical systems can be simulated and examined prior to the construction of the system and thus, enabling modification and optimization. To obtain mathematical model of a hybrid UAV, Newton-Euler equations are employed. The UAV is accepted to be a rigid body. As mentioned previously, to conform the second law of Newton, the velocities and accelerations must be relative to inertial frame. Mathematical model of nonlinear dynamical systems especially a flying aircraft is very complex and coupled. In order to reduce the complexity and calculation costs, reasonable simplifications are performed. For this reason, Earth-fixed reference frame is utilized instead of inertial frame and the Earth is assumed to be flat.

The sign convention of angular velocities and resultant moments are right-handed. While thumb of right hand is directed towards a positive body axis, then fingers show the direction of positive rotation. Some variables which are used in equations of motion are given as follows as shown Figure 3.6.

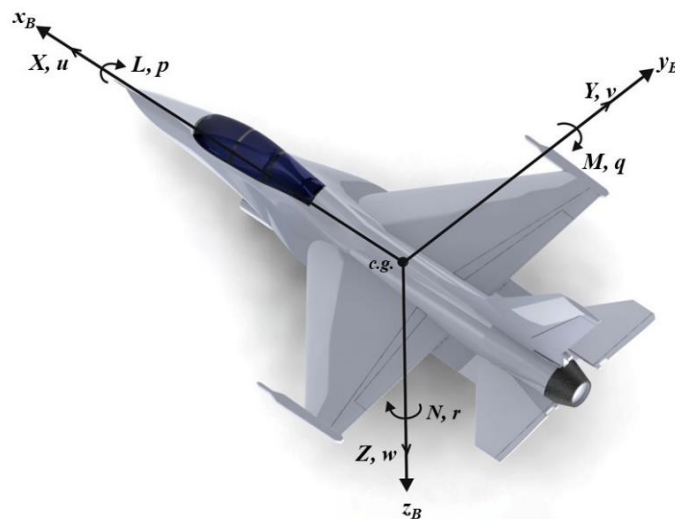


Figure 3.6. Force and moment vectors given in body-fixed reference frame

$$\mathbf{F}_B^* = \begin{bmatrix} X \\ Y \\ Z \end{bmatrix} \Rightarrow \left. \begin{array}{l} X: x_B \text{ component of} \\ Y: y_B \text{ component of} \\ Z: z_B \text{ component of} \end{array} \right\} \begin{array}{l} \text{resultant} \\ \text{*aeropropulsive} \\ \text{force} \end{array} \quad \mathbf{G}_B = \begin{bmatrix} L \\ M \\ N \end{bmatrix} \Rightarrow \begin{array}{l} L: \text{rolling moment} \\ M: \text{pitching moment} \\ N: \text{yawing moment} \end{array}$$

$$\mathbf{V}_B = \begin{bmatrix} u \\ v \\ w \end{bmatrix} \Rightarrow \left. \begin{array}{l} u: x_B \text{ component of} \\ v: y_B \text{ component of} \\ w: z_B \text{ component of} \end{array} \right\} \begin{array}{l} \text{speed} \\ \text{relative} \\ \text{to air} \end{array} \quad \boldsymbol{\omega}_B = \begin{bmatrix} p \\ q \\ r \end{bmatrix} \Rightarrow \begin{array}{l} p: \text{roll rate} \\ q: \text{pitch rate} \\ r: \text{yaw rate} \end{array}$$

$$\mathbf{r}_B = \begin{bmatrix} x \\ y \\ z \end{bmatrix} \Rightarrow \begin{array}{l} \text{position} \\ \text{vector in} \\ F_B \text{ frame} \end{array} \quad \mathbf{r}_E = \begin{bmatrix} x_E \\ y_E \\ z_E \end{bmatrix} \Rightarrow \begin{array}{l} \text{position} \\ \text{vector in} \\ F_E \text{ frame} \end{array}$$

Beginning from Newton's second law to obtain translational equations of motion, also noting that the vectors are relative to F_E frame:

$$\mathbf{F}_E = m \frac{d}{dt} \dot{\mathbf{V}}_E \Rightarrow \mathbf{F}_B = m \frac{d}{dt} (\dot{\mathbf{V}}_B + \boldsymbol{\omega}_B \times \mathbf{V}_B) \quad (3.14)$$

Here, \mathbf{F}_B is total force acting on c.g. of the vehicle, including aerodynamic \mathbf{F}_A , propulsive \mathbf{F}_P and gravitational \mathbf{F}_G forces.

$$\mathbf{F}_B = \mathbf{F}_A + \mathbf{F}_P + \mathbf{F}_G = \mathbf{F}_A + \mathbf{F}_P + m\mathbf{g} \quad (3.15)$$

Expanding Equation (3.14), we get,

$$\begin{bmatrix} X \\ Y \\ Z \end{bmatrix} + \mathbf{L}_{BV} \begin{bmatrix} 0 \\ 0 \\ m\mathbf{g} \end{bmatrix} = m \left[\begin{bmatrix} \dot{u} \\ \dot{v} \\ \dot{w} \end{bmatrix} + \begin{bmatrix} p \\ q \\ r \end{bmatrix} \times \begin{bmatrix} u \\ v \\ w \end{bmatrix} \right] \quad (3.16)$$

Similarly, for rotational equations of motion,

$$\mathbf{G}_E = m \frac{d}{dt} \dot{\mathbf{H}}_E \Rightarrow \mathbf{G}_B = m \frac{d}{dt} (\dot{\mathbf{H}}_B + \boldsymbol{\omega}_B \times \mathbf{H}_B) \quad (3.17)$$

where \mathbf{G} is resultant moment about c.g. of the vehicle, and \mathbf{H} is moment of momentum or angular momentum. Again, the moments acting on center of mass may be given as,

$$\mathbf{G}_B = \mathbf{G}_A + \mathbf{G}_P \quad (3.18)$$

Angular momentum and its derivative may be written as,

$$\mathbf{H}_B = \mathbf{I}_B \boldsymbol{\omega}_B \quad (3.19)$$

$$\dot{\mathbf{H}}_B = \dot{\mathbf{I}}_B \boldsymbol{\omega}_B + \mathbf{I}_B \dot{\boldsymbol{\omega}}_B \cong \mathbf{I}_B \dot{\boldsymbol{\omega}}_B \quad (3.20)$$

where

$$\mathbf{I}_B = \begin{bmatrix} I_{xx} & -I_{xy} & -I_{xz} \\ -I_{yx} & I_{yy} & -I_{yz} \\ -I_{zx} & -I_{zy} & I_{zz} \end{bmatrix}. \quad (3.21)$$

\mathbf{I}_B is the matrix of inertia and its elements are moment and product of inertia of the vehicle and are shown in equations (3.22-3.23). Given dm is infinitesimal (differential) mass that integrated throughout the vehicle. Since the airplanes are almost symmetrical with respect to the symmetry plane- xz , then I_{xy} and I_{yz} becomes zero.

$$I_{xx} = \int (y^2 + z^2) dm; \quad I_{yy} = \int (x^2 + z^2) dm; \quad I_{zz} = \int (x^2 + y^2) dm \quad (3.22)$$

$$I_{xy} = I_{yx} = \int xy dm; \quad I_{xz} = I_{zx} = \int xz dm; \quad I_{yz} = I_{zy} = \int yz dm \quad (3.23)$$

Expanding Equation (3.17),

$$\begin{bmatrix} L \\ M \\ N \end{bmatrix} = \mathbf{I}_B \begin{bmatrix} \dot{p} \\ \dot{q} \\ \dot{r} \end{bmatrix} + \begin{bmatrix} p \\ q \\ r \end{bmatrix} \times \mathbf{I}_B \begin{bmatrix} p \\ q \\ r \end{bmatrix} \quad (3.24)$$

The relation between angular rates and Euler angle rates may be written as,

$$\begin{bmatrix} p \\ q \\ r \end{bmatrix} = \begin{bmatrix} 1 & 0 & -\sin \theta \\ 0 & \cos \phi & \sin \phi \cos \theta \\ 0 & -\sin \phi & \cos \phi \cos \theta \end{bmatrix} \begin{bmatrix} \dot{\phi} \\ \dot{\theta} \\ \dot{\psi} \end{bmatrix} \quad (3.25)$$

and

$$\begin{bmatrix} \dot{\phi} \\ \dot{\theta} \\ \dot{\psi} \end{bmatrix} = \begin{bmatrix} 1 & \sin \phi \tan \theta & \cos \phi \tan \theta \\ 0 & \cos \phi & -\sin \phi \\ 0 & \sin \phi \sec \theta & \cos \phi \sec \theta \end{bmatrix} \begin{bmatrix} p \\ q \\ r \end{bmatrix} \quad (3.26)$$

In addition, for flight path tracking, velocity vector relative to F_E frame is needed and it can be easily obtained by transforming body-axis velocity vector from F_B frame.

$$\mathbf{V}_E = \begin{bmatrix} \dot{x}_E \\ \dot{y}_E \\ \dot{z}_E \end{bmatrix} = \mathbf{L}_{EB} \mathbf{V}_B \quad (3.27)$$

Finally, the equations given above can be combined after assuming the vehicle as a rigid body, the atmosphere as still, x - z plane as symmetry plane and neglecting gyroscopic terms of rotors, and then the general equations of motion can be written as follows.

$$\dot{u} = rv - qw - g \sin \theta + \frac{X}{m} \quad (a)$$

$$\dot{v} = pw - ru + g \sin \phi \cos \theta + \frac{Y}{m} \quad (b) \quad (3.28)$$

$$\dot{w} = qu - pv + g \cos \phi \cos \theta + \frac{Z}{m} \quad (c)$$

$$\dot{p} = \frac{I_{xz}}{I_{xx}} (\dot{r} + pq) + \frac{I_y - I_z}{I_{xx}} qr + \frac{L}{I_{xx}} \quad (a)$$

$$\dot{q} = \frac{I_{xz}}{I_{yy}} (r^2 - p^2) + \frac{I_z - I_x}{I_{yy}} pr + \frac{M}{I_{yy}} \quad (b) \quad (3.29)$$

$$\dot{r} = \frac{I_{xz}}{I_{zz}} (\dot{p} - qr) + \frac{I_x - I_y}{I_{zz}} pq + \frac{N}{I_{zz}} \quad (c)$$

$$\dot{\phi} = p + (q \sin \phi + r \cos \phi) \tan \theta \quad (a)$$

$$\dot{\theta} = q \cos \phi - r \sin \phi \quad (b) \quad (3.30)$$

$$\dot{\psi} = (q \sin \phi + r \cos \phi) \sec \theta \quad (c)$$

$$\dot{x}_E = u(c\theta c\psi) + v(s\phi s\theta c\psi - c\phi s\psi) + w(c\phi s\theta c\psi + s\phi s\psi) \quad (a)$$

$$\dot{y}_E = u(c\theta s\psi) + v(s\phi s\theta s\psi + c\phi c\psi) + w(c\phi s\theta s\psi - s\phi c\psi) \quad (b) \quad (3.31)$$

$$\dot{z}_E = u(-s\theta) + v(s\phi c\theta) + w(c\phi c\theta) \quad (c)$$

3.4 Mathematical Model of Multirotor Module

3.4.1 Propulsion Model

Force and torque generated by a propeller is proportional to its angular speed. There are some coefficient values for thrust and torque calculations which are specific for propulsion systems. Simply, the thrust and torque produced by a propulsion system can be modeled as given in the following equations.

$$T = k_f \Omega^2 \quad (3.32)$$

$$Q = k_t \Omega^2 \quad (3.33)$$

Ω , k_f and k_t indicates rpm value, thrust and torque coefficients of a motor-propeller pair, respectively. These coefficients can be calculated for known thrust/torque and rpm vectors. Least-Squares solution method is used to retrieve the rotor coefficients, and it is given in Equations (3.34) and (3.35).

$$k_f = \left(\Omega^{2T} \Omega^2 \right)^{-1} \Omega^{2T} T \quad (3.34)$$

$$k_t = \left(\Omega^{2T} \Omega^2 \right)^{-1} \Omega^{2T} Q \quad (3.35)$$

In the design phase of the project, the motor – propeller pair is selected to be T-Motor MN5212 KV420 electric motor and T-Motor 15x5 carbon fiber propeller. To retrieve mathematical model of the propulsion system, thrust and torque coefficients must be obtained. Experimental data obtained by load cell measurements are used (Table 3.1).

As specified, the rotor coefficients are calculated to be as follows.

$$k_f = 4.6914 \times 10^{-7} \quad (3.36)$$

$$k_t = 8.9048 \times 10^{-9} \quad (3.37)$$

Table 3.1. Experimental data of a propulsion system (a motor and a propeller pair)

RPM	Current (A)	Thrust (N)	Torque (N.m)
1000	0.28	0.32	0.008
2000	0.79	1.58	0.032
3000	1.88	3.81	0.076
4000	3.83	7.15	0.139
5000	6.80	11.45	0.219
6000	10.97	16.66	0.316
7000	16.9	23.05	0.435
8000	24.8	30.27	0.573

Subsequently, thrust and torque supplied by the propulsion system (motor-propeller) are calculated using the retrieved rotor coefficients. The calculated thrust and torque curves are proportional to the square of the angular speed of the rotor and they are plotted as given in Figures 3.7 and 3.8.

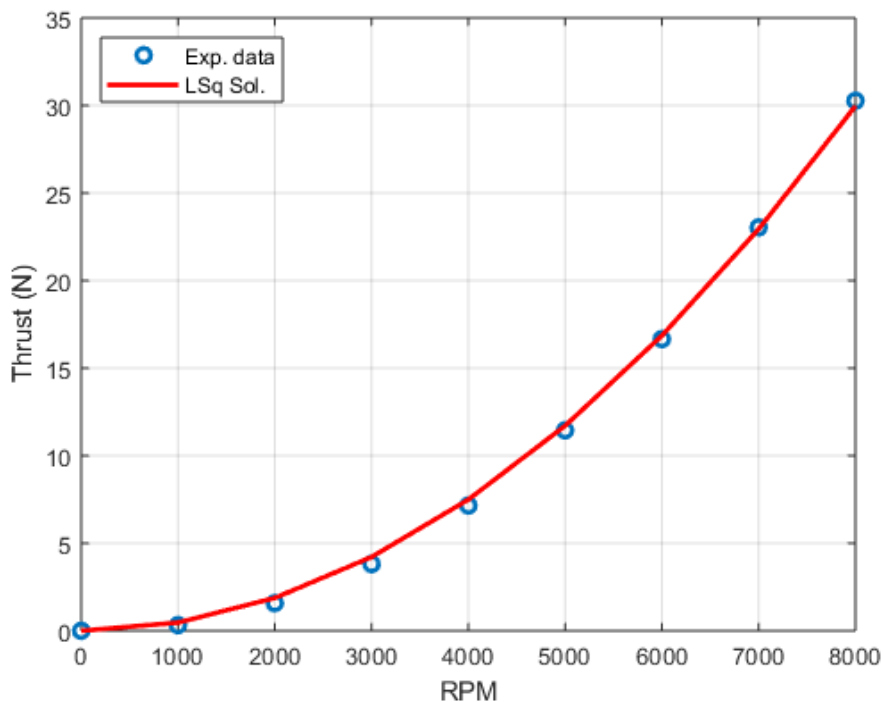


Figure 3.7. Thrust value generated by the propulsion system

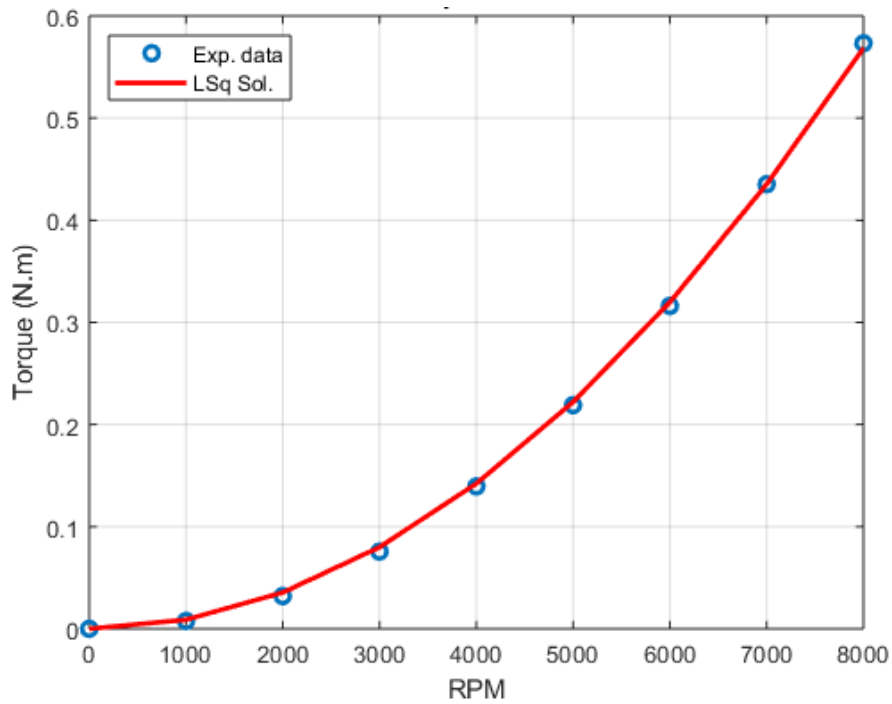


Figure 3.8. Torque value generated by the propulsion system

In order to observe and evaluate the accuracy of the thrust and torque measurements, the results are compared with the those supplied by the manufacturer. The manufacturer results are given in Table 3.2. Thrust and torque values obtained by relevant calculated coefficients at specific rpm values are compared and shown in Figure 3.9 and 3.10.

Table 3.2. Measurement data of motor-propeller supplied by the manufacturer [81]

RPM	Current (A)	Thrust (N)	Torque (N.m)
4976	0.68	11.81	0.321
5487	8.7	14.49	0.278
5947	10.5	17.12	0.330
6376	12.6	19.45	0.374
7287	18.8	25.39	0.493
8042	25.0	31.68	0.607
9091	36.7	40.94	0.784

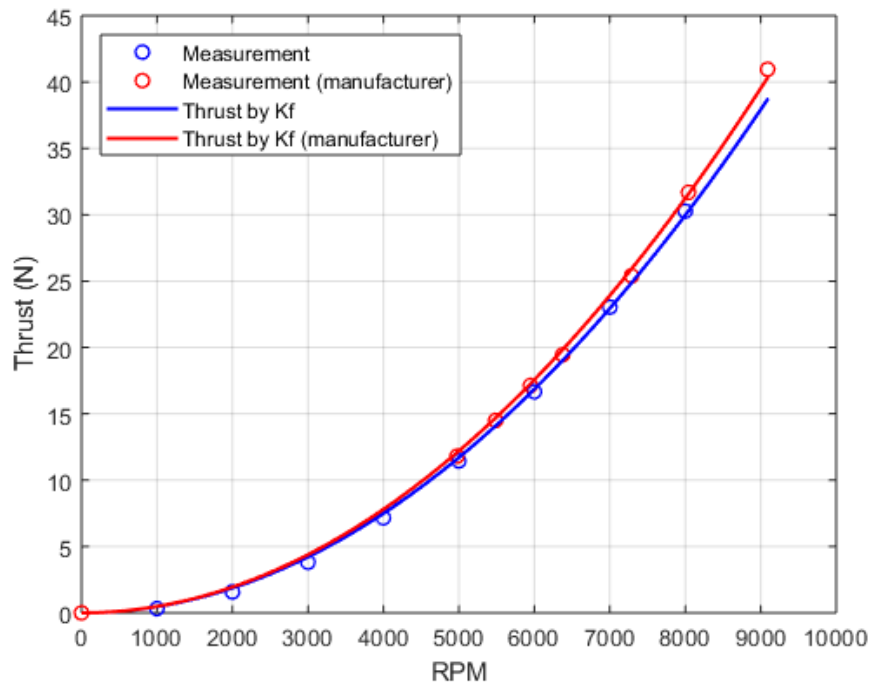


Figure 3.9. Produced thrust data by manufacturer and load cell measurement

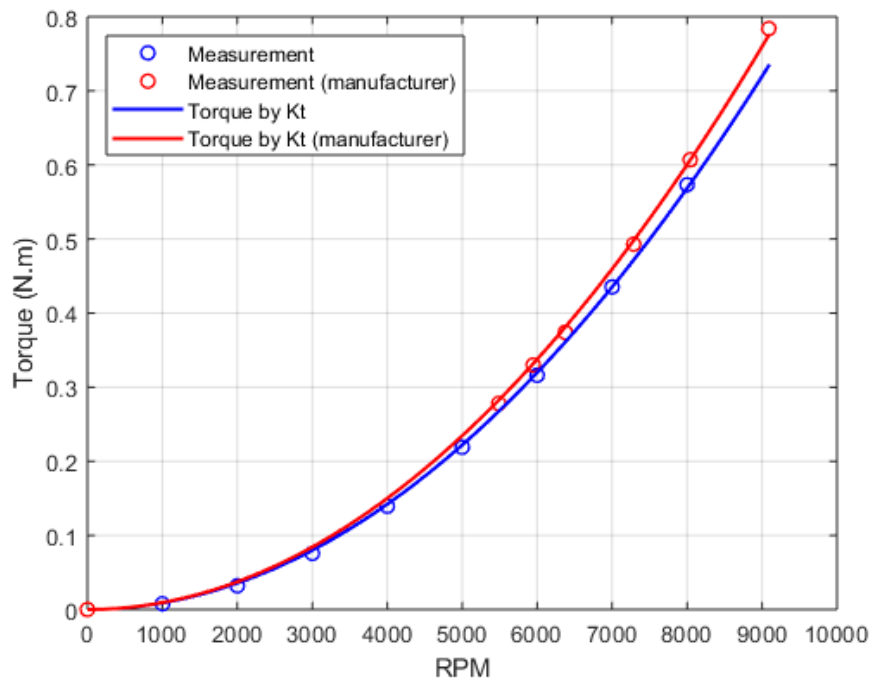


Figure 3.10. Produced torque data by manufacturer and load cell measurement

As seen in the figures given above, the measurement results obtained and supplied by the manufacturer are sufficiently similar. The difference in values between the two experimental outputs are less than 1.21 N for thrust and 0.031 N.m for torque at 8000 rpm. This small difference in results may be originated from the sensitivities of experimental setups and the environmental conditions such as temperature, altitude, moisture and etc. After validating the accuracy of the experimental setup, further measurements could be performed.

The results reported above were static thrust and torque values. The static model is valid for fixed pairs of propulsion systems relative to air and may be a valid/sufficient option for rotary wing aircrafts for hover flight conditions. However, in cruising applications especially for airplanes, the dynamic thrust and torque models must be revealed. Because these vehicles can fly with high speeds in the direction of the produced thrust/torque by the propulsion systems and generated values are significantly affected by the cruising speed.

In order to disclose the dynamic model of the propulsion system specified above, wind tunnel experiments were performed with several wind speeds that the wind tunnel is capable of. The experiments were conducted in an axial fan driven wind tunnel of Aerospace Engineering department at METU which has a 1 m x 1 m square cross-sectional dimension. The tunnel has 25 m/s operational velocity and less than 1% turbulence intensity. The motor-propeller pair was mounted to a load cell capable of measuring forces and moments in 3 axes. Also, the load cell was attached on a tilting joint with an angle indicator which was located at the center of the tunnel cross-section. The measurement setup and wind tunnel are illustrated in Figure 3.11 and 3.12. The measurements were performed for different tilt angles between 0 and 90 degrees (the wind flows towards the propeller perpendicular to the axis of rotation for 0° tilt case and it flows towards the propeller along the axis of rotation, for 90° tilt case) in order to obtain the dynamic propulsion model for all the possible flight conditions including hover, transition and forward flight. Experimental data were

collected for five different wind speeds. The measurements were performed for the parameters that given in Table 3.3. The data for the rotational speed of the rotor and the wind speed were collected by an rpm sensor and a velocity sensor.

Table 3.3. Measurement parameters of wind tunnel experiment

Tilt angle (deg)	0, 30, 60, 90
Incoming wind speed (m/s)	0, 5.2, 8.0, 10.75, 13.77
Rotational speed of the rotor (rpm)	$\Omega_1=1000$, $\Omega_8=8000$, $\Delta\Omega=1000$

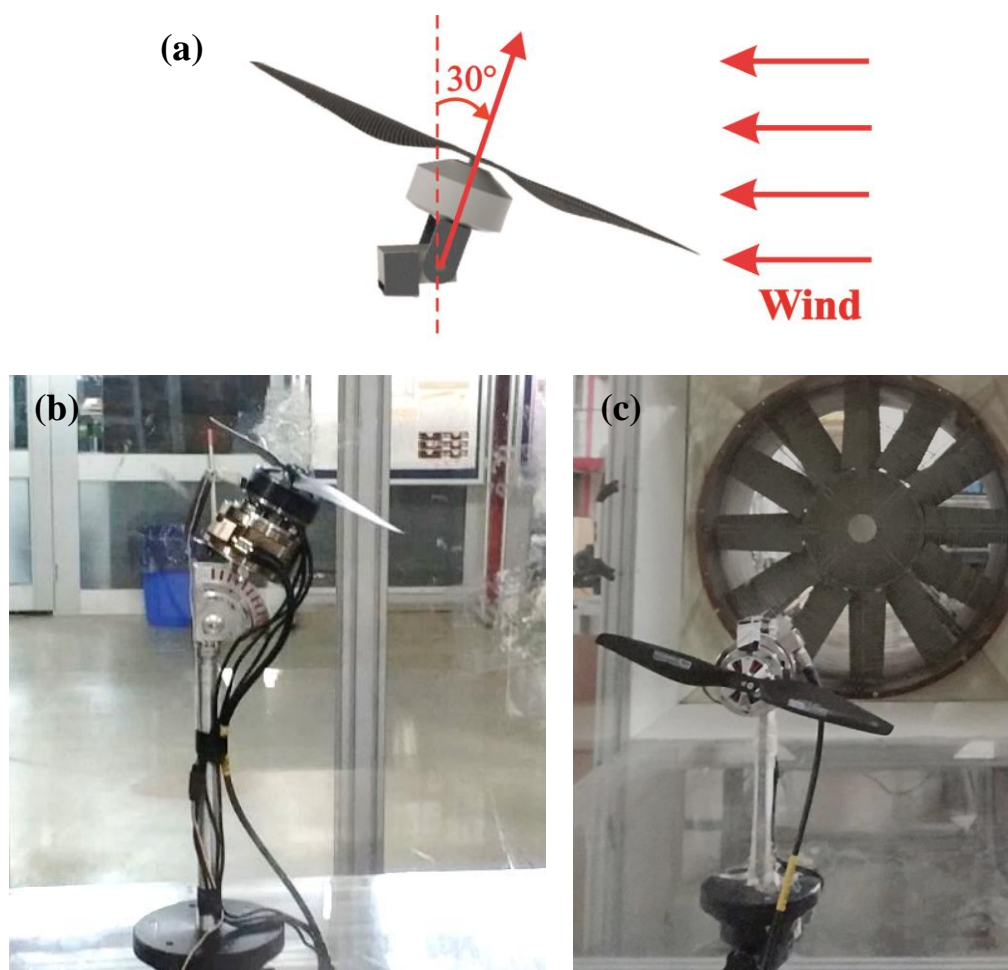


Figure 3.11. Experimental setup and its orientation in the wind tunnel with 30° tilt angle (case a and b) and 90° (case c) tilt angle



Figure 3.12. The wind tunnel used for the measurements [82]

The measurement results for the produced net thrust values (along the axis of rotation of the rotor) of a single motor-propeller pair are plotted versus wind speed for different rotational speeds of the rotor in the following figures. To prevent any ambiguity, net thrust should be defined as the produced thrust force by a single propeller minus drag force that was created by the flow of the wind which is normal to the plane of rotation of the rotor. Because, the load cell measures the produced net force along the axis of rotation. Interestingly, for the zero degree (corresponds to a side wind case) of tilt case, produced net thrust values increase with the increasing wind speed at all rotational speeds of the rotor. However, for the 90 degrees of tilt case (headwind towards the propeller), the produced net thrust values decrease with the increasing wind speed, as expected. Even, at high wind speeds, the propeller gained rotational speed due to the wind without applying any energy to the motor (windmill effect). Thus, the data at high speed winds (headwind) are not collected for low rpm values due to being unable to control rotational speed of the rotor. The rate of decrease in produced net thrust values increase as tilting the motor-propeller pair tilt angle from 0 to 90 degrees.

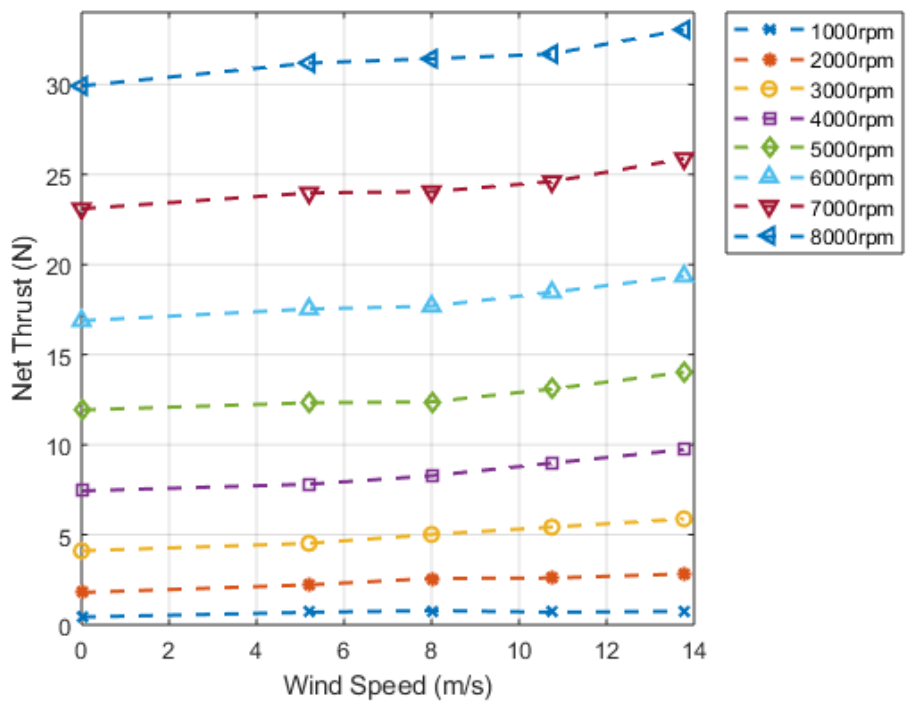


Figure 3.13. Produced net thrust vs wind speed for different rpm values at 0° tilt

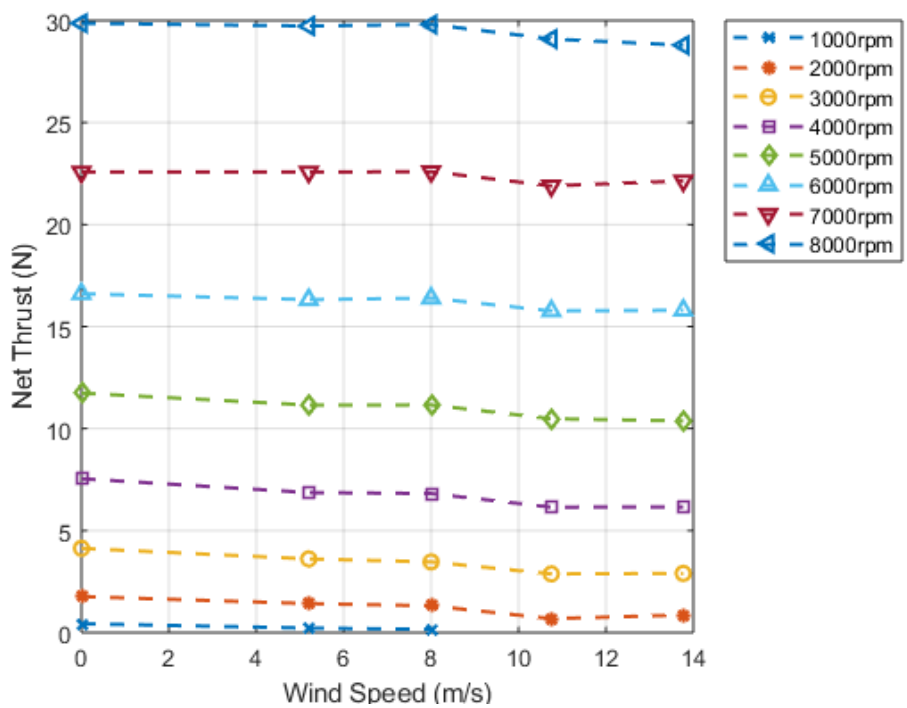


Figure 3.14. Produced net thrust vs wind speed for different rpm values at 30° tilt

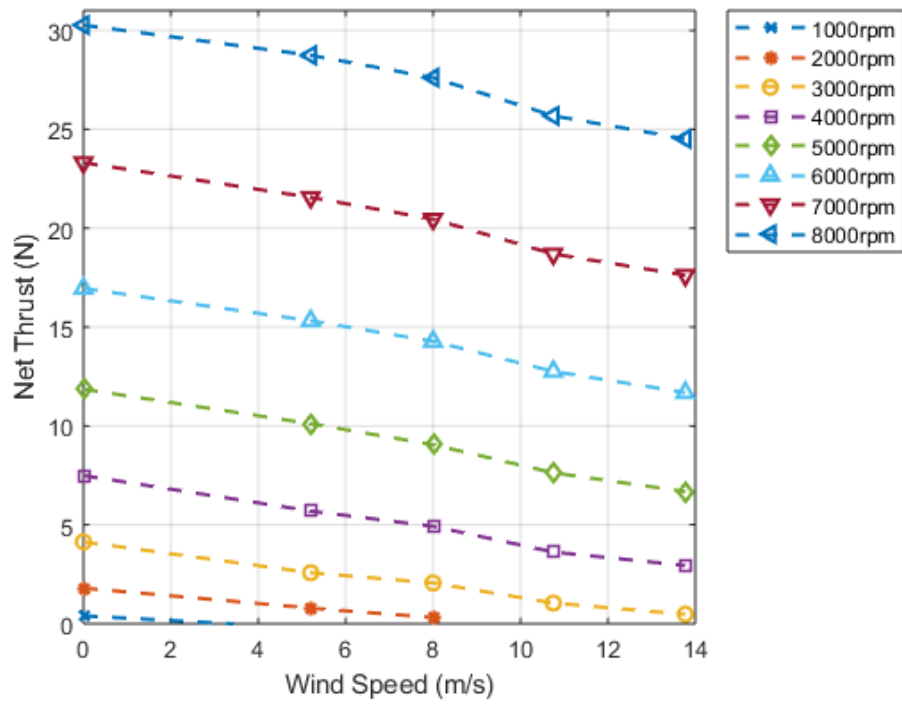


Figure 3.15. Produced net thrust vs wind speed for different rpm values at 60° tilt

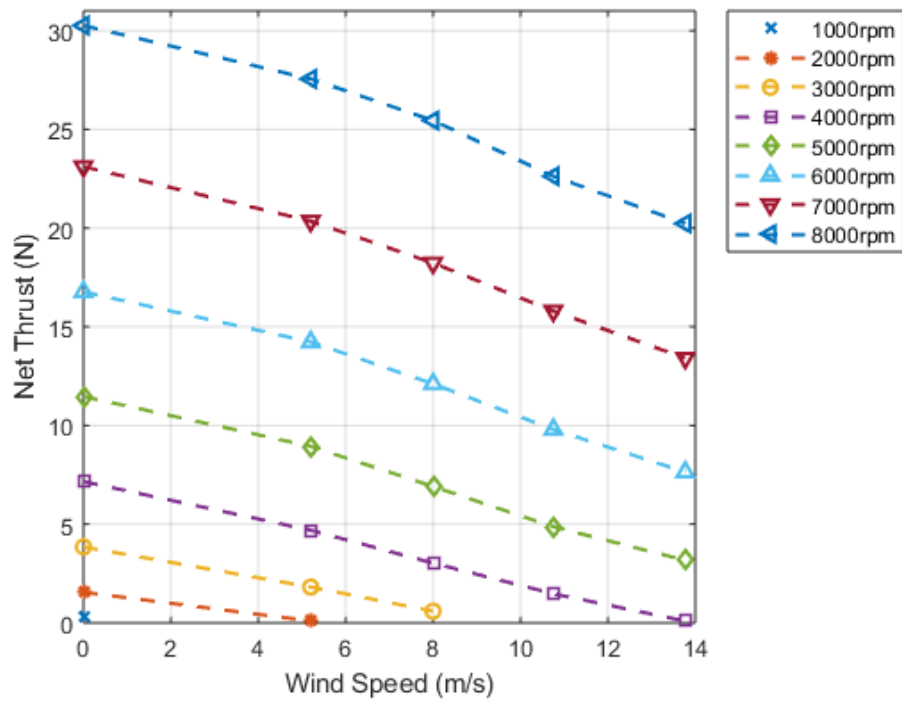


Figure 3.16. Produced net thrust vs wind speed for different rpm values at 90° tilt

Table 3.4. Variation of measurement parameters for 7000 rpm at 90° tilt case

Wind Speed (m/s)	Thrust (N)	Torque (N.m)	Current (A)
0	23.11	0.437	16.9
5.2	20.35	0.443	16.75
8.0	18.23	0.439	16.47
10.75	15.80	0.424	15.64
13.77	13.41	0.434	14.3

When the produced torque measurements are analyzed, it is realized that, it is hard to conclude a trend relative to the wind speed. Although there are small deviations in the produced torque values with various wind speeds, these changes show difference at different rpm values and tilt cases. When the measured torque values at zero wind speed are compared with those at 10.75 and 13.77 m/s wind speed are observed, it is noted that the maximum deviation is less than 0.05 N.m for all tilt and rotational speed cases.

In order to further analyze the effect of the wind speed on the produced torque value, new experiments should be performed with much higher wind speed values. However, this is out of the scope of this thesis. Also, the effect of the wind speed on the produced rotor torque will not have much influence on the overall torque of the aerial vehicle (in forward flight), since the rotors which are symmetrically located at the front left and front right sides of the vehicle rotate contrarily, as will be explained in following sections. Thus, in order to calculate torque value for desired rpm value, the static coefficient of torque calculated by the measured data with no wind speed, will be used in the propulsion model of the vehicle.

Finally, the measured data for the net thrust produced by a single propeller are transported to a three-dimensional look up table, with dimensions of rpm², relative airspeed and tilt angle of the propeller. Thus, a net thrust value of a propeller is computed for assigned tilt angle, relative airspeed and rpm values through the look up table by using cubic spline interpolation and extrapolation method which is available in MATLAB/Simulink software. The relative airspeed of a rotor and the angle

between the relative airspeed and the axis of rotation of the rotor is calculated by using tilt angle of a rotor and body velocity vector of the vehicle. The torque values are calculated by using the (static) torque coefficient that is given in Equation 3.37. The system diagram for the propulsion system is shown in Figure 3.17.

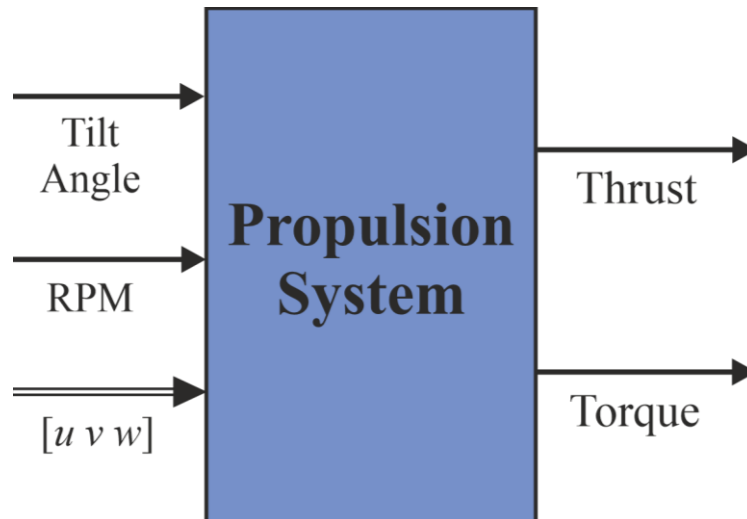


Figure 3.17. Illustration of a propulsion system (a single motor-propeller pair)

3.4.2 Multirotor (Propulsive) Model

The designed tricopter module is shown in Figure 3.18 and in Figure 3.19 with sizing parameters. Rotor rotation and tilt directions are also given in Figure 3.18. Three identical motor-propeller pairs consist of two independently tilting rotors around the y-axis of the rotor mounts in the front and a fixed rotor at the rear. In forward flight, the front rotors are tilted 90 degrees towards the nose of the vehicle to supply required longitudinal thrust and the rear rotor is turned off since the wing module will produce necessary lift to keep height. In hover flight, the torques generated by the rotation of the front rotors are compensated by rotating them in opposite directions. Extra unmatched torque created by the third rear rotor is cancelled out by creating a compensating yaw moment by inversely tilting the front rotors in a proper manner.

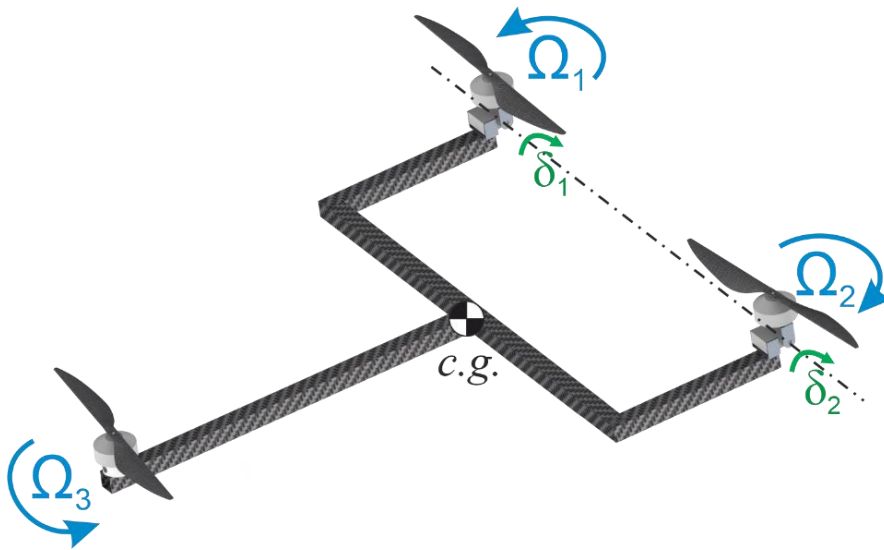


Figure 3.18. Tricopter configuration

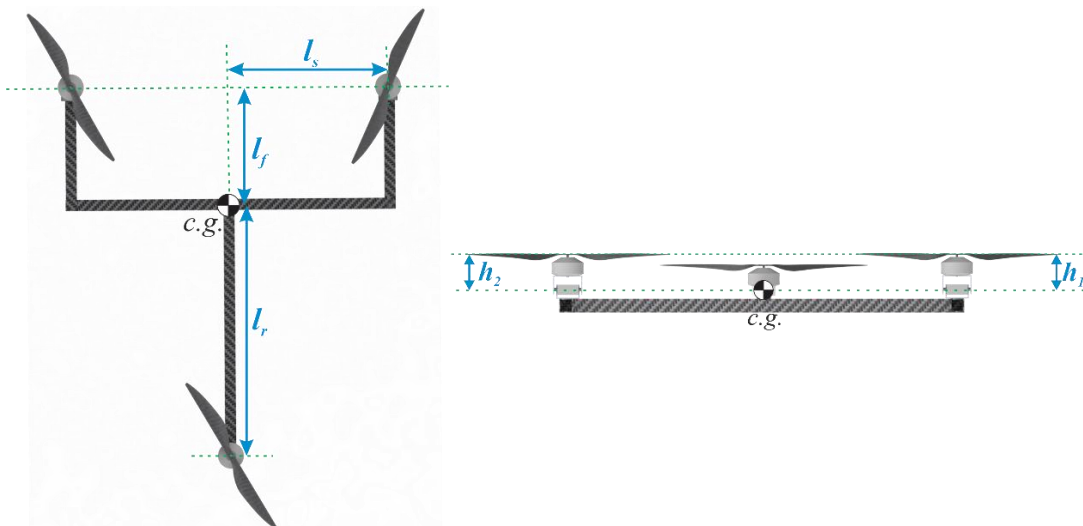


Figure 3.19. Top and front view with sizing parameters

The force and moments correspond to control the altitude and attitude of the vehicle in hover flight. Ascending or descending the altitude is controlled by increasing or decreasing the rpms of three rotors together. Roll motion is mainly controlled by using differential thrust between the front rotors, pitch motion is mainly controlled by differential thrust between front rotors and rear rotor and lastly the yaw motion is

controlled by differential tilt of the two front rotors. Motion control maneuvers are illustrated in Figure 3.20. Also, forward transition is controlled by the force created in x_B – direction of the vehicle which is produced by tilting the front rotors together.

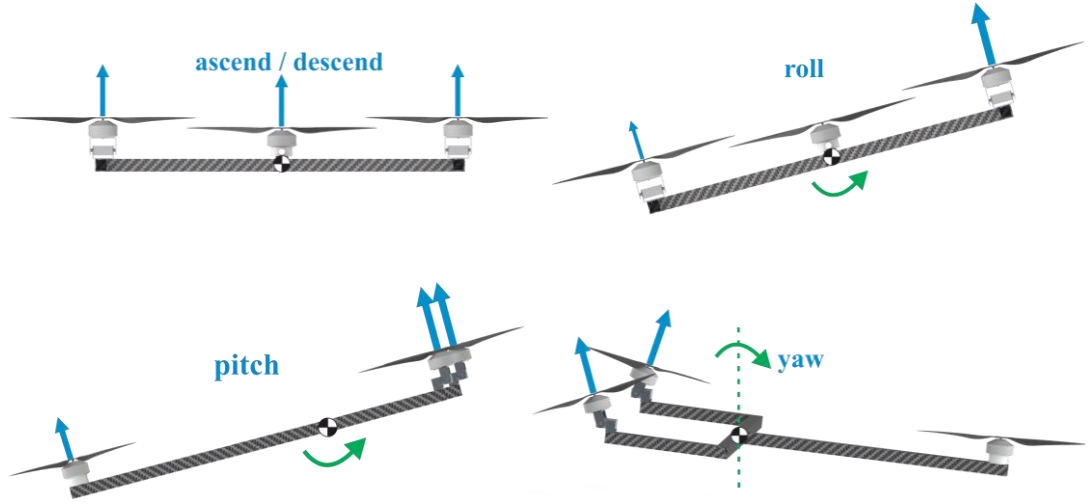


Figure 3.20. Altitude and attitude motion control

Propulsive force and moments are generated by combination of rpms of three rotors and tilt angles of the front two rotors. All these force and moments are represented in Equation (3.38) in a matrix notation. No force is generated in y_B – direction since any of the rotors are directed in this direction. Mean tilt angle δ_t is a known and assignable variable to control transitioning from hover flight to forward flight or vice versa. The mean tilt angle is 0° in hover and 90° in forward flight.

$$\begin{bmatrix} X_p \\ Z_p \\ L_p \\ M_p \\ N_p \end{bmatrix} = \begin{bmatrix} k_f & 0 & k_f & 0 & 0 \\ 0 & -k_f & 0 & -k_f & -k_f \\ -k_t & l_s k_f & k_t & -l_s k_f & 0 \\ -h_1 k_f & l_f k_f & -h_2 k_f & l_f k_f & -l_r k_f \\ l_s k_f & k_t & -l_s k_f & -k_t & k_t \end{bmatrix} \begin{bmatrix} \Omega_1^2 \sin \delta_1 \\ \Omega_1^2 \cos \delta_1 \\ \Omega_2^2 \sin \delta_2 \\ \Omega_2^2 \cos \delta_2 \\ \Omega_3^2 \end{bmatrix} \quad (3.38)$$

Knowing that, tilt angles of the first and second rotors are summation/subtraction of differential tilt angle δ to/from the mean tilt angle δ_t .

$$\delta_1 = \delta_t - \delta \quad (3.39)$$

$$\delta_2 = \delta_t + \delta \quad (3.40)$$

In order to retrieve desired rotor rpms and differential tilt angle δ , to generate necessary force and moments to maintain or act a maneuver, the force and moment vector is multiplied by a proper inverse of the coefficient matrix. Because of presence of four unknowns corresponding to four equations.

The propulsive model block is depicted in Figure 3.21. It includes the propulsion system (Figure 3.17) as a subsystem to calculate dynamic thrust of a propeller for an assigned relative airspeed. Specifying the rpms of the rotors and the tilt angles with the body velocities of the vehicle, the propulsive system block calculates the all the propulsive forces and moments generated by the three of motor-propeller pairs.

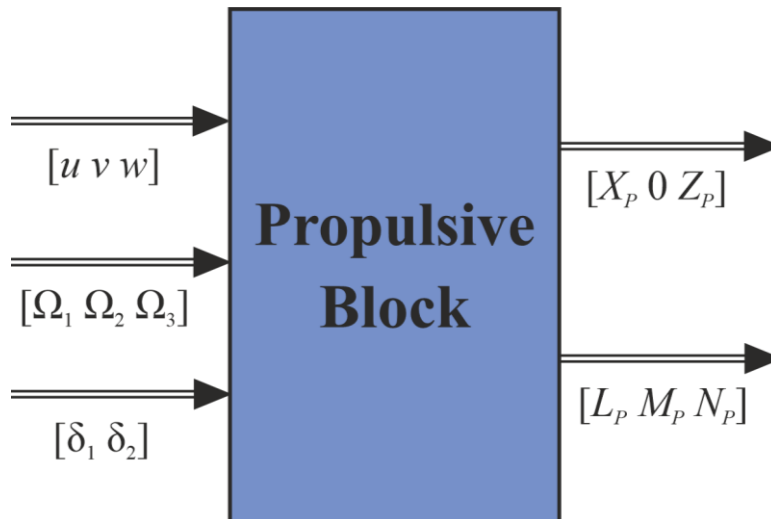


Figure 3.21. Propulsive model (tilt-rotor tricopter) of the hybrid UAV

3.5 Mathematical Model of Fixed-Wing Module

3.5.1 Sign Conventions

Angle of attack and sideslip angle are two important aerodynamic angles. Aerodynamic forces and moments are expressed as a function of aerodynamic angles. The angle between projection of local air velocity onto the plane of symmetry of the vehicle and the body x -axis is the angle of attack. Also, the angle between the projection of local air velocity onto the xy -plane of the vehicle and the body x -axis is the sideslip angle. The two angles are illustrated in Figure 3.22.

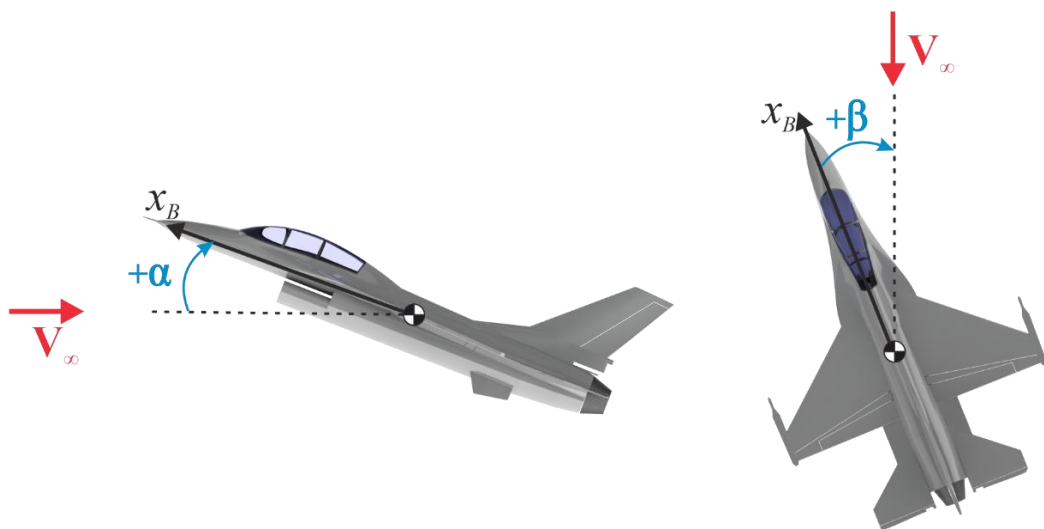


Figure 3.22. Convention for angle of attack and sideslip angle

Conventional airplanes basically have three important control surfaces, aileron, elevator, rudder that is intended to adjust aerodynamic roll, pitch and yaw moments, respectively. A positive deflection is performed for producing a negative moment in body axes, according the right-hand rule. For example, tilting elevator downward in a level flight, causes a negative pitching moment in y_B – axis, thus it is denoted as a

positive elevator deflection. The same convention is valid for aileron and rudder deflections. The sign conventions for control surfaces are illustrated in Figure 3.23.

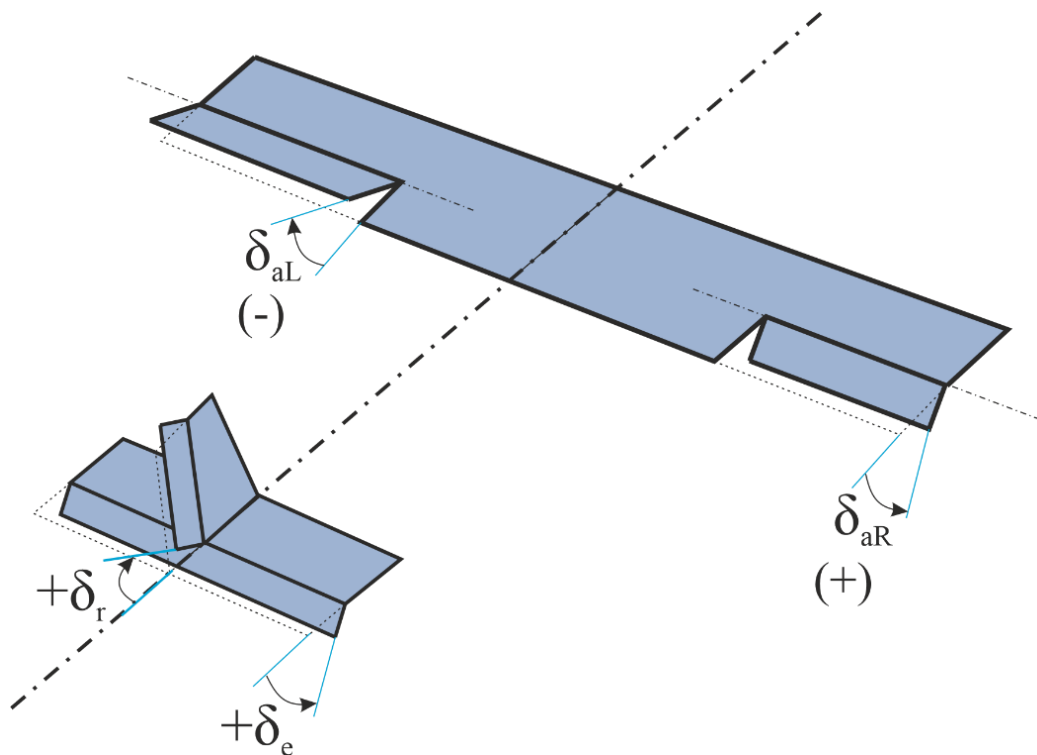


Figure 3.23. Sign convention for control surface deflections

The two aileron surfaces at both sides of wing, are tilted in asymmetric convention, such that in opposite directions. The relation for aileron deflection may be written as:

$$\delta_a = \frac{1}{2}(\delta_{aR} - \delta_{aL}) \quad (3.41)$$

Table 3.5. Effect of control surfaces on the vehicle attitude

Movement	Control Surfaces
(-) Roll	Ailerons (+ δ)
(-) Pitch	Elevator (+ δ)
(-) Yaw	Rudder (+ δ)

3.5.2 Aerodynamic Simulation of the Fixed-Wing Model

Mathematical model of a fixed-wing module is needed for analyzing the transition and cruising flights. The most precise way is to make wind tunnel tests and obtain aerodynamic properties such as non-dimensional force-moment coefficients, stability and control derivatives of an aerial vehicle. However, performing a wind tunnel experiment is an expensive, difficult and time-consuming way which is unnecessary to be performed at early design phases. Computational methods are more suitable, not requiring production of a physical prototype but only a 3D CAD model.

Among numerical approaches, Computational Fluid Dynamics (CFD) methods provide more accurate results. Unfortunately, to have confidential results, a good theory and methodology knowledge is needed. Additionally, requirement of high computational power may be difficult and time consuming in preliminary design stages.

Among the other methods, Panel Method and Vortex Lattice Method (VLM) provide computationally inexpensive and pretty sufficient results in subsonic regime. Although, possibility of underestimating the total drag, they give precise enough results for most applications [83]. VLM and panel methods are based on solutions to Laplace's equation for incompressible, irrotational potential flow. The viscous effects are neglected as well.

XFLR5 which is as an open source project that released under GNU general public license, offers to use the described methods to analyze 2D and 3D airfoils and wing geometries. It is based on XFOIL algorithm. There are numerous R/C model airplane examples designed and built by using VLM and panel methods. Comparisons between computational results show consistency with the experimental outputs [84]. The code has been utilized in variety of studies aiming for analyzing the lifting surfaces [3,37, 45,85,86].

In this study, the designed fixed wing module is generated in XFLR5 user interface with the given design parameters. The 3D CAD model does not include the fuselage and propellers, but the main lifting surfaces, wing and tail. Otherwise, it may cause some numerical errors. The simulation is performed for a range of α and β to obtain aerodynamic coefficients and stability derivatives which are independent of flight velocity. Aerodynamic angle resolution is 1° for α and is 15° for β . In addition, the control derivatives are calculated for the measured α and β ranges by tilting control surfaces individually an amount relative to no tilt cases in the range.

Table 3.6. Simulation conditions for variable ranges

Parameters	Range
Angle of Attack, α	$-15^\circ < \alpha < 15^\circ$
Sideslip Angle, β	$-45^\circ < \beta < 45^\circ$
Control Surface Deflections	$-1^\circ \leq \delta_{deflection} \leq 1^\circ, \Delta\delta_{deflection} = 1^\circ$

3D mesh element view of the modules are shown in Figure 3.24. The determination of the panel numbers is performed such that, the panel numbers are increased until the results has converged. The model is composed of 979 mesh element. The calculation time is increased as the panel number is increased, as expected. The 3D view of the wing – tail modules of the vehicle with the streamline flow and produced lift force is depicted in the Figure 3.25.

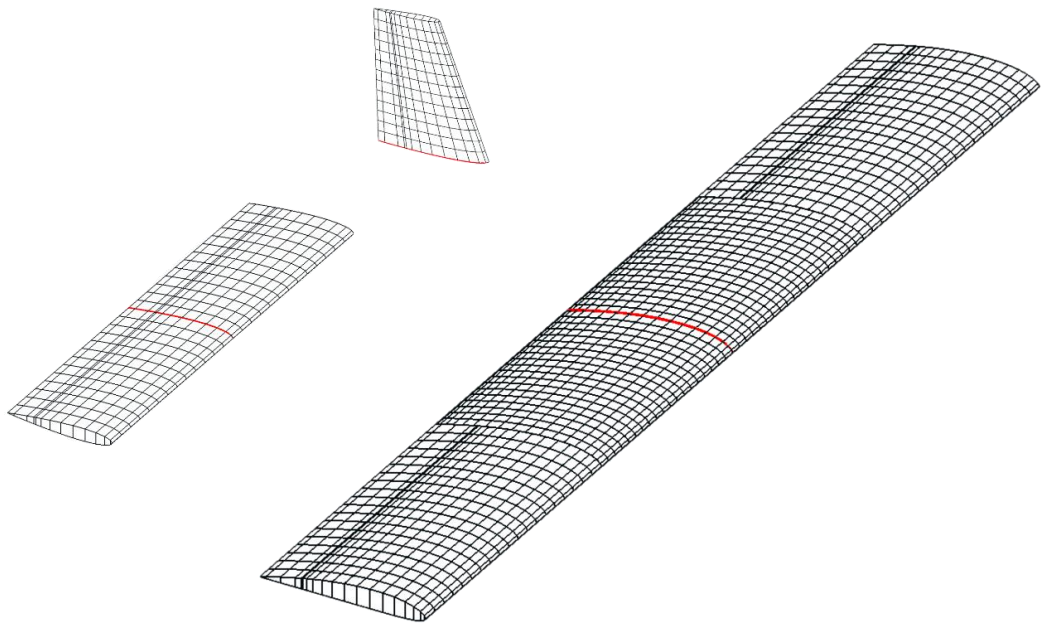


Figure 3.24. 3D mesh view of the wing, horizontal and vertical tails

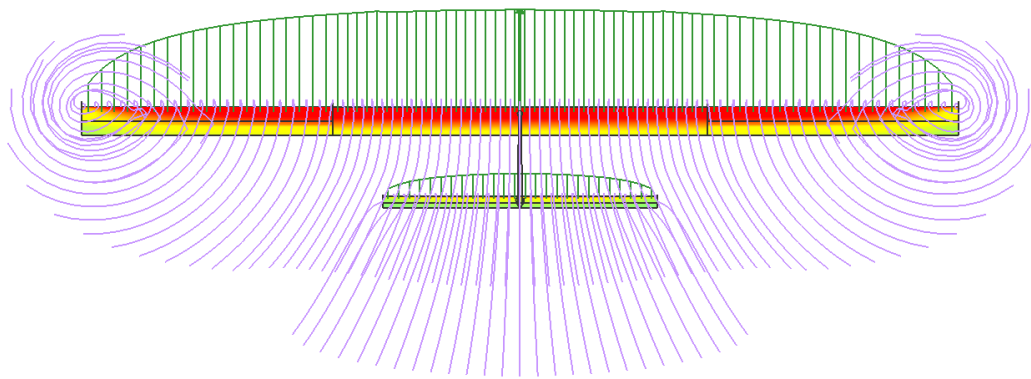


Figure 3.25. 3D view of the XFLR5 model with produced lift and streamlines (with $\alpha = 10^\circ$ assigned)

3.5.3 Aerodynamic Coefficients

Aerodynamic model of the aerial vehicle is obtained by calculating 3 axes force and 3 axes moment equations. These equations are the aerodynamic parts (\mathbf{F}_A and \mathbf{G}_A) of the forces and moments given in Equations 3.28 and 3.31. The aerodynamic force equations in body reference frame are given as,

$$X_A = \frac{1}{2} \rho V^2 S C_X \quad (3.42)$$

$$Y_A = \frac{1}{2} \rho V^2 S C_Y \quad (3.43)$$

$$Z_A = \frac{1}{2} \rho V^2 S C_Z \quad (3.44)$$

Similarly, the aerodynamic moment equations in body reference frame are given as,

$$L_A = \frac{1}{2} \rho V^2 S b C_L \quad (3.45)$$

$$M_A = \frac{1}{2} \rho V^2 S \bar{c} C_M \quad (3.46)$$

$$N_A = \frac{1}{2} \rho V^2 S b C_N \quad (3.47)$$

where; ρ , V and S indicate density of air, airspeed and wing planform area, respectively. In addition, the variables b and \bar{c} given in moment equations indicate the span and mean aerodynamic chord of the wing, respectively.

Knowing non-dimensional aerodynamic force-moment coefficients, the forces and moments of a vehicle can be calculated for different altitude and speed conditions. These coefficients are obtained by using XFLR5 software. The aerodynamic coefficients that calculated by the software are transformed into the body axes by using transformation matrices. They are dependent on aerodynamic angles and control surface deflections, basically. Simulating a vehicle for ranges of aerodynamic angles and control surface deflections, the aerodynamic coefficients could be calculated for

desired α , β and control surface deflections. By this way, the mathematical model of an aerial vehicle aerodynamics is obtained.

An aerodynamic coefficient, for instance, drag coefficient may be expressed as,

$$C_X = C_{X_0} + \Delta C_X \quad (3.48)$$

Here, C_{X_0} should not be confused with parasite drag. In this context, it indicates the drag coefficient with zero α , β and with no control surface deflections. The change in aerodynamic coefficients with respect to aerodynamic angles and control surface deflections may be expressed as,

$$\Delta C_X = C_X(\alpha, \beta) + C_{X_{\delta a}} \delta a + C_{X_{\delta e}} \delta e + C_{X_{\delta r}} \delta r \quad (3.49)$$

The variation of aerodynamic coefficients with respect to mentioned variables is given in Table 3.7. Some variations in the equations are too little such that can be neglected.

Table 3.7. Variation of aerodynamic coefficients with respect to variables [86]

Aerodynamic F&M	$\alpha = \beta = 0$ $\delta_a = \delta_e = \delta_r = 0$	α	β	δ_a	δ_e	δ_r
X_A	drag force at zero value for all variables	induced drag force due to α	drag force due to β	negligible for small δ_a	negligible for small δ_e	negligible for small δ_r
Y_A	zero	side force due to α	side force due to β	zero	zero	side force due to δ_r
Z_A	lift force at zero value for all variables	lift force due to α	lift force due to β	negligible	lift force due to δ_e	zero
L_A	zero	rolling moment due to sideslip affected by α	rolling moment due to β	rolling moment due to δ_a	zero	rolling moment due to δ_r
M_A	pitching moment at zero for all variables	pitching moment due to α	pitching moment due to β	negligible	pitching moment due to δ_e	negligible
N_A	zero	yawing moment due to sideslip affected by α	yawing moment due to β	yawing moment due to δ_a	zero	yawing moment due to δ_r

Subsequently, 6 individual 2D interpolation lookup tables corresponding to α and β are generated to retrieve aerodynamic coefficients for any desired α and β value. In other words, aerodynamic force and moment coefficients are expressed in terms of lookup tables. In order to find control derivatives of aileron, elevator and rudder deflections, each control surface is deflected individually (both in positive and negative directions). Furthermore, the effects of control surfaces on aerodynamic coefficients are implemented to the model by using calculated control derivatives. Aerodynamic coefficients with no control surface deflections are plotted versus α and β (in body axes) through the Figures 3.26 and 3.28 in three-dimensional view.

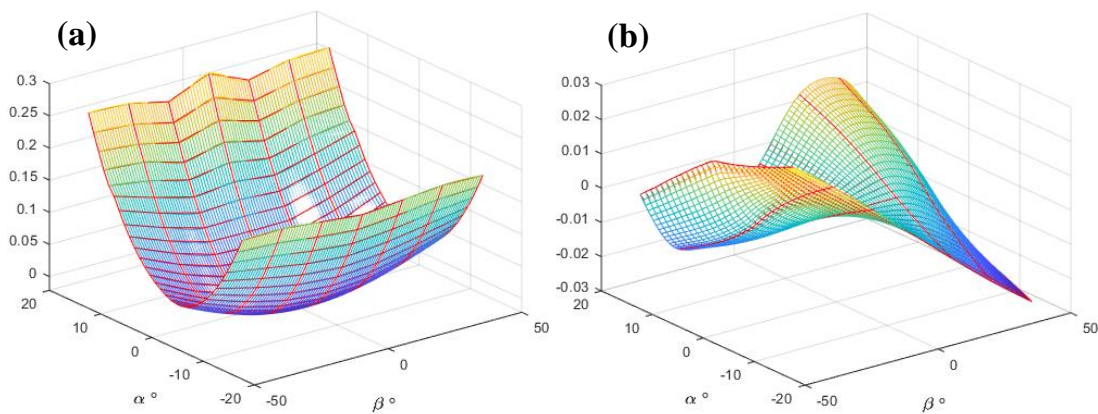


Figure 3.26. (a) C_X and (b) C_L versus α and β with no control surface deflection

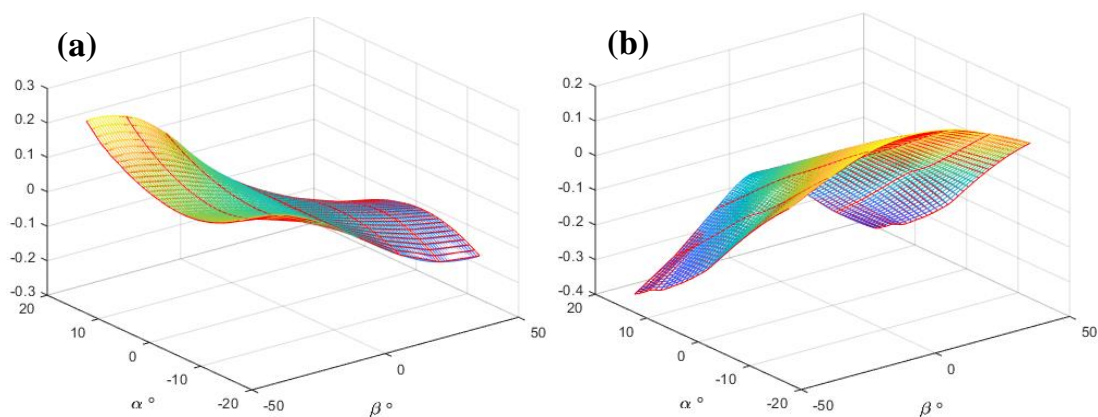


Figure 3.27. (a) C_Y and (b) C_M versus α and β with no control surface deflection

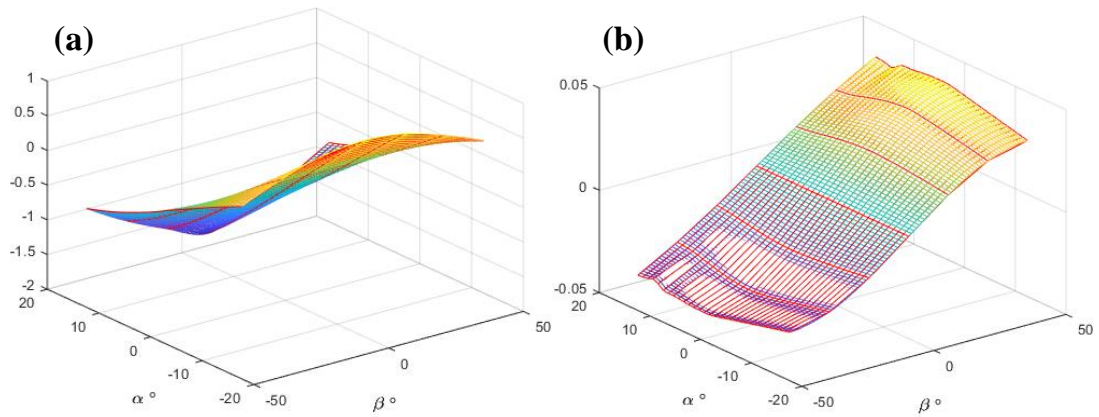


Figure 3.28. (a) C_Z and (b) C_N versus α and β with no control surface deflection

3.5.4 Aerodynamic Control Derivatives

As stated in the previous section, to find overall aerodynamic coefficients of the vehicle (Equations 3.42 through 3.47 and 3.49), the effect of aerodynamic angles and control surface deflections should be revealed. The calculated lookup tables of aerodynamic coefficients for α versus β , include the effects of change of α and β . Thus, it is not needed to recalculate stability derivatives. However, the control derivatives should be extracted. In order to calculate the control derivatives C_{δ_a} , C_{δ_e} and C_{δ_r} , again the aerodynamic coefficient data are used. Also, it is assumed that the effect of the control surface deflection will vary linearly with the variation of deflection. A control derivative may be calculated by the following formula.

$$C_{\delta} = \frac{\partial C}{\partial \delta} = \frac{C_2 - C_1}{\delta_2 - \delta_1} \left(\frac{1}{\text{deg}} \right) \text{ or } \left(\frac{1}{\text{rad}} \right) \quad (3.50)$$

Control derivatives of aileron, elevator and rudder are computed simply by dividing the difference between no tilt and tilted case of nondimensional coefficients to the amount of tilt for that specific control surface. This may be expressed as:

$$C_{\delta_a} = \frac{C_{\delta_a=1^\circ, \delta_e=0^\circ, \delta_r=0^\circ} - C_{\delta_a=0^\circ, \delta_e=0^\circ, \delta_r=0^\circ}}{1^\circ} \left(\frac{1}{\text{deg}} \right) \quad (3.51)$$

$$C_{\delta_e} = \frac{C_{\delta_a=0^\circ, \delta_e=1^\circ, \delta_r=0^\circ} - C_{\delta_a=0^\circ, \delta_e=0^\circ, \delta_r=0^\circ}}{1^\circ} \left(\frac{1}{\text{deg}} \right) \quad (3.52)$$

$$C_{\delta_r} = \frac{C_{\delta_a=0^\circ, \delta_e=0^\circ, \delta_r=1^\circ} - C_{\delta_a=0^\circ, \delta_e=0^\circ, \delta_r=0^\circ}}{1^\circ} \left(\frac{1}{\text{deg}} \right) \quad (3.53)$$

Table 3.8. Values of calculated aerodynamic control derivatives

Aileron		Elevator		Rudder	
$C_{X_{\delta_a}}$	<i>neglect</i>	$C_{X_{\delta_e}}$	<i>neglect</i>	$C_{X_{\delta_r}}$	<i>neglect</i>
$C_{Y_{\delta_a}}$	0	$C_{Y_{\delta_e}}$	0	$C_{Y_{\delta_r}}$	0.00146
$C_{Z_{\delta_a}}$	<i>neglect</i>	$C_{Z_{\delta_e}}$	-0.00652	$C_{Z_{\delta_r}}$	0
$C_{L_{\delta_a}}$	-0.00657	$C_{L_{\delta_e}}$	0	$C_{L_{\delta_r}}$	<i>neglect</i>
$C_{M_{\delta_a}}$	<i>neglect</i>	$C_{M_{\delta_e}}$	-0.02217	$C_{M_{\delta_r}}$	<i>neglect</i>
$C_{N_{\delta_a}}$	<i>neglect</i>	$C_{N_{\delta_e}}$	0	$C_{N_{\delta_r}}$	-0.00082

3.5.5 Nondimensional and Dimensional Stability Derivatives

Nondimensional stability derivatives are partial derivatives of force and moment coefficients (C_X , C_M and etc.) with respect to nondimensional motion variables ($\hat{u}, \hat{v}, \hat{w}, \hat{a}, \hat{q}, \hat{\beta}, \hat{p}, \hat{r}$) [79].

$$C_{z_u} = \frac{\partial C_Z}{\partial \hat{u}} \quad (3.54)$$

where
$$\hat{u} = \frac{u}{V} \quad \text{or} \quad \hat{u} = \frac{u}{u_0} \quad (3.55)$$

Also, these force and moment coefficients are nondimensionalized by some divisors. For the aerodynamic forces X, Y and Z, the divisor of dynamic pressure times

reference wing area ($0.5 \times \rho V^2 S$) is used. For the pitching moment this divisor is multiplied by the mean chord length of the wing and for the rolling and yawing moments the divisor is multiplied by the length of wing span.

Nondimensional stability derivatives are calculated by XFLR5 and reported here.

Table 3.9. Nondimensional longitudinal derivatives

	X		Z		M
C_{X_u}	-0.012429	C_{Z_u}	-0.0001441	C_{M_u}	2.7603×10^{-7}
C_{X_α}	0.19059	C_{Z_α}	4.746	C_{M_α}	-1.3188
C_{X_q}	neglect	C_{Z_q}	8.0267	C_{M_q}	-15.594

Table 3.10. Nondimensional lateral derivatives

	Y		L		N
C_{Y_β}	-0.13497	C_{L_β}	-0.0079662	C_{N_β}	0.075766
C_{Y_p}	0.014249	C_{L_p}	-0.47736	C_{N_p}	-0.059061
C_{Y_r}	0.15724	C_{L_r}	0.10217	C_{N_r}	-0.088392

The calculation of the longitudinal and lateral dimensional stability derivatives [79] are given in the Table 3.11 and 3.12.

Table 3.11. Nondimensional stability derivatives of longitudinal parameters

	X	Z	M
u	$\rho u_0 S \left(C_{w_0} \sin \theta_0 + \frac{1}{2} C_{X_u} \right)$	$-\rho u_0 S \left(C_{w_0} \cos \theta_0 + \frac{1}{2} C_{Z_u} \right)$	$\frac{1}{2} \rho u_0 S \bar{c} C_{M_u}$
w	$\frac{1}{2} \rho u_0 S C_{X_\alpha}$	$\frac{1}{2} \rho u_0 S C_{Z_\alpha}$	$\frac{1}{2} \rho u_0 S \bar{c} C_{M_\alpha}$
q	$\frac{1}{4} \rho u_0 S \bar{c} C_{X_q}$	$\frac{1}{4} \rho u_0 S \bar{c} C_{Z_q}$	$\frac{1}{4} \rho u_0 S \bar{c}^2 C_{M_q}$

Where nondimensional weight coefficient is $C_{w_0} = 2mg / \rho u_0^2 S$.

Table 3.12. Nondimensional stability derivatives of lateral parameters

	Y	L	N
v	$\frac{1}{2} \rho u_0 S C_{Y_\beta}$	$\frac{1}{2} \rho u_0 S b C_{L_\beta}$	$\frac{1}{2} \rho u_0 S b C_{N_\beta}$
p	$\frac{1}{4} \rho u_0 S b C_{Y_p}$	$\frac{1}{4} \rho u_0 S b^2 C_{L_p}$	$\frac{1}{4} \rho u_0 S b^2 C_{N_p}$
r	$\frac{1}{4} \rho u_0 S b C_{Y_r}$	$\frac{1}{4} \rho u_0 S b^2 C_{L_r}$	$\frac{1}{4} \rho u_0 S b^2 C_{N_r}$

Aerodynamic model of the fixed-wing module of the vehicle is shown in Figure 3.29. Inserting aerodynamic angles and control derivatives beside the air density, airspeed, and some design parameters, the subsystems calculates the forces and moments generated by the module.

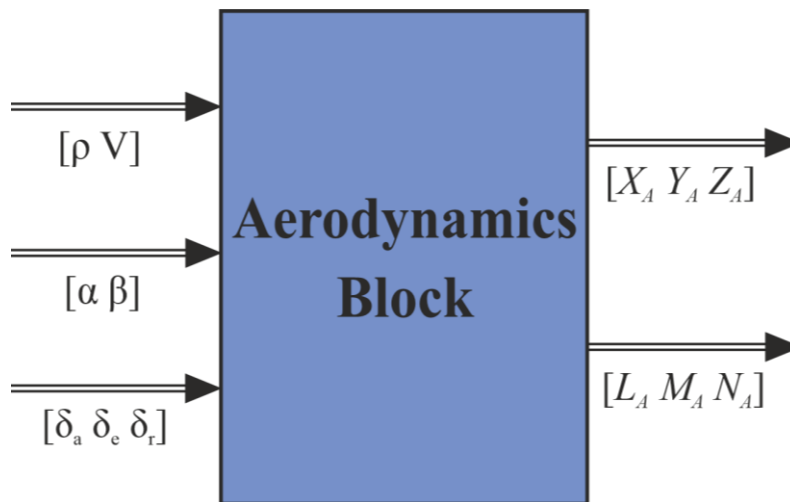


Figure 3.29. Aerodynamic model of Fixed-wing module

3.6 Combining Multirotor and Fixed-Wing Models

In sections 3.4 and 3.5 multicopter and fixed-wing modules of the hybrid VTOL modeling studies have been reported. These models correspond to propulsive and aerodynamic force-moment sources of the hybrid aerial vehicle, respectively. To complete the overall model, the modules are reunited together, adding also the gravity effect. Certainly, gravitational force is expressed in body-fixed frame, like other force and moment sources. Henceforward, the forces and moments produced by propellers, wing, tails and the gravity steer the dynamics of hybrid vehicle. In low speed flights, propulsive forces and moments are dominant however, in high speed regime, the aerodynamic forces and moments control the aerial vehicle and front rotors supply required thrust. The overall nonlinear mathematical model of the hybrid aerial vehicle is depicted in Figure 3.30.

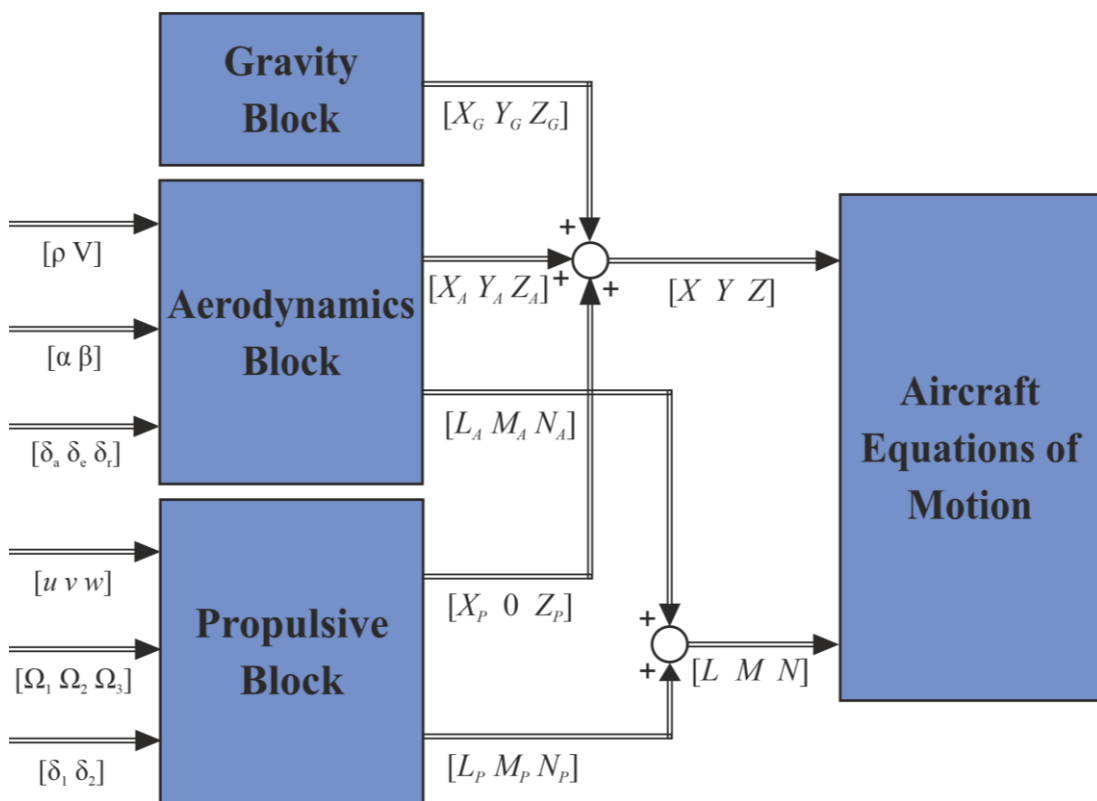


Figure 3.30. Mathematical nonlinear model of the hybrid UAV

3.7 Throttle Model and Actuator Models

In order to have the relation between rotor rpm and throttle command, throttle sub-model is generated. The sub-model will be used in linearization and simulations of the study. The throttle command and experimental data which is reported in Chapter 3.4.1 are used to produce the model. A second order curve is fitted to the throttle – rpm curve by the help of MATLAB and the polynomial constants are obtained. The constants are given as follows.

$$rpm = p_1 \times \delta_p^2 + p_2 \times \delta_p + p_3 \quad (3.56)$$

where $p_1 = -0.193, \quad p_2 = 110.8, \quad p_3 = -12.8 \quad (3.57)$

The experimental data of throttle versus rpm and fitted curve that obtained by the calculated polynomial constants are given in Figure 3.31.

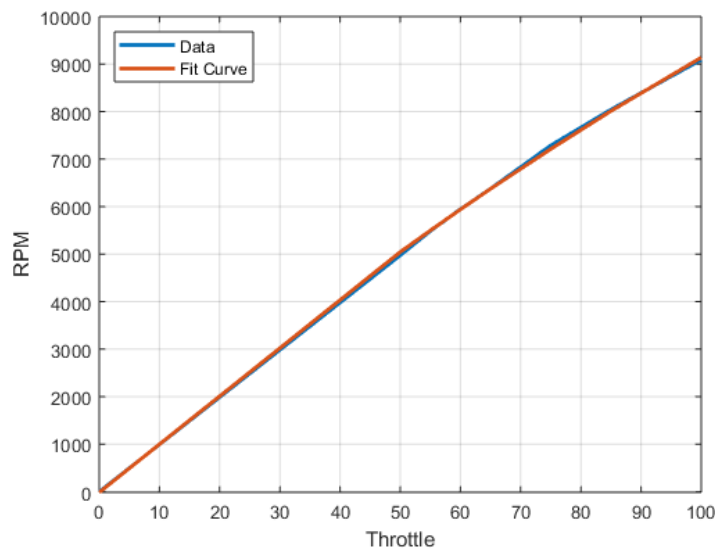


Figure 3.31. Experimental throttle data and fitted curve

Also, to represent actuator dynamics $1/(0.05s+1)$ transfer function is used for motor and tilt servos. For aileron, elevator and rudder servos (which have faster response time) $1/(0.02s+1)$ transfer function is used.

CHAPTER 4

TRIMMING, LINEARIZATION AND STABILITY ANALYSIS

In stability analysis and control system design, linearized model of nonlinear dynamics is important. For this reason, the nonlinear equations of motion describing the aircraft dynamics are linearized around some specific points and the linear model is approximate enough in a region around linearization point to represent the real model. These specific points mentioned that the systems are linearized around them are equilibrium points i.e. trim points.

In this chapter, trim conditions are specified for different flight modes of the nonlinear mathematical model of the aerial vehicle. The linearization of nonlinear mathematical model is performed around the specified trim points in order to analyze the stability and to design linear controllers.

4.1 Trimming

An aircraft has infinitely many trim points. In a trim point of an aircraft all of the resultant forces and moments that act on the aerial vehicle are equal to zero. Also, the state derivatives are zero. The aerial vehicle flies with constant translational velocity (no circular motion) in forward flight or just suspending with no velocity in the air in hover flight mode. The predetermined state and control parameters are defined in Tables 4.1 and 4.2.

Table 4.1. Predetermined state parameters in trim condition

Hover mode	Fixed-wing mode
$\dot{u} = \dot{v} = \dot{w} = 0$ $\dot{p} = \dot{q} = \dot{r} = 0$	$\dot{u} = \dot{v} = \dot{w} = 0$ $\dot{p} = \dot{q} = \dot{r} = 0$
$u = v = w = 0$ $p = q = r = 0$	$u = u_e, v = 0, w = w_e$ $p = q = r = 0$
$X = Y = 0, Z = Z_e$ $L = M = N = 0$	$X = X_e, Y = 0, Z = Z_e$ $L = M = N = 0$
$\phi = 0, \theta = \theta_e, \psi = \psi_e$	$\phi = 0, \theta = \theta_e, \psi = \psi_e$

Table 4.2. Predetermined control variables in trim condition

Hover mode	Fixed-wing mode
$\Omega_1 = \Omega_{1e}, \Omega_2 = \Omega_{2e}, \Omega_3 = \Omega_{3e}$	$\Omega_1 = \Omega_{1e}, \Omega_2 = \Omega_{2e}, \Omega_3 = 0$
$\delta_t = 0^\circ, \delta = \delta_e^\circ$	$\delta_t = 90^\circ, \delta = 0^\circ$
$\delta a = 0^\circ, \delta e = \delta e_e^\circ, \delta r = 0^\circ$	$\delta a = 0^\circ, \delta e = \delta e_e^\circ, \delta r = 0^\circ$

After constraining the trim state and control parameters, they are inserted into the equations of motion defined in Equations between 3.28 - 3.31. The most suitable parameters are selected among the available trim point parameters. The parameters of trim condition for the two flight modes are tabulated in Table 4.3.

Table 4.3. Trim variables for flight modes

Trim variables		Flight modes		Unit
		Hover	Fixed-wing	
Aerodynamic variables	u	0	18.2	m/s
	v	0	0	m/s
	w	0	-0.13	m/s
	ϕ	0	0	deg
	θ	0	-0.4	deg
	ψ	0	0	deg

Control variables	Ω_1	5277	5111	<i>rpm</i>
	Ω_2	5284	5111	<i>rpm</i>
	Ω_3	5279	0	<i>rpm</i>
	δ_t	0	90	<i>deg</i>
	δ	1.50	0	<i>deg</i>
	δ_a	ineffective	0	<i>deg</i>
	δ_e		1.87	<i>deg</i>
	δ_r		0	<i>deg</i>

4.2 Linearization

The aerial vehicle has nonlinear equations of motion. Analyzing stability of a nonlinear system may be rather complicated and difficult due to using exact representation of the complicated vehicle dynamics. For the purpose of simplifying the stability analysis and designing a control system for the vehicle in an operation region, the nonlinear system could be linearized around trim points. Linearization is useful in much engineering applications and the linearized system is valid enough to represent the original system in a neighborhood of the trim points. In addition, linear systems allow to use linear controllers which are easier and inexpensive way to develop controllers. In this part, the vehicle dynamics are linearized for the multicopter mode (hovering) and fixed-wing mode (cruising) at the trim points that are specified in previous part.

State vector of the system and state vector for navigation equations are specified as:

$$\mathbf{x} = [u \ v \ w \ p \ q \ r \ \phi \ \theta]^T \in \mathbb{R}^8 \quad (4.1)$$

$$\mathbf{x}_N = [\psi \ x_E \ y_E \ z_E]^T \in \mathbb{R}^4 \quad (4.2)$$

Virtual control input vector in terms of aeropropulsive forces and moments is specified as:

$$\mathbf{u}^* = [X \ Y \ Z \ L \ M \ N]^T \in \mathbb{R}^6 . \quad (4.3)$$

However, the real input vector should be given in terms of actuators. The control input vectors are given for the multicopter and the fixed-wing modes as follows:

$$\mathbf{u}_{MC} = [\Omega_1^2 \ \Omega_2^2 \ \Omega_3^2 \ \delta]^T \in \mathbb{R}^4 \quad (4.4)$$

$$\mathbf{u}_{FW} = [\delta_a \ \delta_e \ \delta_r \ \delta_p]^T \in \mathbb{R}^4 \quad (4.5)$$

Derivative of the state vector is a function of the state and input variables.

$$\dot{\mathbf{x}} = f(\mathbf{x}, \mathbf{u}) \quad (4.6)$$

Below, the linear system is expressed in the form of state space representation.

$$\dot{\mathbf{x}} = \mathbf{Ax} + \mathbf{Bu} \quad (4.7)$$

$$\mathbf{y} = \mathbf{Cx} + \mathbf{Du} \quad (4.8)$$

The Small-Perturbation Theory is utilized to linearize system. Each state is perturbed from the reference circumstance of steady flight by very small disturbances. Thereafter, the equations are expanded by using Taylor series expansion method and high order derivative terms are discarded. In addition, the atmosphere is assumed to be still.

$$\mathbf{x} = \mathbf{x}_e + \Delta\mathbf{x} \quad (4.9)$$

$$f(\mathbf{x}_e + \Delta\mathbf{x}, \mathbf{u}_e + \Delta\mathbf{u}) = f(\mathbf{x}_e, \mathbf{u}_e) + \left. \frac{\partial f(\mathbf{x}, \mathbf{u})}{\partial \mathbf{x}} \right|_{\substack{\mathbf{x}=\mathbf{x}_e \\ \mathbf{u}=\mathbf{u}_e}} \Delta\mathbf{x} + \left. \frac{\partial f(\mathbf{x}, \mathbf{u})}{\partial \mathbf{u}} \right|_{\substack{\mathbf{x}=\mathbf{x}_e \\ \mathbf{u}=\mathbf{u}_e}} \Delta\mathbf{u} + \text{H.O.T.} \quad (4.10)$$

Here, \mathbf{A} and \mathbf{B} matrices become the first order derivative terms and can be defined as:

$$\mathbf{A} = \left. \frac{\partial f(\mathbf{x}, \mathbf{u})}{\partial \mathbf{x}} \right|_{\substack{x=x_e \\ u=u_e}} = \begin{bmatrix} \frac{\partial f_1}{\partial x_1} & \dots & \frac{\partial f_1}{\partial x_n} \\ \vdots & \ddots & \vdots \\ \frac{\partial f_n}{\partial x_1} & \dots & \frac{\partial f_n}{\partial x_n} \end{bmatrix} \quad (4.11)$$

$$\mathbf{B} = \left. \frac{\partial f(\mathbf{x}, \mathbf{u})}{\partial \mathbf{u}} \right|_{\substack{x=x_e \\ u=u_e}} = \begin{bmatrix} \frac{\partial f_1}{\partial u_1} & \dots & \frac{\partial f_1}{\partial u_n} \\ \vdots & \ddots & \vdots \\ \frac{\partial f_n}{\partial u_1} & \dots & \frac{\partial f_n}{\partial u_n} \end{bmatrix}_{\substack{x=x_e \\ u=u_e}} \quad (4.12)$$

Furthermore, the system matrix \mathbf{A} , can be divided into two parts. First part, \mathbf{A}_1 is obtained by taking the first order derivatives of functions of pure state variables. Similarly, the second, \mathbf{A}_2 is calculated by taking first order derivatives of functions of pure virtual control input variables (forces and moments). However, these variables do not include the forces and moments produced by control actuators. It may be expressed as:

$$\mathbf{A} = \left. \frac{\partial f(\mathbf{x}, \mathbf{u})}{\partial \mathbf{x}} \right|_{\substack{x=x_e \\ u=u_e}} = \mathbf{A}_1 + \mathbf{A}_2 = \left. \frac{\partial f(\mathbf{x})}{\partial \mathbf{x}} \right|_{x=x_e} + \left. \frac{\partial f(\mathbf{x}, \mathbf{u})}{\partial \mathbf{x}} \right|_{x=x_e} \quad (4.13)$$

The linear forces and moments used in EoMs may be expressed in terms of dimensional derivatives as:

$$\Delta X = X_u \Delta u + X_w \Delta w + \cancel{Z_q \Delta q} + \Delta X_c \quad (a)$$

$$\Delta Y = Y_v \Delta v + Y_p \Delta p + Y_r \Delta r + \Delta Y_c \quad (b)$$

$$\Delta Z = Z_u \Delta u + Z_w \Delta w + \cancel{Z_w \Delta w} + Z_q \Delta q + \Delta Z_c \quad (c)$$

$$\Delta L = L_v \Delta v + L_p \Delta p + L_r \Delta r + \Delta L_c \quad (d)$$

$$\Delta M = M_u \Delta u + M_w \Delta w + \cancel{M_w \Delta w} + M_q \Delta q + \Delta M_c \quad (e)$$

$$\Delta N = N_v \Delta v + N_p \Delta p + N_r \Delta r + \Delta N_c \quad (f)$$

(4.14)

The subscript c stands for the forces and moments sourced by the control actuations. The dimensional derivatives are expressed in X_u notation and may be given as:

$$X_u = \frac{\partial X}{\partial u} \quad (4.15)$$

In Equation (4.14), symmetric force and moment derivatives are neglected. Since X_q derivative is negligibly small [87], it is ignored. Z_w and M_w derivatives are also neglected since they do not have a powerful effect upon the aircraft's motion [81], [85]. Additionally, it is assumed that the vehicle flies at a constant altitude or the density of the is not changing. The dimensional stability derivatives are computed by using the formulas previously given in Table 3.11 and 3.12.

4.2.1 Linear Model of Multicopter

Using above mentioned linearization methods, the state space representation of the tricopter module for hover standing flight is obtained. Since the negligible cross-coupling between longitudinal and lateral dynamics, the linear model is represented in longitudinal and lateral form in body-fixed reference frame as follows.

$$\begin{bmatrix} \Delta \dot{u} \\ \Delta \dot{w} \\ \Delta \dot{q} \\ \Delta \dot{\theta} \end{bmatrix} = \begin{bmatrix} 0 & 0 & 0 & -g \\ 0 & 0 & 0 & 0 \\ 0 & 0 & 0 & 0 \\ 0 & 0 & 1 & 0 \end{bmatrix} \begin{bmatrix} \Delta u \\ \Delta w \\ \Delta q \\ \Delta \theta \end{bmatrix} + \begin{bmatrix} \frac{X_{\Omega_1^2}}{m} & \frac{X_{\Omega_2^2}}{m} & \frac{X_{\Omega_3^2}}{m} & \frac{X_{\delta}}{m} \\ \frac{Z_{\Omega_1^2}}{m} & \frac{Z_{\Omega_2^2}}{m} & \frac{Z_{\Omega_3^2}}{m} & \frac{Z_{\delta}}{m} \\ \frac{M_{\Omega_1^2}}{I_{yy}} & \frac{M_{\Omega_2^2}}{I_{yy}} & \frac{M_{\Omega_3^2}}{I_{yy}} & \frac{M_{\delta}}{I_{yy}} \\ 0 & 0 & 0 & 0 \end{bmatrix} \begin{bmatrix} \Delta \Omega_1^2 \\ \Delta \Omega_2^2 \\ \Delta \Omega_3^2 \\ \Delta \delta \end{bmatrix} \quad (4.16)$$

$$\begin{bmatrix} \Delta \dot{v} \\ \Delta \dot{p} \\ \Delta \dot{r} \\ \Delta \dot{\phi} \end{bmatrix} = \begin{bmatrix} 0 & 0 & 0 & g \\ 0 & 0 & 0 & 0 \\ 0 & 0 & 0 & 0 \\ 0 & 1 & 0 & 0 \end{bmatrix} \begin{bmatrix} \Delta v \\ \Delta p \\ \Delta r \\ \Delta \phi \end{bmatrix} + \begin{bmatrix} Y_{\Omega_1^2} / m & Y_{\Omega_2^2} / m & Y_{\Omega_3^2} / m & Y_{\delta} / m \\ I_3 L_{\Omega_1^2} + I_2 N_{\Omega_1^2} & I_3 L_{\Omega_2^2} + I_2 N_{\Omega_2^2} & I_3 L_{\Omega_3^2} + I_2 N_{\Omega_3^2} & I_3 L_{\delta} + I_2 N_{\delta} \\ I_2 L_{\Omega_1^2} + I_1 N_{\Omega_1^2} & I_2 L_{\Omega_2^2} + I_1 N_{\Omega_2^2} & I_2 L_{\Omega_3^2} + I_1 N_{\Omega_3^2} & I_2 L_{\delta} + I_1 N_{\delta} \\ 0 & 0 & 0 & 0 \end{bmatrix} \begin{bmatrix} \Delta \Omega_1^2 \\ \Delta \Omega_2^2 \\ \Delta \Omega_3^2 \\ \Delta \delta \end{bmatrix} \quad (4.17)$$

where I_1 , I_2 and I_3 are: $I_1 = \frac{I_{xx}}{(I_{xx}I_{zz} - I_{xz}^2)}$, $I_2 = \frac{I_{xz}}{(I_{xx}I_{zz} - I_{xz}^2)}$, $I_3 = \frac{I_{zz}}{(I_{xx}I_{zz} - I_{xz}^2)}$

The system and input matrices **A** and **B** are calculated as;

$$\mathbf{A}_{long} = \begin{bmatrix} 0 & 0 & 0 & -9.8066 \\ 0 & 0 & 0 & 0 \\ 0 & 0 & 0 & 0 \\ 0 & 0 & 1 & 0 \end{bmatrix}, \quad \mathbf{A}_{lat} = \begin{bmatrix} 0 & 0 & 0 & 9.8066 \\ 0 & 0 & 0 & 0 \\ 0 & 0 & 0 & 0 \\ 0 & 0 & 1 & 0 \end{bmatrix} \quad (4.18)$$

$$\mathbf{B}_{long} = \begin{bmatrix} 0 & 0 & 0 & 0.0090 \\ 0 & 0 & 0 & 0.1710 \\ 0 & 0 & 0 & -0.6092 \\ 0 & 0 & 0 & 0 \end{bmatrix}, \quad \mathbf{B}_{lat} = \begin{bmatrix} 0 & 0 & 0 & 0 \\ 0 & 0 & 0 & 1.1640 \\ 0 & 0 & 0 & -14.8345 \\ 0 & 0 & 0 & 0 \end{bmatrix} \quad (4.19)$$

The output and feedthrough matrices, **C** and **D** are specified as;

$$\mathbf{C}_{long} = \begin{bmatrix} 1 & 0 & 0 & 0 \\ 0 & 1 & 0 & 0 \\ 0 & 0 & 1 & 0 \\ 0 & 0 & 0 & 1 \end{bmatrix}, \quad \mathbf{C}_{lat} = \begin{bmatrix} 1 & 0 & 0 & 0 \\ 0 & 1 & 0 & 0 \\ 0 & 0 & 1 & 0 \\ 0 & 0 & 0 & 1 \end{bmatrix} \quad (4.20)$$

$$\mathbf{D}_{long} = \begin{bmatrix} 0 & 0 & 0 & 0 \\ 0 & 0 & 0 & 0 \\ 0 & 0 & 0 & 0 \\ 0 & 0 & 0 & 0 \end{bmatrix}, \quad \mathbf{D}_{lat} = \begin{bmatrix} 0 & 0 & 0 & 0 \\ 0 & 0 & 0 & 0 \\ 0 & 0 & 0 & 0 \\ 0 & 0 & 0 & 0 \end{bmatrix} \quad (4.21)$$

4.2.2 Linear Model of Fixed-Wing Module

Similarly, the linearized system of the fixed-wing module could be represented in state space form (in body-fixed reference frame) for longitudinal and lateral dynamics as;

$$\begin{bmatrix} \Delta \dot{u} \\ \Delta \dot{w} \\ \Delta \dot{q} \\ \Delta \dot{\theta} \end{bmatrix} = \begin{bmatrix} \frac{X_u}{m} & \frac{X_w}{m} & -w_0 & -g \cos \theta_0 \\ \frac{Z_u}{m} & \frac{Z_w}{m} & u_0 + \frac{Z_q}{m} & -g \sin \theta_0 \\ \frac{M_u}{I_{yy}} & \frac{M_w}{I_{yy}} & \frac{M_q}{I_{yy}} & 0 \\ 0 & 0 & 1 & 0 \end{bmatrix} \begin{bmatrix} \Delta u \\ \Delta w \\ \Delta q \\ \Delta \theta \end{bmatrix} + \begin{bmatrix} X_{\delta_e} / m & X_{\delta_p} / m \\ Z_{\delta_e} / m & Z_{\delta_p} / m \\ M_{\delta_e} / I_{yy} & M_{\delta_p} / I_{yy} \\ 0 & 0 \end{bmatrix} \begin{bmatrix} \Delta \delta_e \\ \Delta \delta_p \end{bmatrix} \quad (4.22)$$

$$\begin{bmatrix} \Delta \dot{v} \\ \Delta \dot{p} \\ \Delta \dot{r} \\ \Delta \dot{\phi} \end{bmatrix} = \begin{bmatrix} \frac{Y_v}{m} & w_0 + \frac{Y_p}{m} & -u_0 + \frac{Y_r}{m} & g \cos \theta_0 \\ I_3 L_v + I_2 N_v & I_3 L_p + I_2 N_p & I_3 L_r + I_2 N_r & 0 \\ I_2 L_v + I_1 N_v & I_2 L_p + I_1 N_p & I_2 L_r + I_1 N_r & 0 \\ 0 & 1 & \tan \theta_0 & 0 \end{bmatrix} \begin{bmatrix} \Delta v \\ \Delta p \\ \Delta r \\ \Delta \phi \end{bmatrix} + \begin{bmatrix} Y_{\delta_a} / m & Y_{\delta_r} / m \\ I_3 L_{\delta_a} + I_2 N_{\delta_a} & I_3 L_{\delta_r} + I_2 N_{\delta_r} \\ I_2 L_{\delta_a} + I_1 N_{\delta_a} & I_2 L_{\delta_r} + I_1 N_{\delta_r} \\ 0 & 0 \end{bmatrix} \begin{bmatrix} \Delta \delta_a \\ \Delta \delta_r \end{bmatrix} \quad (4.23)$$

For the derived linear model, the system and input matrices **A** and **B** are calculated as;

$$\mathbf{A}_{long} = \begin{bmatrix} -0.0259 & 0.2805 & 0.1277 & -9.8064 \\ -1.0774 & -6.9851 & 16.4275 & 0.0688 \\ 0 & -7.7125 & -13.6793 & 0 \\ 0 & 0 & 1 & 0 \end{bmatrix} \quad (4.24)$$

$$\mathbf{A}_{lat} = \begin{bmatrix} -0.1986 & -0.1074 & -17.9751 & 9.8064 \\ -0.2319 & -14.5843 & 3.0972 & 0 \\ 1.3587 & -1.1434 & -1.5153 & 0 \\ 0 & 1 & -0.0070 & 0 \end{bmatrix} \quad (4.25)$$

$$\mathbf{B}_{long} = \begin{bmatrix} 0 & 0.0369 \\ -0.1747 & 0 \\ -2.3597 & -0.0276 \\ 0 & 0 \end{bmatrix}, \quad \mathbf{B}_{lat} = \begin{bmatrix} 0 & 0.0391 \\ -3.7626 & -0.0037 \\ -0.0296 & -0.2680 \\ 0 & 0 \end{bmatrix} \quad (4.26)$$

The output and feedthrough matrices, \mathbf{C} and \mathbf{D} are;

$$\mathbf{C}_{long} = \begin{bmatrix} 1 & 0 & 0 & 0 \\ 0 & 1 & 0 & 0 \\ 0 & 0 & 1 & 0 \\ 0 & 0 & 0 & 1 \end{bmatrix}, \quad \mathbf{C}_{lat} = \begin{bmatrix} 1 & 0 & 0 & 0 \\ 0 & 1 & 0 & 0 \\ 0 & 0 & 1 & 0 \\ 0 & 0 & 0 & 1 \end{bmatrix} \quad (4.27)$$

$$\mathbf{D}_{long} = \begin{bmatrix} 0 & 0 \\ 0 & 0 \\ 0 & 0 \\ 0 & 0 \end{bmatrix}, \quad \mathbf{D}_{lat} = \begin{bmatrix} 0 & 0 \\ 0 & 0 \\ 0 & 0 \\ 0 & 0 \end{bmatrix} \quad (4.28)$$

4.3 Stability Analysis

4.3.1 Multicopter Module

In section 4.2.1 a linear state space model of the multicopter module has been reported in terms of real actuator inputs. In that representation, each state is coupled with all inputs and it is not possible to control a state with a specific input. Here, the transfer functions of the system are obtained with respect to the force and moments.

Table 4.4. Transfer functions of tricopter with respect to force inputs

$\frac{\Delta u}{\Delta X} = \frac{0.25}{s}$	$\frac{\Delta x_E}{\Delta X} = \frac{0.25}{s^2}$
$\frac{\Delta w}{\Delta Z} = \frac{0.25}{s}$	$\frac{\Delta z_E}{\Delta Z} = \frac{0.25}{s^2}$

Table 4.5. Transfer functions of tricopter with respect to moment inputs

$\frac{\Delta v}{\Delta L} = \frac{27.02}{s^3}$	$\frac{\Delta p}{\Delta L} = \frac{2.755}{s}$	$\frac{\Delta \phi}{\Delta L} = \frac{2.755}{s^2}$	$\frac{\Delta y_E}{\Delta L} = \frac{27.02}{s^4}$
$\frac{\Delta u}{\Delta M} = \frac{-32.47}{s^3}$	$\frac{\Delta q}{\Delta M} = \frac{3.311}{s}$	$\frac{\Delta \theta}{\Delta M} = \frac{3.311}{s^2}$	$\frac{\Delta x_E}{\Delta M} = \frac{-32.47}{s^4}$
$\frac{\Delta r}{\Delta N} = \frac{1.572}{s}$		$\frac{\Delta \psi}{\Delta N} = \frac{1.572}{s^2}$	

As can be noted from the transfer functions of the tricopter, all the poles are at the origin of the complex plane. Thus, the open loop system is unstable. It is also noted that, side-force Y cannot be produced by the tricopter module.

4.3.2 Fixed-Wing Module

The system matrices for the linearized model at the trim point are given in equations (4.24) and (4.25). There are two pairs of poles of the longitudinal system which specify the short-period and phugoid modes. The poles of the two modes lie on left hand side of the complex plane which implies the stability of the longitudinal characteristics of the vehicle. The short period mode influences the fast-transient characteristics of the longitudinal motion which is heavily damped and oscillatory for a short period of time with variation of angle of attack, pitch angle with very little change in forward velocity. The phugoid mode affects the slow-transient characteristics of longitudinal motion. It is responsible for large amplitude variation of pitch angle, forward velocity, and altitude. The parameters for longitudinal modes are given in the Table 4.6.

Table 4.6. Longitudinal characteristics of fixed-wing module of the vehicle

Name	Poles $n + j\omega$	Nat. Freq. ω_n (rad/s)	Damp. Ratio ξ	Period T (s)	Time to Double t_{double} (s)
Short Period	-10.345 $\pm j10.754$	14.922	0.693	0.584	0.067
Phugoid	-0.004 $\pm j0.605$	0.605	0.007	10.384	173.87

There are three modes governing the characteristics of lateral motion of the fixed-wing module which are called as roll, dutch-roll and spiral modes. Roll mode defines the characteristics of pure rolling motion and it is stable. Dutch-roll mode is responsible for oscillatory and coupled roll – yaw motion. This mode is also stable. The mode corresponding to pole having positive real part is spiral mode. The spiral modes of an airplane usually have high doubling time and may be unstable. The parameters for lateral modes of the vehicle are given in Table 4.7 and 4.8.

Table 4.7. Dutch-roll mode characteristics of the fixed-wing module

Name	Poles $n + j\omega$	Nat. Freq. ω_n (rad/s)	Damp. Ratio ξ	Period T (s)	Time to Double t_{double} (s)
Dutch-Roll	-1.002 $\pm j5$	5.1	0.197	1.257	0.692

Table 4.8. Roll and spiral mode characteristics of the fixed-wing module

Name	Poles $n + j\omega$	Time Constant τ (s)	Time to Double t_{double} (s)
Roll	-14.397	0.069	0.048
Spiral	0.097	-10.3	7.116

4.3.2.1 Short Period and Roll Mode Approximations

In order to design pitch and roll orientation autopilots, the transfer functions of linearized system such that having more accurate representation of characteristics should be used. Thus, short period and roll mode approximations is used to design linear controllers for pitch and roll displacement controllers [85].

Similar to multicopter transfer functions given in Table 4.4 and 4.5, the transfer functions of pitch and roll angles will be presented in terms of moments, for the purpose of similarity in control system architecture (refer to Chapter 5.3). For short period mode, it is assumed that $\Delta u = 0$ and X force equation is neglected.

$$\begin{bmatrix} \Delta \dot{w} \\ \Delta \dot{q} \\ \Delta \dot{\theta} \end{bmatrix} = \begin{bmatrix} Z_w/m & u_0 & 0 \\ M_w/I_{yy} & M_q/I_{yy} & 0 \\ 0 & 1 & 0 \end{bmatrix} \begin{bmatrix} \Delta w \\ \Delta q \\ \Delta \theta \end{bmatrix} + \begin{bmatrix} 1/m & 0 \\ 0 & 1/I_{yy} \\ 0 & 0 \end{bmatrix} \begin{bmatrix} \Delta Z \\ \Delta M \end{bmatrix} \quad (4.29)$$

$$A_{sp} = \begin{bmatrix} -6.988 & 18.2 & 0 \\ -7.715 & -13.68 & 0 \\ 0 & 1 & 0 \end{bmatrix}, B_{sp} = \begin{bmatrix} 0.25 & 0 \\ 0 & 3.311 \\ 0 & 0 \end{bmatrix}, C_{sp} = \begin{bmatrix} 1 & 0 & 0 \\ 0 & 1 & 0 \\ 0 & 0 & 1 \end{bmatrix}, D_{sp} = \begin{bmatrix} 0 & 0 \\ 0 & 0 \\ 0 & 0 \end{bmatrix} \quad (4.30)$$

The transfer function that relates the pitch angle and pitching moment is found to be:

$$\left(\frac{\Delta \theta(s)}{\Delta M(s)} \right)_{sp} = \frac{3.311s + 23.14}{s^3 + 20.67s^2 + 236s} \quad (4.31)$$

For the rolling orientation, the roll mode approximation is used. The equation of pure roll motion is obtained from the Equation (4.23) and may be given as follows by a single degree of freedom approximation.

$$\Delta \dot{p} = I_3 L_p \Delta p + I_3 \Delta L \quad (4.32)$$

The equation is rearranged after taking its Laplace transform.

$$\frac{\Delta p(s)}{\Delta L(s)} = \frac{I_3}{s - I_3 L_p} \quad (4.33)$$

Also, inserting $\Delta p(s) = s \Delta \phi(s)$, $I_3 = \frac{I_{zz}}{(I_{xx} I_{zz} - I_{xz}^2)}$ and the value of roll damping, L_p

(at the trim point) into the Equation (4.32), we get:

$$\frac{\Delta \phi(s)}{\Delta L(s)} = \frac{I_3}{s(s - I_3 L_p)} = \frac{2.755}{s^2 + 14.575s} \quad (4.34)$$

CHAPTER 5

CONTROL OF THE VEHICLE

Aircrafts are composed of expensive equipment and must be well controlled from takeoff to landing to prevent any injuries and financial losses. Although an airplane has stable dynamics especially in cruising flights and it is manually controllable, unfortunately, multirotor aerial vehicles don't have the same characteristics. It is nearly impossible to control multirotor, especially tilting multirotor vehicles manually. Thus, automatic flight controllers are needed to get the aerial vehicles done control commands, even very aggressive maneuvering commands.

In this chapter, for the nonlinear dynamics of the hybrid aerial vehicle, linear and nonlinear flight controllers are developed and implemented. Flight controllers are developed for multirotor and fixed-wing modes. Control allocation and mapping between virtual control commands and actuators, such as, motors, tilting mechanisms, and control surface deflections are provided.

5.1 Concepts of Operations

The designed hybrid vehicle will have separate controllers stabilizing the vehicle in hover and forward flight phases. During transition and back transition phases the both controllers will be active and the control signals will be mixed. Besides the stabilization, the controllers will make the vehicle to follow the given commands from the pilot (pilot in the loop). The commands will be delivered by a remote controller that has four main channels that controlled by command sticks.

In multicopter mode altitude is controlled by throttle stick which adjusts the total thrust created by upward directed tri-propellers. The attitudes roll, pitch and yaw are

controlled by corresponding control sticks by adjusting propeller angular velocities and servo tilts through the controller unit. On the other hand, at the fixed-wing mode, the throttle stick adjusts the total throttle value of the two (totally) tilted front propellers (the front propellers rotate have the same rpm values but opposite rotation direction in the fixed-wing mode). The attitude orientation is controlled by using roll, pitch and yaw channels that control the deflections of control surfaces of aileron, elevator and rudder.

Also, the remote controller has channels of switches to start forward transition from hover to forward flight or back transition from forward to hover flight. The forward transition from hover is started by switching on the transition stick. Then the front rotors start to tilt gradually (mean tilt angle) from 0 to 20 degrees in 4 seconds. Due to this tilt angle, the thrust component in body x -direction start to accelerate the vehicle. During the forward transition, the lost body z -component of the thrust will be compensated by increasing rpm values of the front rotors. In this way the altitude of the vehicle can be maintained. While the forward speed increases, the aerodynamic forces and moments become more effective. When the vehicle reaches 15 m/s of forward speed which is above the stall speed, the front rotors are tilted at once from 20 to 90 degrees and the transition is completed. The required throttle value is set to reach forward flight trim point of 18.2 m/s.

Finally, the back transition is started from forward flight trim point by activating back transition switch. Then, front rotors are tilted from 90 to 20 degrees (mean tilt angle) and then gradually tilted from 20 degrees to 0 degrees (mean tilt angle) in 4 seconds. When the forward speed decrease to 15 m/s the vehicle starts to perform a breaking pitch up maneuver to decrease forward speed to zero to pass the hover flight.

5.2 Controllability and Observability

In order to check controllability of the system, rank of the controllability matrix (which composed of state matrices \mathbf{A} and \mathbf{B}) is analyzed. The controllability matrix must have full rank for a controllable system for an n -by- n \mathbf{A} matrix [88].

$$\text{rank}\left(\left[\mathbf{B} \mid \mathbf{A}\mathbf{B} \mid \cdots \mid \mathbf{A}^n\mathbf{B}\right]\right) \quad (5.1)$$

It is computed that the controllability matrices of multicopter module and both longitudinal and lateral modes of the fixed-wing module have full rank. Thus, the systems are said to be completely controllable.

Also, to check the observability of the systems, the observability matrix (which is composed of system matrices \mathbf{A} and \mathbf{C}) is used [88] and is given for an n -by- n matrix.

$$\text{rank}\left(\left[\mathbf{C}^T \mid \mathbf{A}^T\mathbf{C}^T \mid \cdots \mid (\mathbf{A}^T)^n\mathbf{C}^T\right]\right) \quad (5.2)$$

Again, since it is computed that observability matrices of the multicopter and fixed-wing systems have full rank, they are fully observable.

5.3 Controller Design

The forces and moments, including propulsive, aerodynamic and gravitational sources that exist in the equations of motion of the hybrid vehicle are virtual inputs to the dynamical system. Basically, there are three main phases of flight control process, hover, forward and transition flight phases. In hover stage, position and attitude; roll, pitch, yaw will be controlled by using force and moments \mathbf{Z} , \mathbf{L} , \mathbf{M} and \mathbf{N} generated by propulsive subsystem. In forward flight, the vehicle position and attitude will be controlled by using the moments \mathbf{L} , \mathbf{M} , \mathbf{N} produced by aerodynamics and propulsive

subsystems. Transition phase will be a combination of the previous two cases. Linear controllers are designed to control the flight phases of the vehicle. The system block diagram is shown in Figure 5.1. The designed controllers calculate necessary virtual force and moments to get desired states. Then, required actuator movement values are calculated to produce required forces and moments. Finally, the calculated forces and moments are fed to the vehicle dynamics and the system is simulated in MATLAB/Simulink.

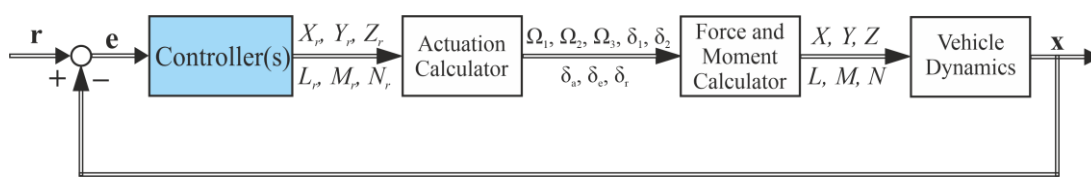


Figure 5.1. System block diagram

5.3.1 Proportional – Derivative (PD) Controller

Since attitude and altitude equations are not coupled in tricopter system, separate controllers must be designed for desired variable. Thus, four separate PD controllers are designed to control altitude and roll, pitch and yaw angles. Control signal is defined as in Equation (5.3). The block diagram of the closed loop system with implemented controller is depicted in Figure 5.2.

$$u = K_p \times e + K_d \times \frac{de}{dt} \quad (5.3)$$

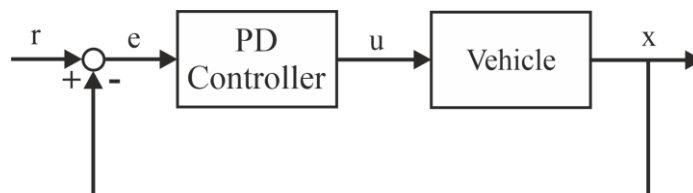


Figure 5.2. System block diagram with a PD controller for a control channel

The PD controller gain parameters are tuned individually by using Root-Locus plot to get reasonable system response in specified design requirement intervals for step response of the linearized system. The step response specifications for the multicopter controllers are selected to be;

- Maximum overshoot: $M_{p, \text{attitude}} < 15 \%$, $M_{p, \text{altitude}} < 15 \%$
- Rise time: $t_{r, \text{attitude}} < 0.5 \text{ sec}$, $t_{r, \text{altitude}} < 2 \text{ sec}$
- Settling time: $t_{s, \text{attitude}} < 1 \text{ sec}$, $t_{s, \text{altitude}} < 3 \text{ sec}$

The calculated controller gains are provided as in the following table.

Table 5.1. Tuned gain parameters for tricopter

$Kp_{\phi} = 9$	$Kp_{\theta} = 9$	$Kp_{\psi} = 11.25$	$Kp_z = 10$
$Kd_{\phi} = 4$	$Kd_{\theta} = 4$	$Kd_{\psi} = 5$	$Kd_z = 10$

Similarly, separate PD controllers are designed for the fixed-wing module to control vehicle attitude. The controller gains are tuned using Root-Locus plots in the following design requirement parameters and given in Table 5.2.

- Maximum overshoot: $M_p < 10 \%$
- Rise time: $t_r < 1 \text{ sec}$
- Settling time: $t_s < 3 \text{ sec}$

Table 5.2. Tuned gain parameters for fixed-wing aircraft

$Kp_{\phi} = 1$	$Kp_{\theta} = 15$	$Kp_{\psi} = 0.001$
$Kd_{\phi} = 0.3$	$Kd_{\theta} = 1$	$Kd_{\psi} = 0.05$

5.3.2 Linear Quadratic Regulator (LQR) Controller

LQR is a full state feedback controller. For the purpose of designing an LQR controller, linear state space model of vehicle dynamics is needed which is provided in the previous chapter. For the provided system, a \mathbf{K} matrix that will produce an optimal control signal vector given in Equation (5.4), must be found out.

$$\mathbf{u} = -\mathbf{K}\mathbf{x} \quad (5.4)$$

To find an optimal \mathbf{K} matrix, the Equation given in (5.5) is optimized [88]. Here shown, positive-definite Hermitian or real symmetric \mathbf{Q} and \mathbf{R} matrices are used to adjust the weight of error signal and energy consumption. (\mathbf{Q} may also be a positive-semidefinite matrix.)

$$J = \int_0^{\infty} (\mathbf{x}^* \mathbf{Q} \mathbf{x} + \mathbf{u}^* \mathbf{R} \mathbf{u}) dt \quad (5.5)$$

As a result, the following equation gives the optimum \mathbf{K} which is the state feedback gain matrix. It minimizes the value of the cost function.

$$\mathbf{K} = \mathbf{R}^{-1} \mathbf{B}^* \mathbf{P} \quad (5.6)$$

\mathbf{P} is also a positive-definite Hermitian or real symmetric matrix. To find the \mathbf{P} , the Equation (5.7) is needed to be solved which is called algebraic Ricatti equation.

$$\mathbf{A}^* \mathbf{P} + \mathbf{P} \mathbf{A} - \mathbf{P} \mathbf{B} \mathbf{R}^{-1} \mathbf{B}^* \mathbf{P} + \mathbf{Q} = \mathbf{0} \quad (5.7)$$

Here, \mathbf{Q} and \mathbf{R} matrices are tuned and chosen after a tuning process, for the tricopter module as:

$$\mathbf{Q} = \begin{bmatrix} 2 & 0 & 0 & 0 & 0 & 0 & 0 & 0 \\ 0 & 0.3 & 0 & 0 & 0 & 0 & 0 & 0 \\ 0 & 0 & 0.3 & 0 & 0 & 0 & 0 & 0 \\ 0 & 0 & 0 & 0.2 & 0 & 0 & 0 & 0 \\ 0 & 0 & 0 & 0 & 1 & 0 & 0 & 0 \\ 0 & 0 & 0 & 0 & 0 & 1 & 0 & 0 \\ 0 & 0 & 0 & 0 & 0 & 0 & 1.08 & 0 \\ 0 & 0 & 0 & 0 & 0 & 0 & 0 & 1 \end{bmatrix}, \quad \mathbf{R} = \begin{bmatrix} 1 & 0 & 0 & 0 & 0 & 0 \\ 0 & 1 & 0 & 0 & 0 & 0 \\ 0 & 0 & 1 & 0 & 0 & 0 \\ 0 & 0 & 0 & 1 & 0 & 0 \\ 0 & 0 & 0 & 0 & 1 & 0 \\ 0 & 0 & 0 & 0 & 0 & 1 \end{bmatrix} \quad (5.8)$$

Following, the gain matrix \mathbf{K} is calculated as:

$$\mathbf{K} = \begin{bmatrix} 0 & 0 & 0 & 0 & 0 & 0 & 0 & 0 \\ 0 & 0 & 0 & 0 & 0 & 0 & 0 & 0 \\ 3.1623 & 0 & 0 & 0 & 0 & 0 & 0 & 1 \\ 0 & 1.0131 & 0 & 0 & 1 & 0 & 0 & 0 \\ 0 & 0 & 0.9510 & 0 & 0 & 1 & 0 & 0 \\ 0 & 0 & 0 & 1.2335 & 0 & 0 & 1.0392 & 0 \end{bmatrix} \quad (5.9)$$

Signal – block diagram with LQR controller is shown in Figure 5.3. The output vector is feedbacked after multiplying with gain matrix \mathbf{K} . If no reference input is commanded, the system will attempt to preserve the trim condition of the system. The controlled states are attitude and altitude for multicopter module.

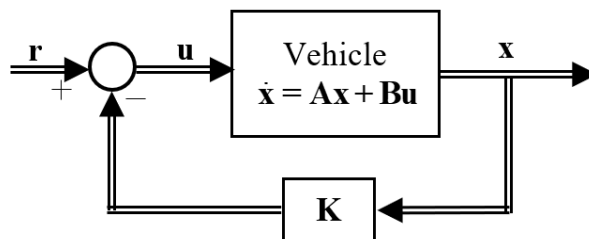


Figure 5.3. System diagram with LQR controller

5.3.3 Linear Quadratic Tracker (LQT) Controller

LQT is also a state feedback controller similar to LQR. But in cost function error signal is used as given in Equation (5.10).

$$J = \int_0^{\infty} (\mathbf{e}^* \mathbf{Q} \mathbf{e} + \mathbf{u}^* \mathbf{R} \mathbf{u}) dt \quad (5.10)$$

The error between reference input and commanded states may be written as:

$$\mathbf{e} = \mathbf{r} - \mathbf{C} \mathbf{x} \quad (5.11)$$

where matrix \mathbf{C} is selected such that to control selected states. \mathbf{Q} and \mathbf{R} matrices are the same weighting matrices in LQR part. But in tracker controller, there is a slight difference in algebraic Ricatti equation, which may be written as:

$$\mathbf{A}^* \mathbf{P} + \mathbf{P} \mathbf{A} - \mathbf{P} \mathbf{B} \mathbf{R}^{-1} \mathbf{B}^* \mathbf{P} + \mathbf{C}^* \mathbf{Q} \mathbf{C} = \mathbf{0} \quad (5.12)$$

The optimal control input is written as:

$$\mathbf{u} = -\mathbf{K}_{LQT} \mathbf{x} + \mathbf{K}_r \mathbf{r} \quad (5.13)$$

where \mathbf{K}_{LQT} and \mathbf{K}_r gain matrices is given as:

$$\mathbf{K}_{LQT} = \mathbf{R}^{-1} \mathbf{B}^* \mathbf{P} \quad (5.14)$$

and

$$\mathbf{K}_r = \mathbf{R}^{-1} \mathbf{B}^* (\mathbf{P} \mathbf{B} \mathbf{R}^{-1} \mathbf{B}^* - \mathbf{A}^*)^{-1} \mathbf{C}^* \mathbf{Q} \quad (5.15)$$

Signal – block diagram for LQT controller is given as in Figure 5.4 and the states are attitude and altitude for the multicopter module.

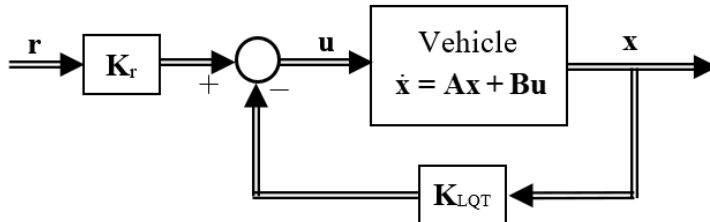


Figure 5.4. System Diagram with LQT

Q and **R** weighting matrices are tuned and determined as follows for the tricopter.

$$\mathbf{Q}_{LQT} = \begin{bmatrix} 1 & 0 & 0 & 0 \\ 0 & 1 & 0 & 0 \\ 0 & 0 & 1 & 0 \\ 0 & 0 & 0 & 3 \end{bmatrix}, \quad \mathbf{R}_{LQT} = \begin{bmatrix} 1 & 0 & 0 & 0 & 0 & 0 \\ 0 & 1 & 0 & 0 & 0 & 0 \\ 0 & 0 & 1 & 0 & 0 & 0 \\ 0 & 0 & 0 & 1 & 0 & 0 \\ 0 & 0 & 0 & 0 & 1 & 0 \\ 0 & 0 & 0 & 0 & 0 & 1 \end{bmatrix} \quad (5.16)$$

Finally, the gain matrices are calculated as:

$$\mathbf{K}_{LQT} = \begin{bmatrix} 0 & 0 & 0 & 0 & 0 & 0 & 0 & 0 \\ 0 & 0 & 0 & 0 & 0 & 0 & 0 & 0 \\ 2.8284 & 0 & 0 & 0 & 0 & 0 & 0 & 1 \\ 0 & 0.8523 & 0 & 0 & 1 & 0 & 0 & 0 \\ 0 & 0 & 0.7775 & 0 & 0 & 1 & 0 & 0 \\ 0 & 0 & 0 & 1.4841 & 0 & 0 & 1.7321 & 0 \end{bmatrix} \quad (5.17)$$

$$\mathbf{K}_r = \begin{bmatrix} 0 & 0 & 0 & 0 \\ 0 & 0 & 0 & 0 \\ 1 & 0 & 0 & 0 \\ 0 & 1 & 0 & 0 \\ 0 & 0 & 1 & 0 \\ 0 & 0 & 0 & 1.7321 \end{bmatrix} \quad (5.18)$$

5.4 Actuation Calculation

Flight controllers implemented to the system basically delivers virtual force and moment commands. However, these virtual commands must be transformed into actuator components such as motors, tilting servos and etc. to produce the real force and moment responses. There are 8 actuator components in the designed aerial vehicle and may be shown as:

$$[\Omega_1 \ \Omega_2 \ \Omega_3 \ \delta_t \ \delta]^T, \quad [\delta_a \ \delta_e \ \delta_r]^T \quad (5.19)$$

where the first three terms are motor rpms, fourth and fifth terms are mean tilt angle and differential tilt angle and the last three terms are aileron, elevator and rudder control surface tilt angles, respectively. (Refer to Equations 3.39 and 3.40)

Force and moment equations of tricopter and fixed-wing modules are derived in Chapter 3 and they may be rearranged and given as follows. The propulsive forces and moments are,

$$\begin{bmatrix} Z_p \\ L_p \\ M_p \\ N_p \end{bmatrix} = \begin{bmatrix} 0 & -k_f & 0 & -k_f & -k_f \\ -k_t & l_s k_f & k_t & -l_s k_f & 0 \\ -h_1 k_f & l_f k_f & -h_2 k_f & l_f k_f & -l_r k_f \\ l_s k_f & k_t & -l_s k_f & -k_t & k_t \end{bmatrix} \begin{bmatrix} \Omega_1^2 \sin(\delta_t - \delta) \\ \Omega_1^2 \cos(\delta_t - \delta) \\ \Omega_2^2 \sin(\delta_t + \delta) \\ \Omega_2^2 \cos(\delta_t + \delta) \\ \Omega_3^2 \end{bmatrix} \quad (5.20)$$

$$\begin{bmatrix} \Omega_1^2 \sin(\delta_t - \delta) \\ \Omega_1^2 \cos(\delta_t - \delta) \\ \Omega_2^2 \sin(\delta_t + \delta) \\ \Omega_2^2 \cos(\delta_t + \delta) \\ \Omega_3^2 \end{bmatrix} = \begin{bmatrix} 0 & -k_f & 0 & -k_f & -k_f \\ -k_t & l_s k_f & k_t & -l_s k_f & 0 \\ -h_1 k_f & l_f k_f & -h_2 k_f & l_f k_f & -l_r k_f \\ l_s k_f & k_t & -l_s k_f & -k_t & k_t \end{bmatrix}^{-1} \begin{bmatrix} Z_p \\ L_p \\ M_p \\ N_p \end{bmatrix} \quad (5.21)$$

Here, the motor rpms and differential tilt angle are calculated for a known δ_t angle.

The aerodynamic forces and moments may be written as:

$$\begin{bmatrix} X_A \\ Y_A \\ Z_A \\ L_A \\ M_A \\ N_A \end{bmatrix} = \frac{1}{2} \rho V^2 S \begin{bmatrix} C_X \\ C_Y \\ C_Z \\ C_L \\ C_M \\ C_N \end{bmatrix} = \frac{1}{2} \rho V^2 S \left(\begin{bmatrix} C_X \\ C_Y \\ C_Z \\ C_L \\ C_M \\ C_N \end{bmatrix}_{(\alpha, \beta)} + \Delta \begin{bmatrix} C_X \\ C_Y \\ C_Z \\ C_L \\ C_M \\ C_N \end{bmatrix} \right) \quad (5.22)$$

$$\Delta \begin{bmatrix} X_A \\ Y_A \\ Z_A \\ L_A \\ M_A \\ N_A \end{bmatrix} = \frac{1}{2} \rho V^2 S \begin{bmatrix} C_X \\ C_Y \\ C_Z \\ C_L \\ C_M \\ C_N \end{bmatrix}_{(\delta a, \delta e, \delta r)} \quad (5.23)$$

$$\Delta \begin{bmatrix} X_A \\ Y_A \\ Z_A \\ L_A \\ M_A \\ N_A \end{bmatrix} = \frac{1}{2} \rho V^2 S \begin{bmatrix} C_{X_{\delta a}} & C_{X_{\delta e}} & C_{X_{\delta r}} \\ C_{Y_{\delta a}} & C_{Y_{\delta e}} & C_{Y_{\delta r}} \\ C_{Z_{\delta a}} & C_{Z_{\delta e}} & C_{Z_{\delta r}} \\ C_{L_{\delta a}} & C_{L_{\delta e}} & C_{L_{\delta r}} \\ C_{m_{\delta a}} & C_{m_{\delta e}} & C_{m_{\delta r}} \\ C_{n_{\delta a}} & C_{n_{\delta e}} & C_{n_{\delta r}} \end{bmatrix} \begin{bmatrix} \delta a \\ \delta e \\ \delta r \end{bmatrix} \quad (5.24)$$

But, since the throttle controlled manually in fixed-wing mode, only moments are considered.

$$\begin{bmatrix} \delta a \\ \delta e \\ \delta r \end{bmatrix} = \begin{bmatrix} C_{l_{\delta a}} & C_{l_{\delta e}} & C_{l_{\delta r}} \\ C_{m_{\delta a}} & C_{m_{\delta e}} & C_{m_{\delta r}} \\ C_{n_{\delta a}} & C_{n_{\delta e}} & C_{n_{\delta r}} \end{bmatrix}^{-1} \Delta \begin{bmatrix} L_A \\ M_A \\ N_A \end{bmatrix} / \frac{1}{2} \rho V^2 S \quad (5.25)$$

$$\begin{bmatrix} \delta a \\ \delta e \\ \delta r \end{bmatrix} = \begin{bmatrix} C_{l_{\delta a}} & C_{l_{\delta e}} & C_{l_{\delta r}} \\ C_{m_{\delta a}} & C_{m_{\delta e}} & C_{m_{\delta r}} \\ C_{n_{\delta a}} & C_{n_{\delta e}} & C_{n_{\delta r}} \end{bmatrix}^{-1} \Delta \begin{bmatrix} C_L \\ C_M \\ C_N \end{bmatrix} = \begin{bmatrix} C_{l_{\delta a}} & C_{l_{\delta e}} & C_{l_{\delta r}} \\ C_{m_{\delta a}} & C_{m_{\delta e}} & C_{m_{\delta r}} \\ C_{n_{\delta a}} & C_{n_{\delta e}} & C_{n_{\delta r}} \end{bmatrix}^{-1} \left(\begin{bmatrix} C_L \\ C_M \\ C_N \end{bmatrix} - \begin{bmatrix} C_L \\ C_M \\ C_N \end{bmatrix}_{(\alpha, \beta)} \right) \quad (5.26)$$

5.4.1 Control Mixing

Normally, the hybrid vehicle is controlled only by a multicopter controller which has control on rotor rpms and rotor tilt angles in hover flight. Similarly, it is controlled only by a controller for fixed-wing module in cruising flight which has control on

aerodynamic control surface deflections. However, during transition phase both controllers are active and controls are distributed between the two. For low speed range, the multicopter controller is dominant and for high speed range, the controller of fixed-wing module is dominant. The weight of the signals that output from the two controllers are specified by the controller effectiveness factor which is a function of mean tilt angle. The factor is normalized by the amount of maximum tilt angle. It may be given as:

$$\varepsilon = \frac{\delta_t}{90} \quad (5.27)$$

The controller signals of the fixed-wing module are multiplied by ε and multicopter controller signals are multiplied by $(1 - \varepsilon)$ which is shown in Figure 5.5. For example, in forward flight in which the mean tilt angle is 90° , ε will be 1 and multicopter controller will have no effect on controls. The throttle (of the two front rotors running at same rpm value in forward flight) will be controlled manually.

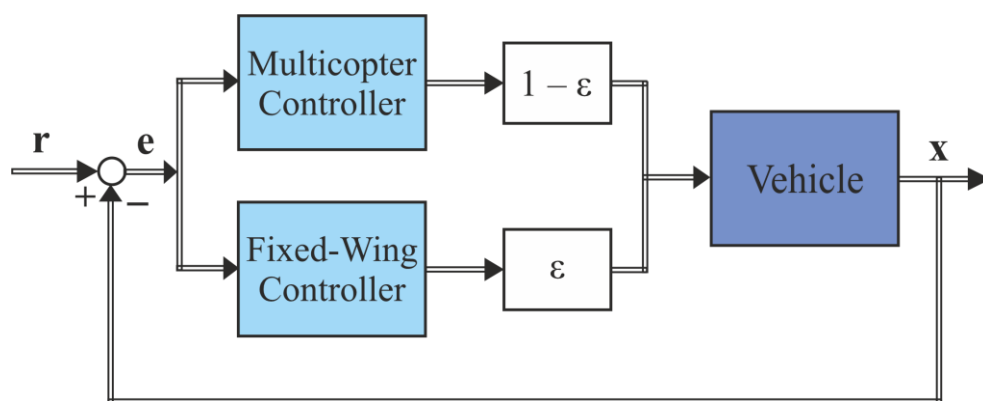


Figure 5.5. Control mixing by using control effectiveness factor

5.5 Gain Scheduling

The previously reported controller gains are obtained for trim conditions in hover and forward flights. Since they are linear controllers they are effective around the operating points that they are designed. However, at deviations from trim conditions such as transitioning, the controller gain will not be optimal. Thus, in order to have a smooth transition between flight phases, gain scheduling will be implemented.

As specified in Tables 5.1 and 5.2 in Chapter 5.3.1, the given gains will be used for hover and forward flight phases. However, for transitioning flight, the gains will be scheduled with respect to the mean tilt angle. The transitioning flight is supposed to be separated to three parts. First, tilt angle is between 0 and 10 degrees. Second, tilt angle is between 10 and 20 degrees. And third is for tilt angles between 20 and 90 degrees. The PD controller gains corresponding to these intervals are reported in the following tables.

Table 5.3. Controller gains of multicopter module for $0 < \delta_t < 10$

$Kp_\phi = 9$	$Kp_\theta = 15$	$Kp_\psi = 33.75$	$Kp_z = 10$
$Kd_\phi = 4$	$Kd_\theta = 4$	$Kd_\psi = 15$	$Kd_z = 10$

Table 5.4. Controller gains of fixed-wing module for $0 < \delta_t < 10$

$Kp_\phi = 2$	$Kp_\theta = 15$	$Kp_\psi = 1$
$Kd_\phi = 0.3$	$Kd_\theta = 1$	$Kd_\psi = 0.1$

Table 5.5. Controller gains of multicopter module for $10 < \delta_t < 20$

$Kp_\phi = 15$	$Kp_\theta = 15$	$Kp_\psi = 45$	$Kp_z = 10$
$Kd_\phi = 4$	$Kd_\theta = 4$	$Kd_\psi = 20$	$Kd_z = 10$

Table 5.6. Controller gains of fixed-wing module for $10 < \delta_t < 20$

$Kp_\phi = 2$	$Kp_\theta = 15$	$Kp_\psi = 2$
$Kd_\phi = 0.3$	$Kd_\theta = 1$	$Kd_\psi = 0.1$

5.6 Simulation Results

The designed and modeled hybrid vehicle is simulated with the developed controllers. MATLAB/Simulink is used for simulation and analysis. First, nonlinear vehicle dynamics are built in the software as an open loop system. Then, developed controllers are implemented and to distribute the control commands over vehicle actuator elements, control mixer is applied. The vehicle states are feedbacked over reference commands and the closed loop system is completed. The responses of vehicle are observed for reference commands such as roll, pitch, yaw and ascend etc.

As a first stage, multirotor and fixed-wing modes are simulated individually. After the single mode simulations, the transitioning simulations between different flight modes will be performed. The simulation results are provided in this section. The simulation flow diagram is shown as given in Figure 5.6.

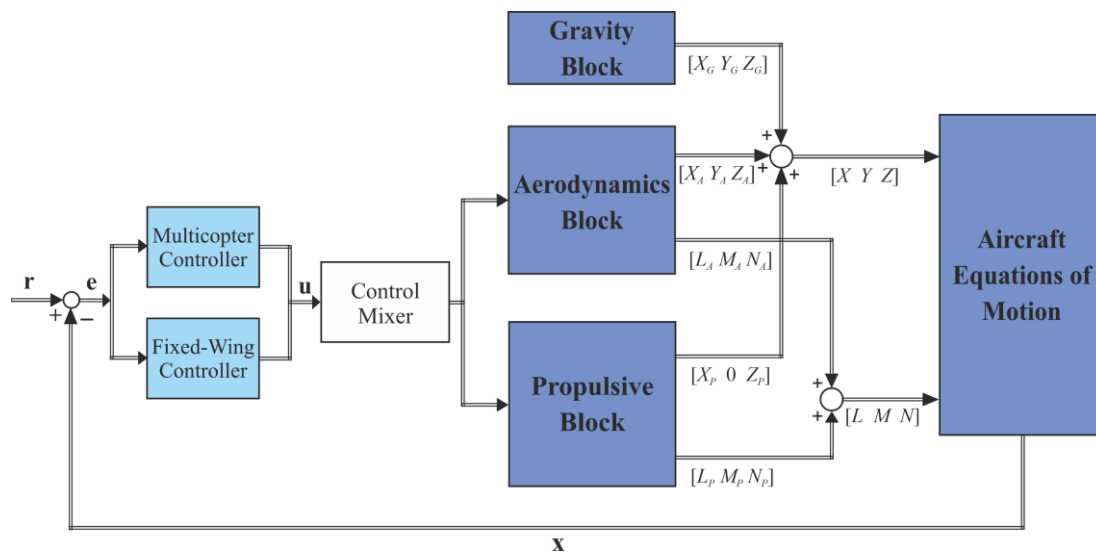


Figure 5.6. Simulation block diagram

5.6.1 Multicopter Flight Simulations

In this part, the vehicle is simulated while it is suspended in the air and keeping its altitude at a height and it is in a trimmed flight. In trimmed hover flight the vehicle has no translational and rotational velocity, and the Euler angles are at zero degrees.

In the following figures, the simulations of roll, pitch, yaw and altitude response characteristics of the aerial vehicle to the reference commands are illustrated. The actuator responses, motor rpms and tilt angles of the front two rotors are also given. The results include the simulations with designed PD, LQR and LQT controllers.

In Figure 5.7. and 5.8. the response of the hybrid vehicle to the roll reference command in multicopter mode is shown. The command is to roll the vehicle of 10 degrees for 5 seconds without changing the pitch, yaw attitude and the altitude. While the vehicle follows the roll command nicely, it maintains other reference attitude and altitude commands as it seen in the figure. In Figure 5.8, the roll response of the rotor rpms and tilt angles are shown. As it is expected, although there is a slight increase in rpm value of the third rear rotor, the front rotor rpms inversely and largely change to produce required rolling moment. Also, there is a slight increase (symmetric) in individual rotor tilt values to compensate the torque produced by the increase in the rpm of the third rotor. It is also noted that the mean tilt angle is kept zero.

Similarly, in Figures 5.9 and 5.10 the vehicle follows 10 degrees of pitch angle command. In order to achieve that the front two rotor and the rear rotor rpms increase and decrease inversely. Again, the individual tilt angles change inversely keeping the mean tilt angle at zero degree. In Figures 5.11 and 5.12 the yaw angle command response and in Figures 5.13 and 5.14 the altitude command response of the vehicle are observed. In order to generate a yawing moment, mainly differential tilt of front rotors is performed (thus, differential thrust about the body z -axis). Finally, for altitude control is performed by adjusting the total thrust value of the three rotors together without changing the individual tilt angles.

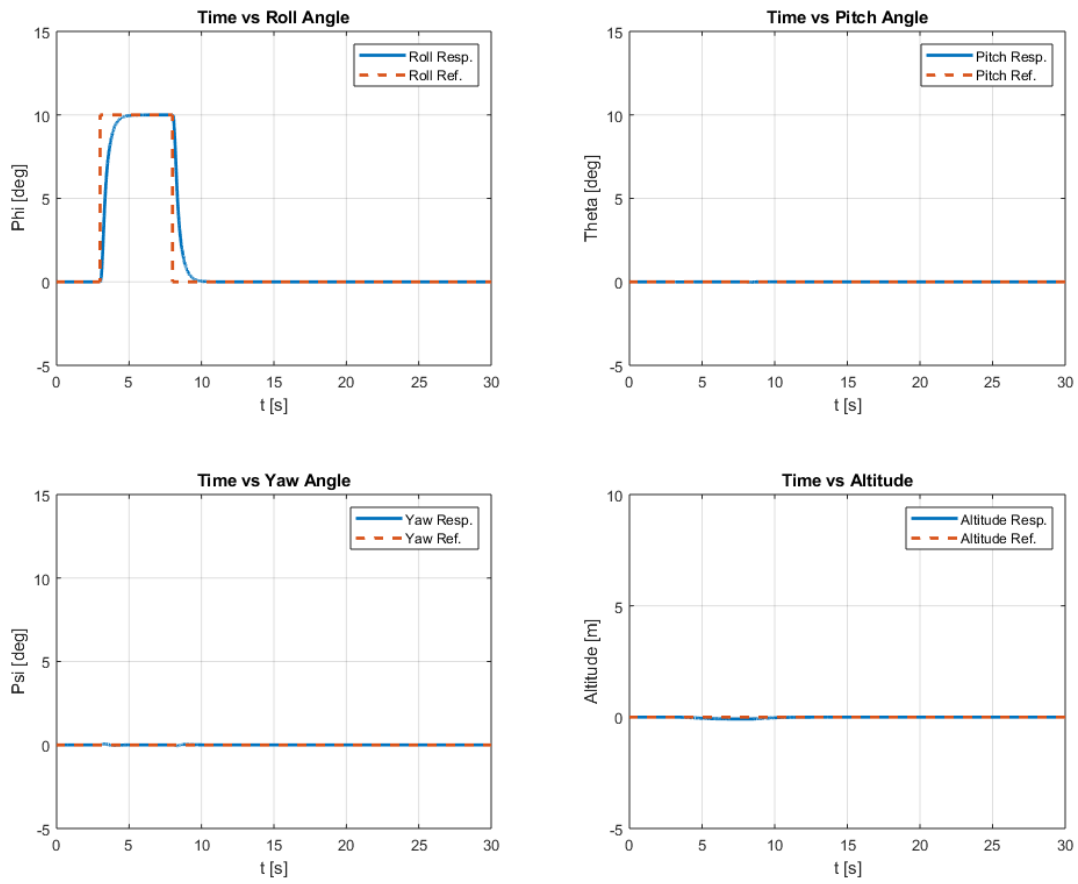


Figure 5.7. Roll reference response with PD controller

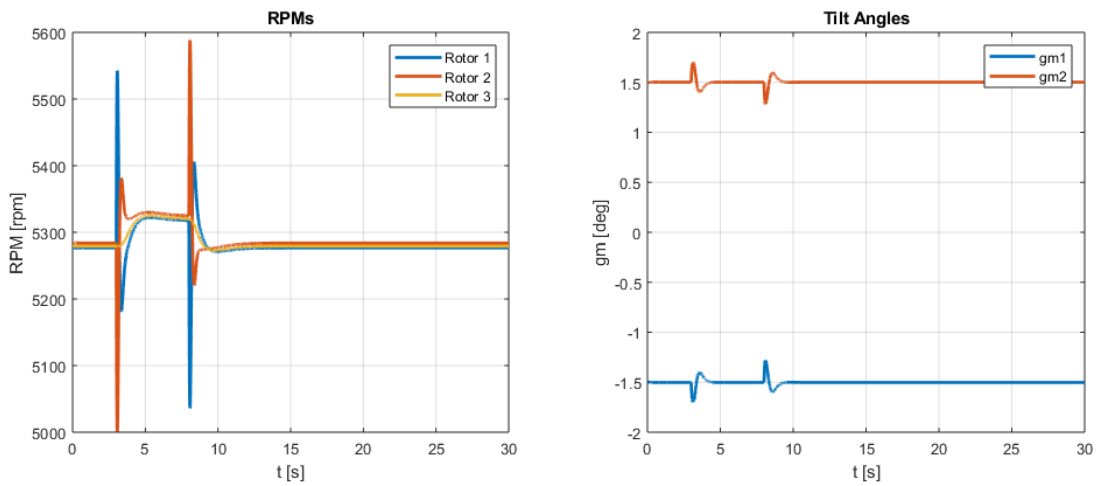


Figure 5.8. Rotor rpms and tilt angles in roll response with PD controller

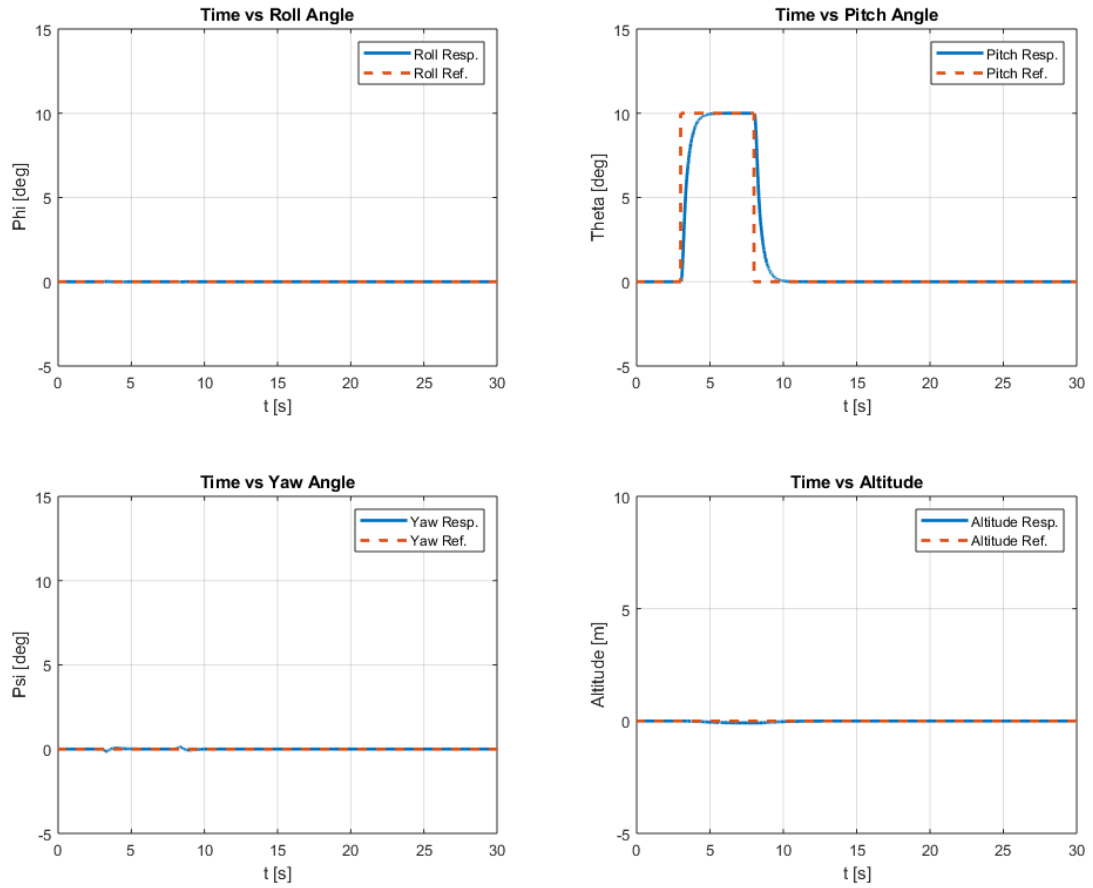


Figure 5.9. Pitch reference response with PD controller

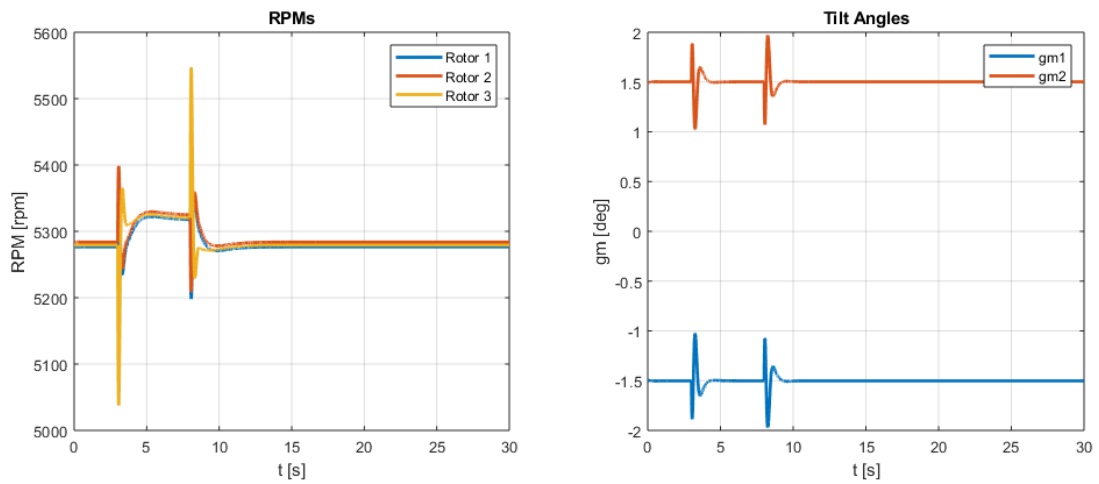


Figure 5.10. Rotor rpms and tilt angles in pitch response with PD controller

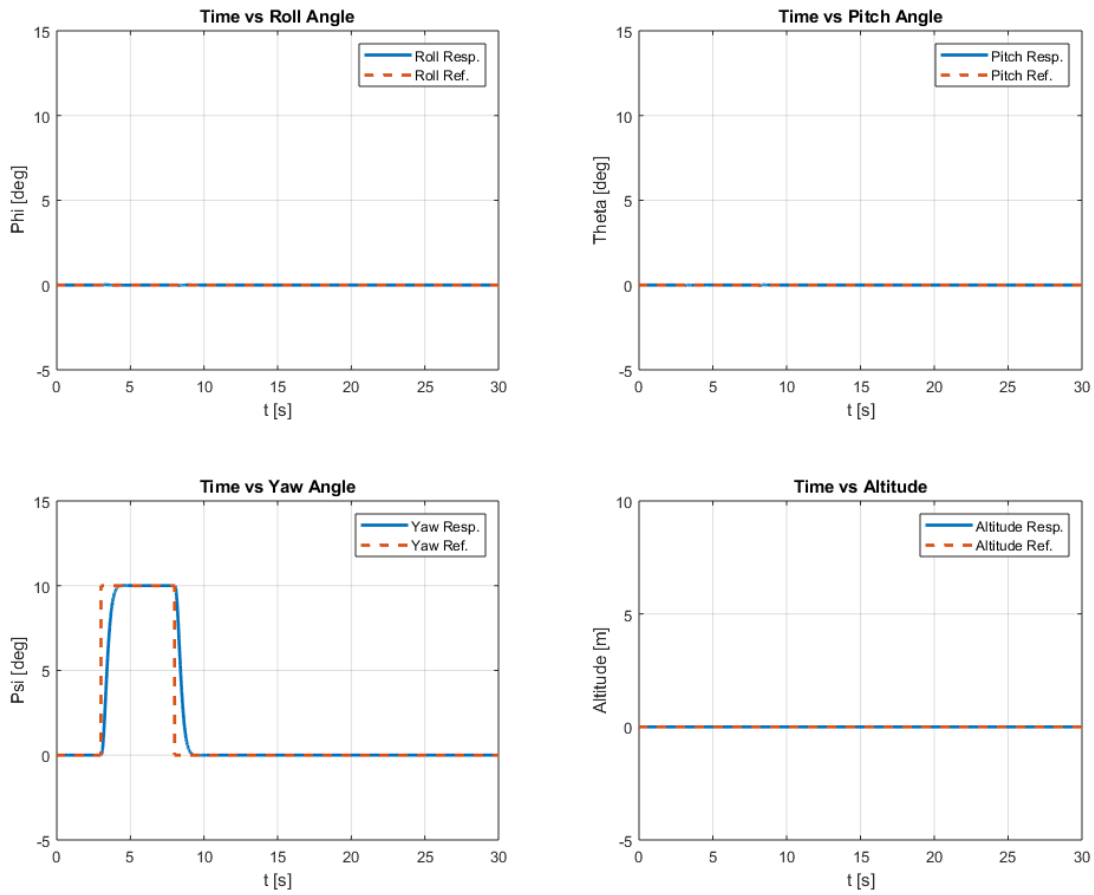


Figure 5.11. Yaw reference response with PD controller

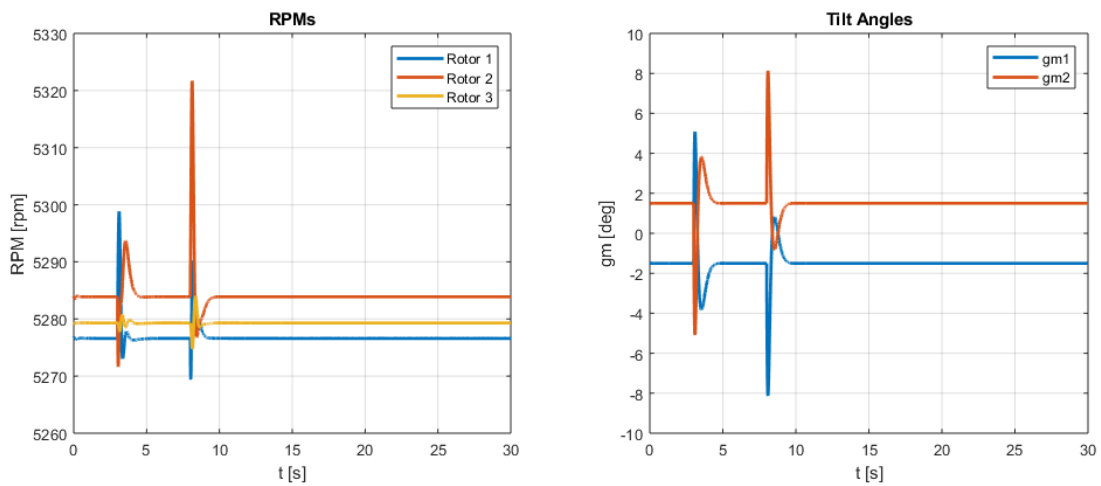


Figure 5.12. Rotor rpms and tilt angles in yaw response with PD controller

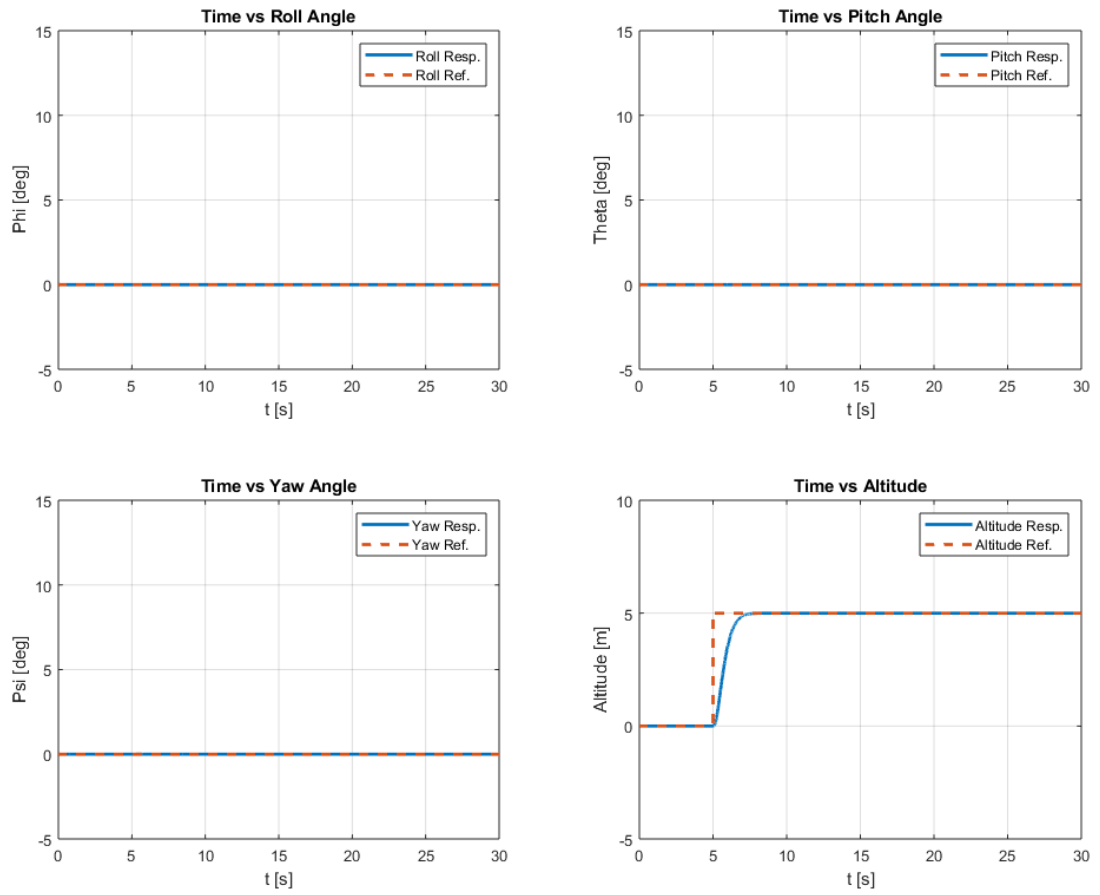


Figure 5.13. Altitude reference response with PD controller

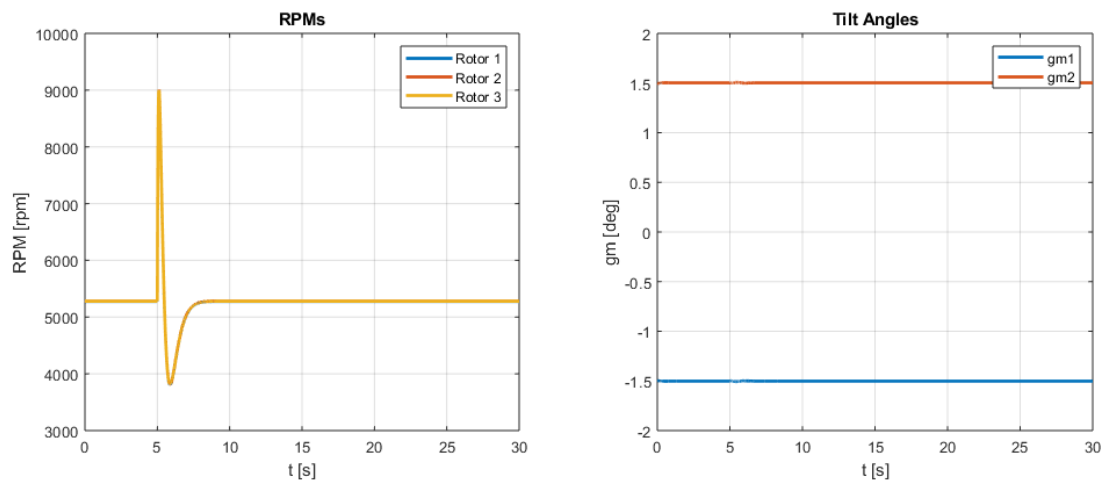


Figure 5.14. Rotor rpms and tilt angles in altitude response with PD controller

In Figures 5.15 – 5.18 the performance of the designed PD, LQR and LQT controllers are compared and shown. The designed PD controllers have better transient characteristics compared to the others. Also, LQT controller has better transient characteristics but with a slight overshoot, compared to LQR controller.

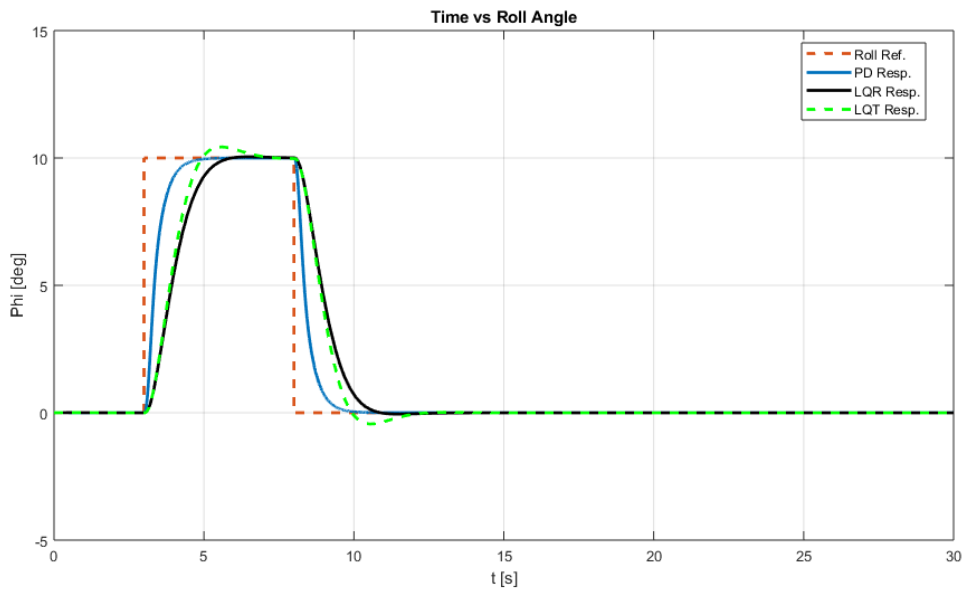


Figure 5.15. Roll reference response comparison for PD, LQR and LQT controllers

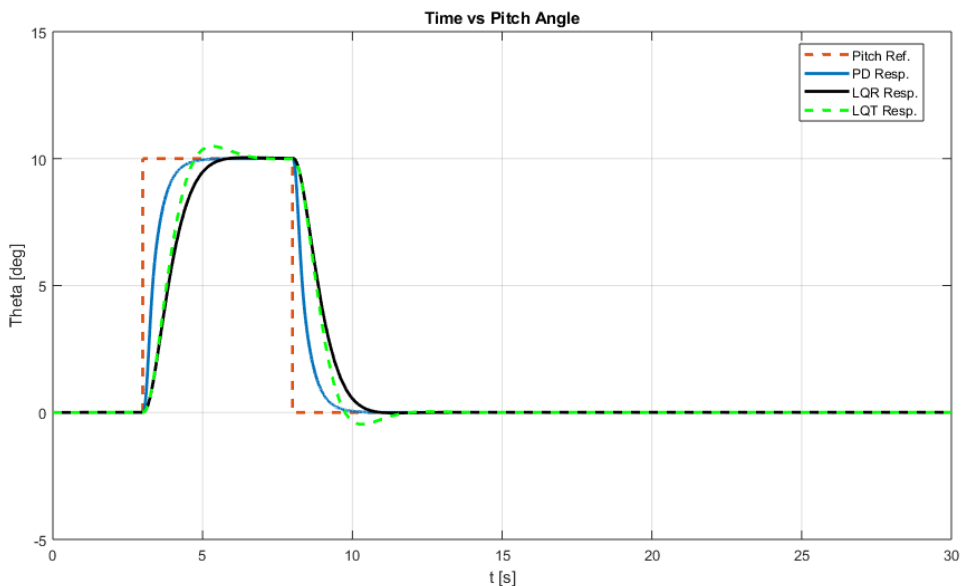


Figure 5.16. Pitch reference response comparison for PD, LQR and LQT controllers

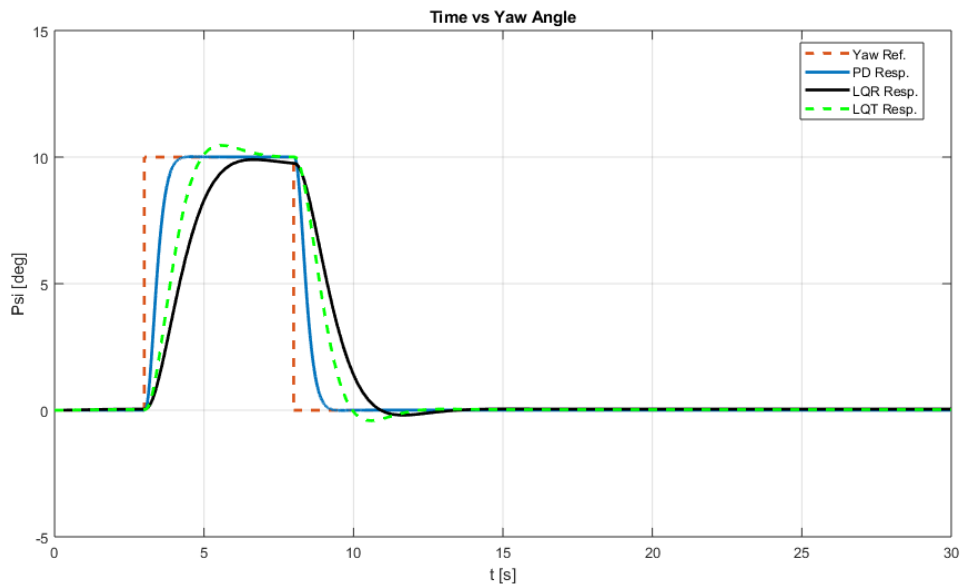


Figure 5.17. Yaw reference response comparison for PD, LQR and LQT controllers

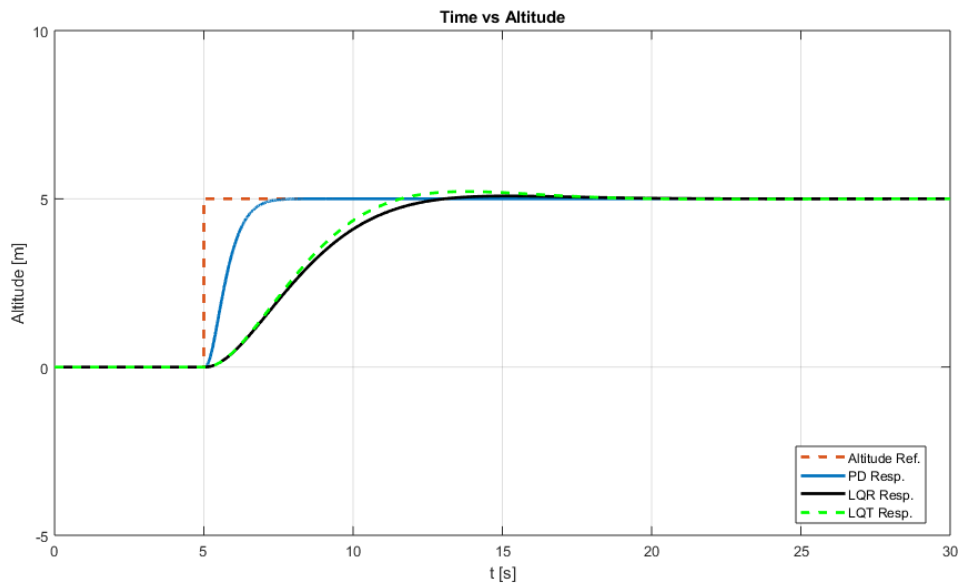


Figure 5.18. Altitude ref. response comparison for PD, LQR and LQT controllers

Although the PD controllers give better transient response they make the system to use more control inputs. The PD controllers are a good option to use during transition phases. Because they will supply more robust control during transition which may cause descensions in attitude and altitude of the vehicle.

5.6.2 Fixed-Wing Flight Simulations

In this part, the vehicle is simulated while it is cruising at a height and it is in a trimmed flight. In trimmed forward flight the vehicle has no rotational velocity, the roll angle is zero, the heading (yaw angle) is at constant value (zero degree in this case). In the following figures, simulations for the characteristics of roll pitch and yaw response of the aerial vehicle is illustrated. Results include the simulations with developed PD controllers.

In Figure 5.19 and 5.20, attitude and altitude of the vehicle is shown while it is gliding (starting from the trim point) without applying throttle. While it maintains its attitude (roll reference is at zero and the pitch reference is at trim value of -0.4 degrees), due

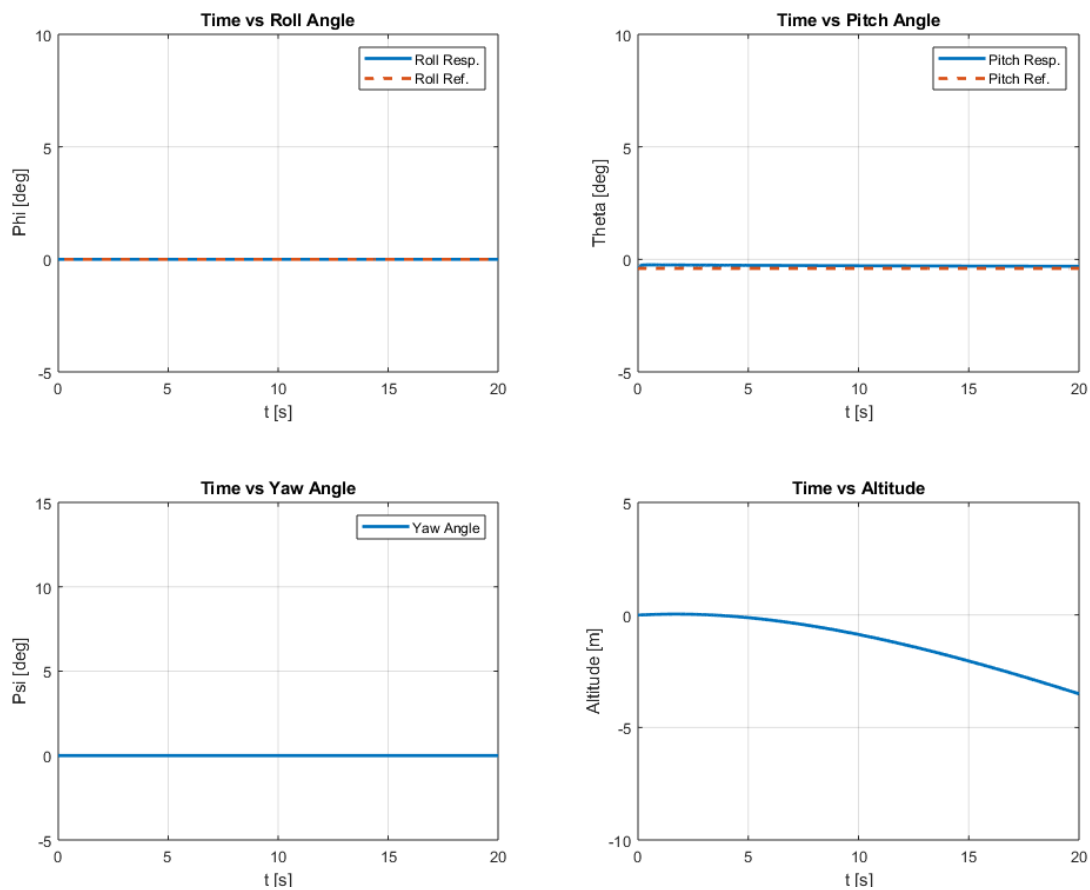


Figure 5.19. Forward flight simulation with no propulsion with PD controllers

to the drag the vehicle starts to lose its forward speed and thus due to the decrease in dynamic pressure, the generated lift force decreases. This circumstance ends up with loss in altitude as it seen. Due to altitude loss, the body z -component of velocity (w) and hence the angle of attack increases. Since no sideslip exists, the sideslip angle is at zero degree. Upon the instantaneous aerodynamic angles, airspeed and attitude command, the control surfaces deflect suitably (positive elevator and no aileron and rudder deflection in the case of Figure 5.19 and 5.20). Variation of inertial velocities and the airspeed are present in the figure.

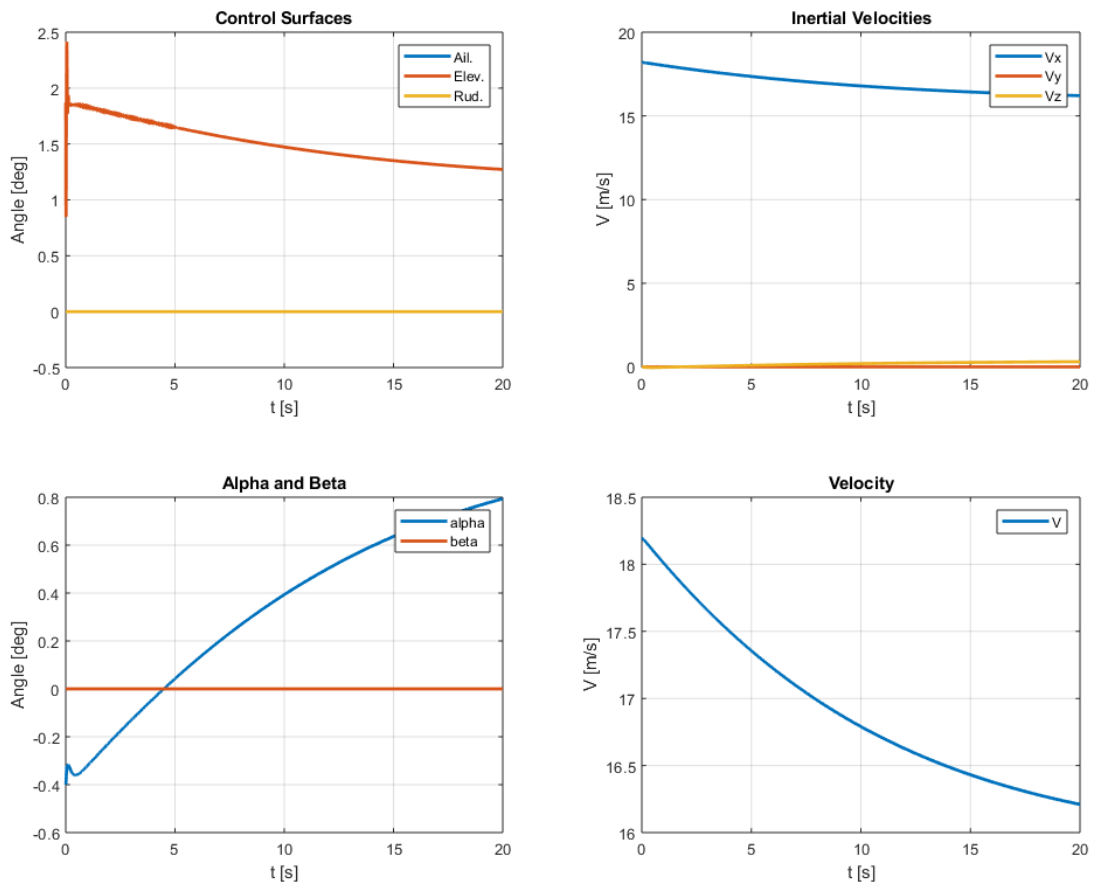


Figure 5.20. Forward flight simulation with no propulsion with PD controllers

In Figure 5.21 and 5.22 the simulation results with the designed PD controllers for the roll angle reference command are presented. The reference for pitch angle is at the trim value of -0.4 degree. With the square reference of the roll, the vehicle rolls 5 degrees and due to the bank angle the heading (yaw angle) of the vehicle starts to increase which can be observed in the figure. Again, similar to the previous case the altitude loss is observed mainly due to the drag force.

Similarly angle of attack is increased due to altitude loss and sideslip angle is generated due to banked turn which are presented in Figure 5.22. Also, the control surface actuations for the given reference commands are presented in the figure.

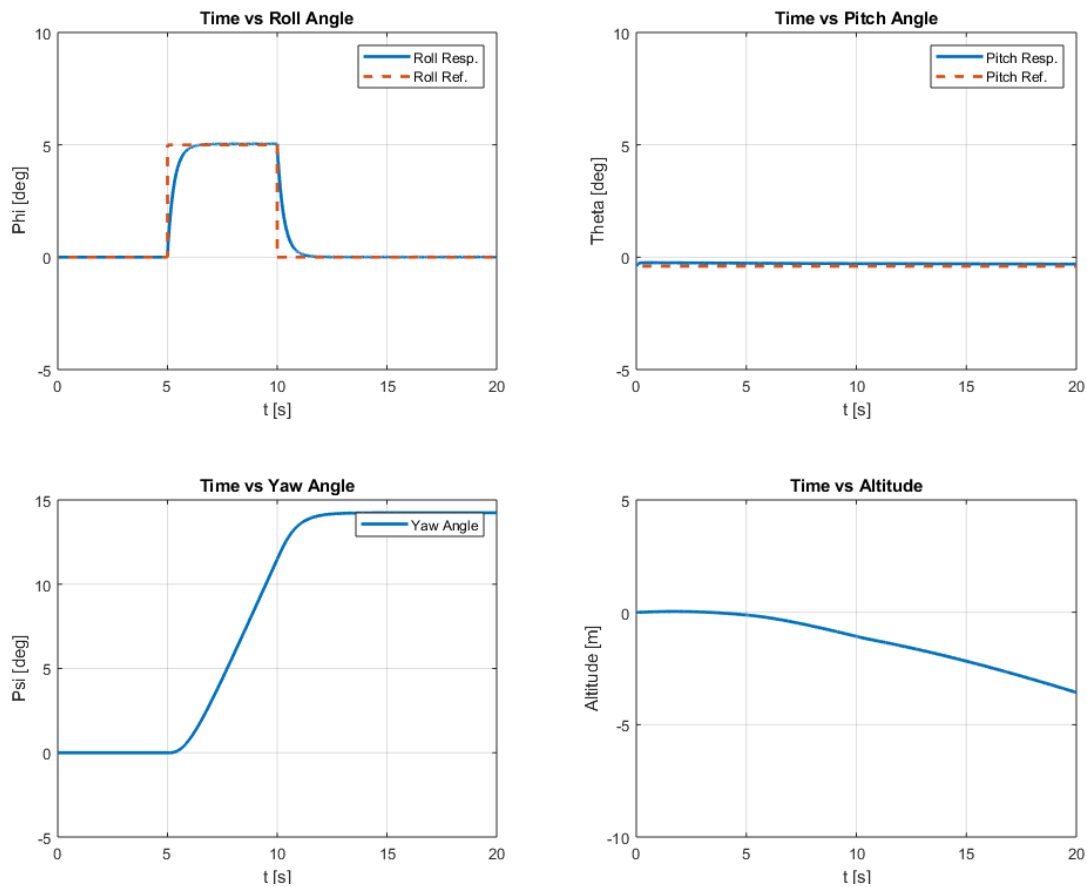


Figure 5.21. Roll response with no propulsion with PD controllers

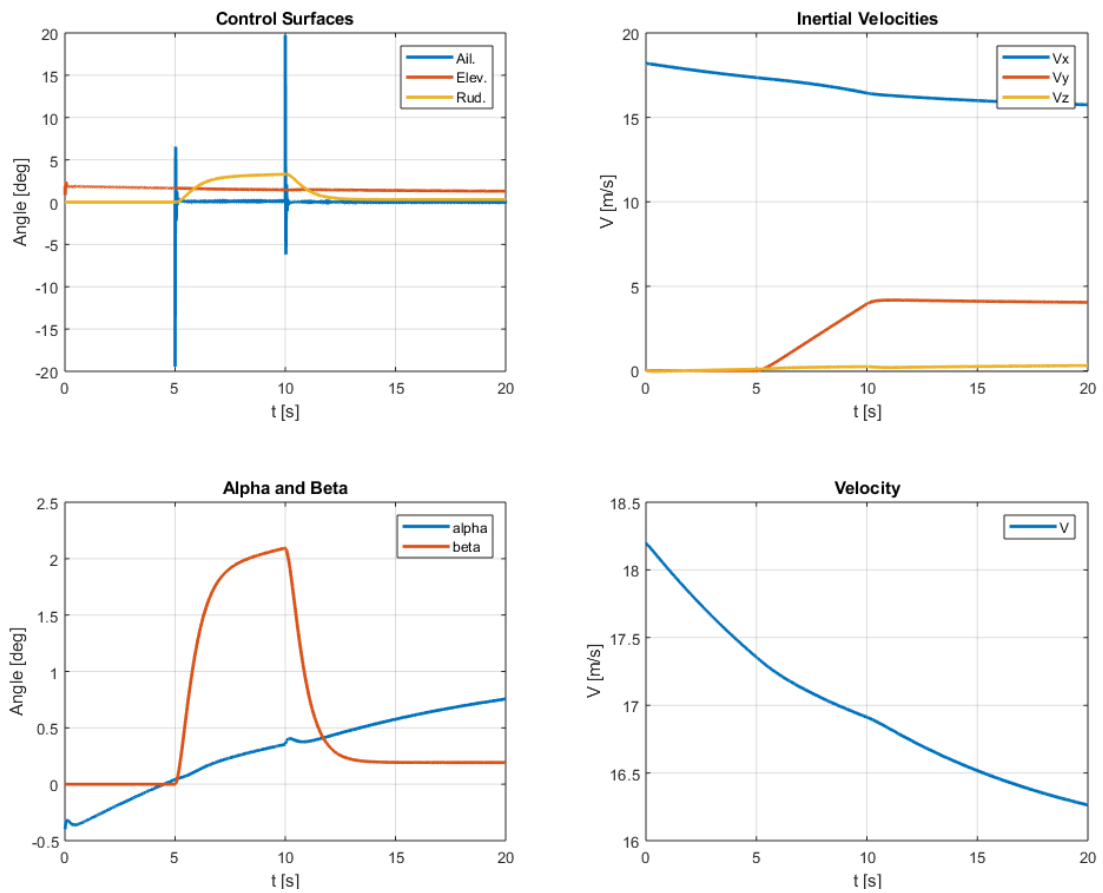


Figure 5.22. Roll response with no propulsion with PD controllers

In Figure 5.23 and 5.24 the simulation results with the designed PD controllers for the pitch angle reference command are presented. The reference for pitch angle is zero before and after 5 degrees of square wave. The roll angle and thus heading are maintained at zero. Due to increase in pitch angle the angle of attack is increased. Also, it is observed that the vehicle starts to ascend and gain altitude. However, since there is no propulsion the drag force is increased due to high angle of attack. Thus and also due to the increase in potential energy the airspeed is largely decreased. After pitching down the attitude, it is gliding and regaining airspeed as it may be observed in the following figures. Also the control surface actuations to perform desired pitch reference are presented.

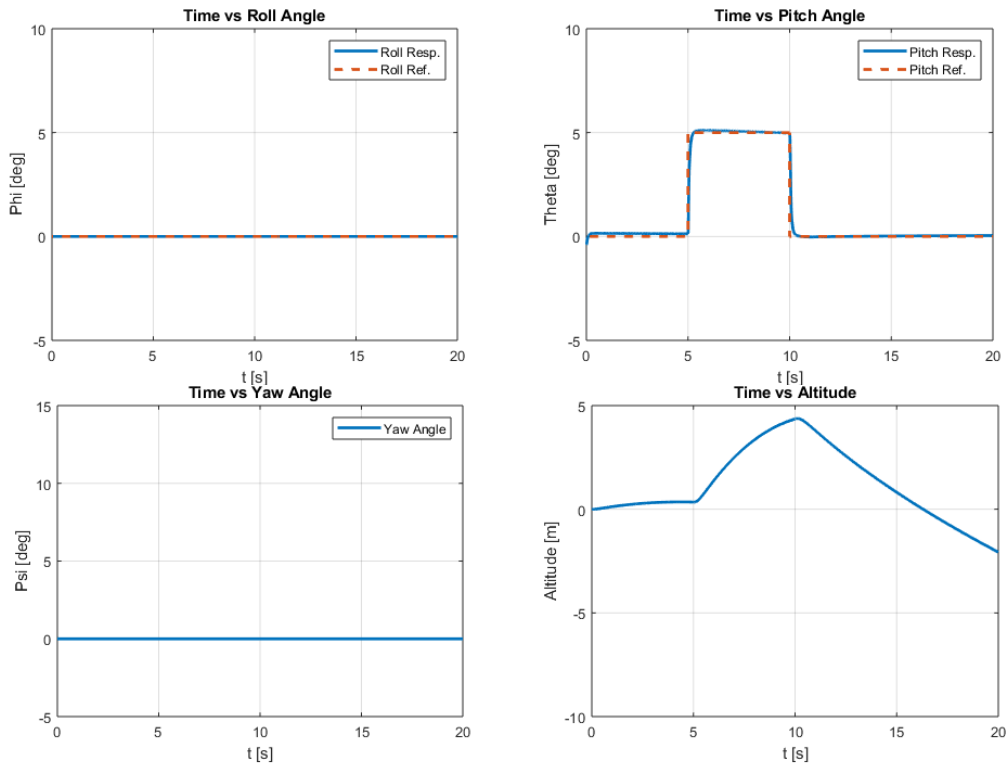


Figure 5.23. Pitch response with no propulsion with PD controllers

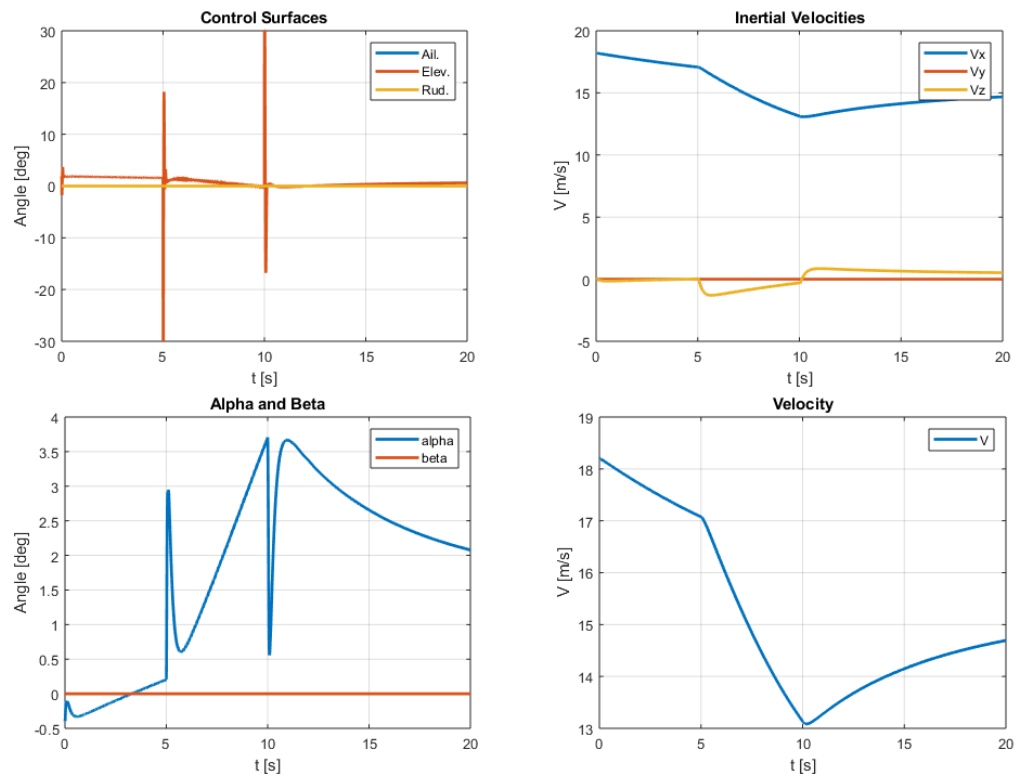


Figure 5.24. Pitch response with no propulsion with PD controllers

5.6.3 Transition Flight Simulations

In this part, the vehicle is simulated while it is transitioning from hover flight to forward flight from the trim condition at a height. In order to perform transition, the following methodology is used. First, front tilting rotors are tilted 20 degrees from trimmed hover flight. Due to the tilted rotors, an amount of force in body x -direction is generated and the vehicle starts to accelerate. The attitude of the hybrid vehicle is tried to be kept fixed without assigning it a pitch attitude. When the vehicle speeds up and reach a flight speed of 15 m/s which is below the trimmed cruising speed of 18.2 m/s, then the tilting rotors are tilted all at once (and the rear rotor is switched off) and a required amount of throttle is applied to speed up the vehicle to its cruising speed. In this way, forward transition from hover to forward flight is performed. While transitioning, two flight controllers, multicopter and fixed-wing controllers work simultaneously and signals that output from the controllers are multiplied by controller effectiveness factor which is a function of the mean tilt angle. As the vehicle starts to tilt front rotors, the fixed-wing controller is activated and its weight is increased from 0 to 1 as mean tilt angle is increased from 0 to 90 degrees.

As it seen from the simulation results given below, there are small disturbances in attitude due to transition which results from diverging from the trim conditions. However, this disturbance is decreased and smoothed by piecewise gain scheduling.

Also, aerodynamical angles alpha and beta given in Figure 5.27 are nonsensical at the beginning of the simulation. It is because, they are calculated by taking ratio of the body velocities at very slow speed values. As the total velocity increases, these parameters come to sensible values.

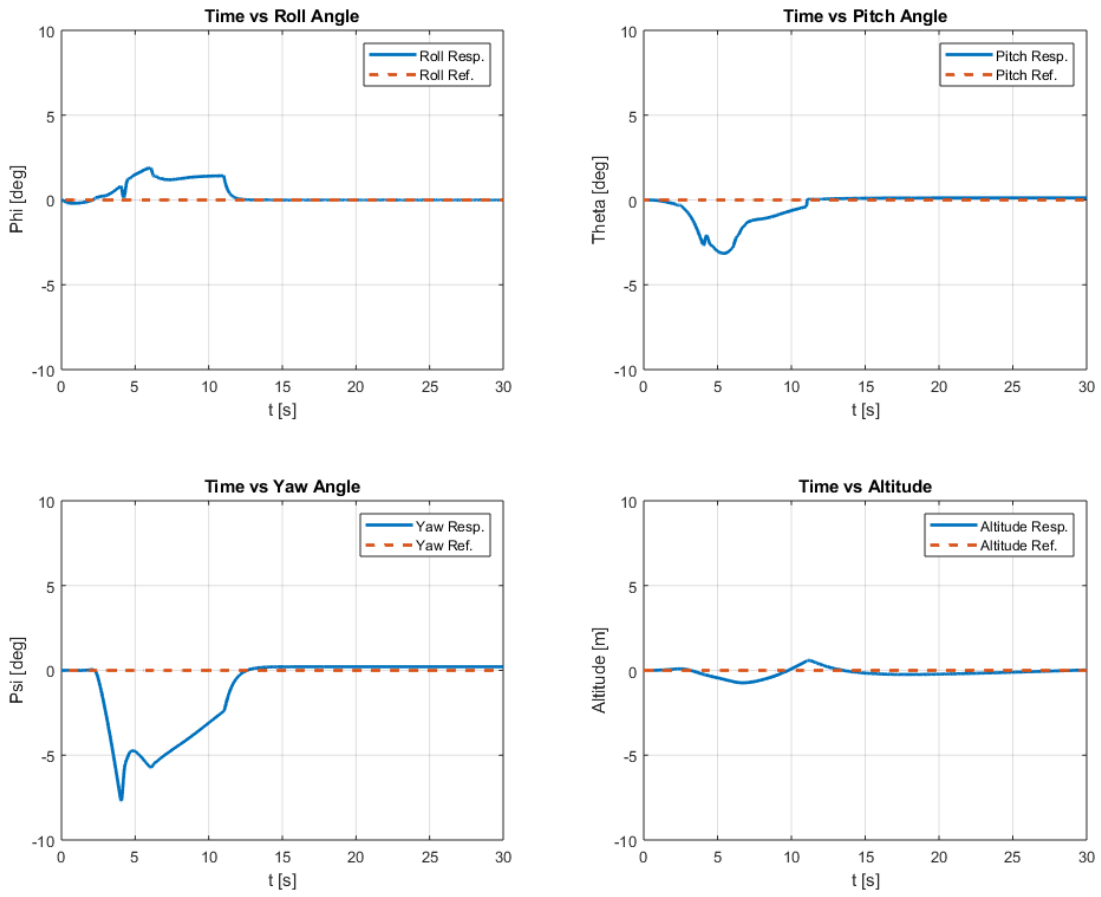


Figure 5.25. Attitude and altitude results for forward transition

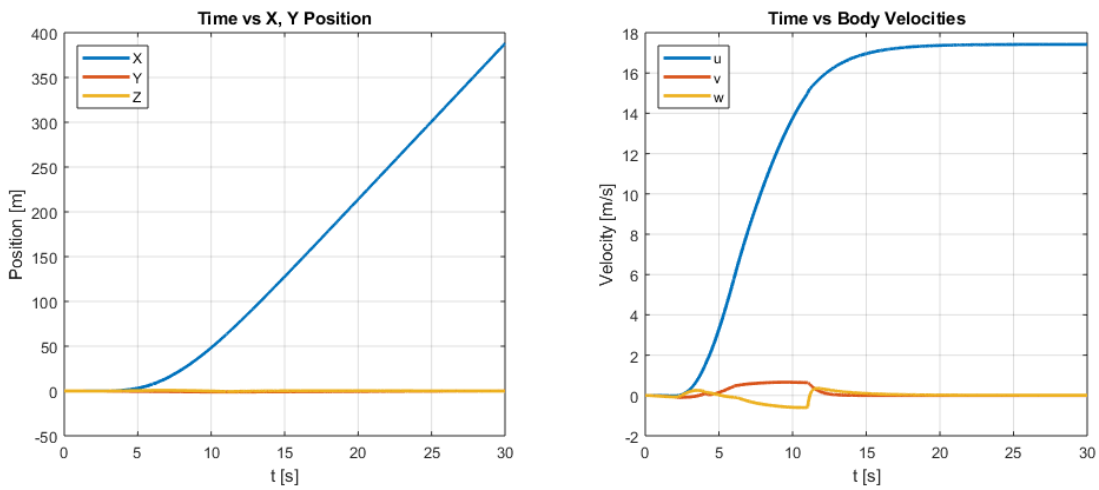


Figure 5.26. Position and velocity results for forward transition

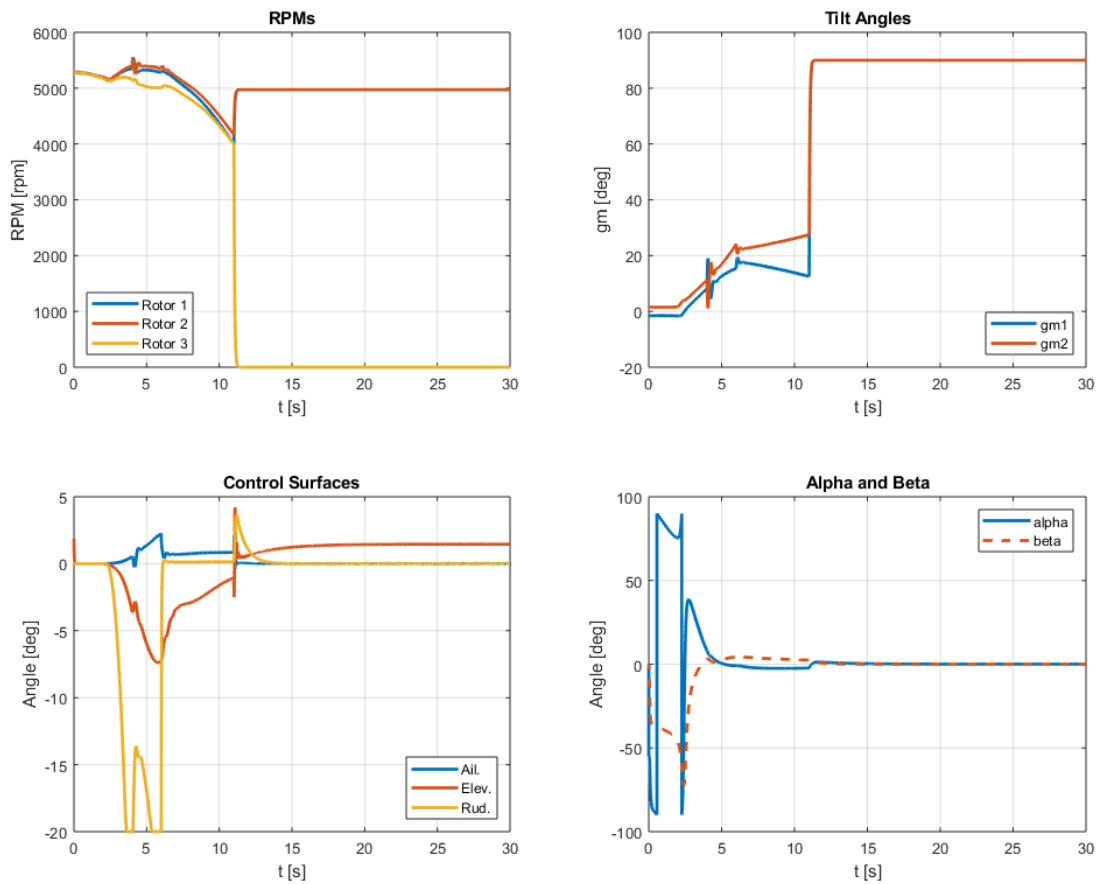


Figure 5.27. Actuator and aerodynamic angle results for forward transition

The back-transition simulation results from forward to hover flight is presented in Figures 5.28 – 5.30. Back-transition starts with tilting mean tilt angle from 90 to 20 degrees suddenly and then to 0 degrees gradually in 4 seconds. The vehicle starts to slow down from the cruising speed and when the speed drops down to 15 m/s, the vehicle performs a breaking action by pitching up a required amount. The pitch up command is controlled by another outer controller. At the end of back-transition the vehicle reaches to hover flight stage. Again, like in the previous case, both controllers are active and weighted by the controller effectiveness factor which is a function of the mean tilt angle of the front two rotors. Also, the controller gains are scheduled with respect to the mean tilt angle. Although, the roll, yaw angles and the altitude are slightly disturbed the results are satisfactory.

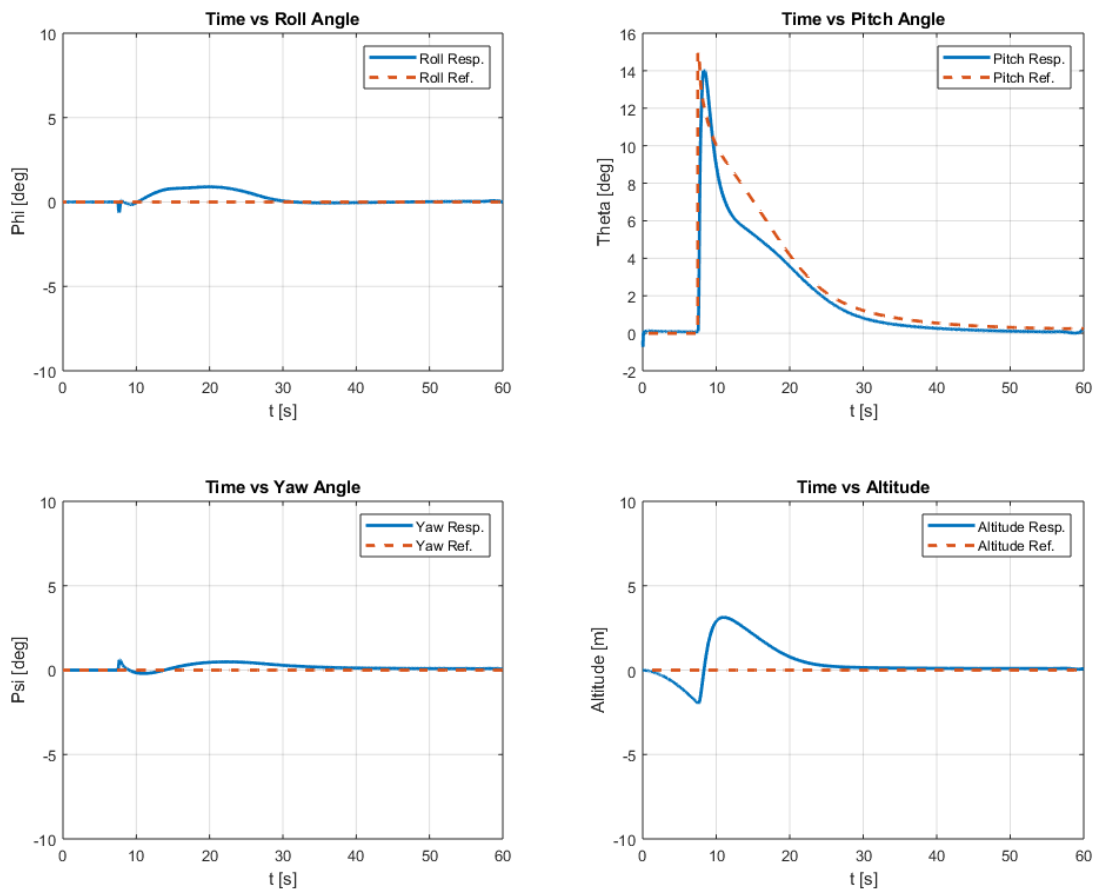


Figure 5.28. Attitude and altitude results for back-transition

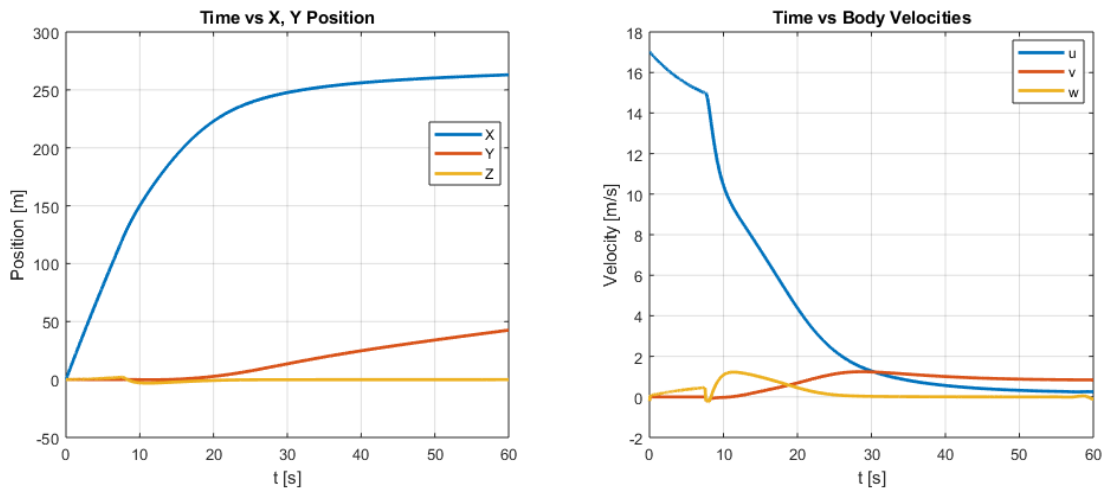


Figure 5.29. Position and velocity results for back-transition

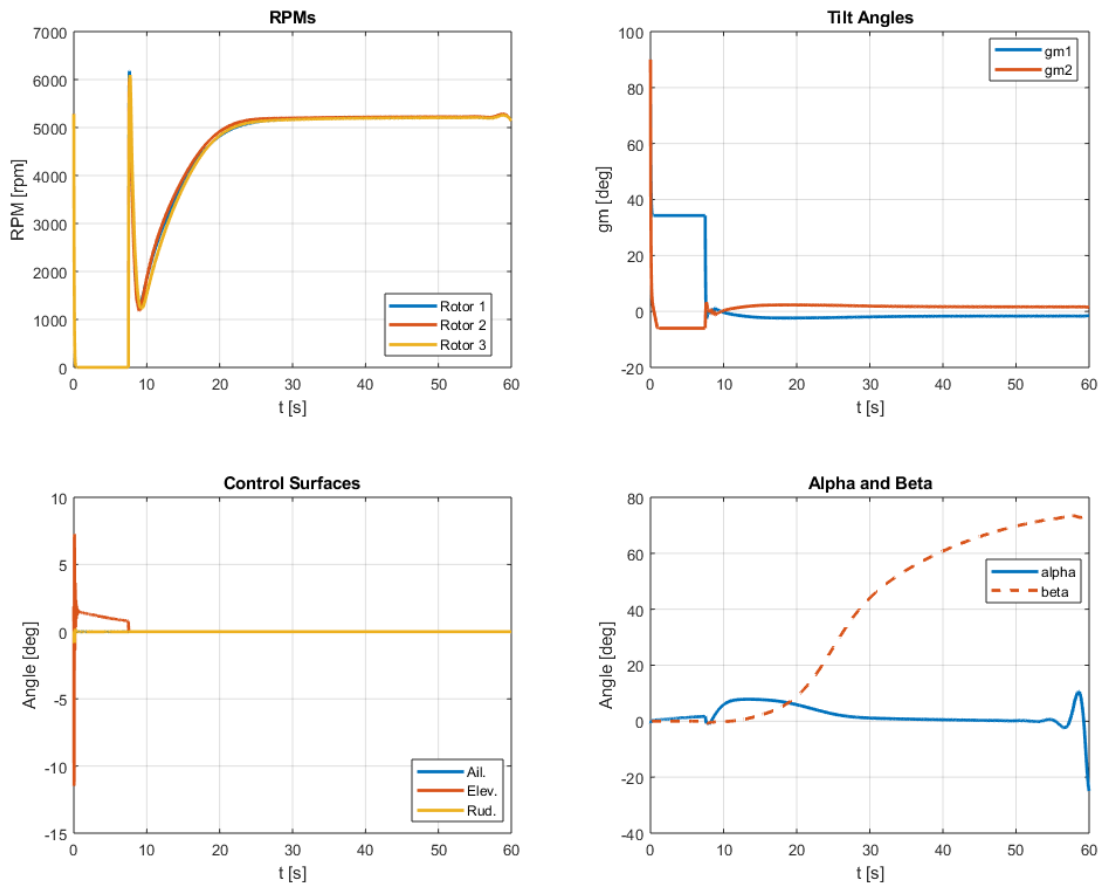


Figure 5.30. Actuator and aerodynamic angle results for back-transition

CHAPTER 6

CONCLUSION

In the thesis, a novel tiltrotor tricopter hybrid UAV with a fixed-wing structure is designed. The hybrid UAV is capable of vertically take-off and land beside the forward flight capability. For transitioning from VTOL to forward flight, front rotors are tilted. A mathematical nonlinear dynamic model of the vehicle including aerodynamic and propulsive parts is derived. For aerodynamic part, the model is obtained by extracting aerodynamic coefficient, stability and control derivatives of the vehicle using a VLM/3D panel method simulation software.

To analyze stability and to develop linear controllers, the vehicle is trimmed for individual flight phases. Then linearization of the nonlinear system is performed at the specified trim points. Thereafter, state space model of the linear system is provided. Various types of controllers are developed by using linearized system. PID, LQR and LQT linear controllers are developed and compared for multicopter and fixed-wing flight modes. A control mixer is developed and utilized to weight the controllers during transition and activate/deactivate them according to the flight mode of the vehicle.

The designed and modeled system is built in Simulink. Nonlinear vehicle dynamics are simulated and analyzed for given reference commands for hover and forward flight modes. In addition, transitioning between flight modes are simulated and results are presented.

Hybrid UAVs that are capable of vertical takeoff and landing, are in a promising position today and further studies are needed to thrive hybrid aerial vehicles. In this thesis, we studied design, modeling, control and simulation of a hybrid UAV.

Although, the designed controllers in this thesis are not used (since it requires advanced coding knowledge and due to time limitations), the designed and built hybrid vehicle is validated by using an open-source autopilot (PX4). First, since the designed tilt-rotor tricopter airframe with a fixed-wing module is not available in the autopilot software, several script files are written and implemented to the software to define the airframe. After, the flight tests were performed successfully including the vertical take-off, hover, transition forward flight with fixed-wing mode, back-transition and vertical landing stages. The flight data are presented in the appendix.

REFERENCES

- [1] Nonami, K., Kendoul, F., Suzuki, S., Wang, W., & Nakazawa, D. (2010). Introduction. In *Autonomous flying robots: unmanned aerial vehicles and micro aerial vehicles* (pp. 1-29). Springer Science & Business Media.
- [2] Hassanalian, M., & Abdelkefi, A. (2017). Classifications, applications, and design challenges of drones: A review. *Progress in Aerospace Sciences, 91*, 99-131.
- [3] Summers, A. W. (2017). *Modeling and Control of a Fixed Wing Tilt-Rotor Tri-Copter* (Ph.D.), University of Washington.
- [4] Turkish Aerospace, *Anka*. Retrieved from: <https://www.tai.com.tr/urun/anka>. [Accessed January 2018].
- [5] Dassault Aviation, *Neuron*. Retrieved from: <https://www.dassault-aviation.com/en/group/2017-paris-air-show/illustrated-news/neuron-fcas-male/> [Accessed January 2018].
- [6] Northrop Grumman, MQ-8B. Retrieved from: <http://www.northropgrumman.com/Capabilities/MQ8BFireScout/Pages/default.aspx>. [Accessed January 2018].
- [7] DPI UAV Systems, DP-14 Hawk. Retrieved from: <http://www.dragonflypictures.com/products/unmanned-vehicles/dp-14-hawk>. [Accessed January 2018].
- [8] DJI, Phantom. Retrieved from: https://www5.djicdn.com/cms_uploads/video/image/3072/cover_365x219_phantom-3-standard-intro.jpg. [Accessed January 2018].
- [9] Festo, Smartbird. Retrieved from: <https://www.festo.com/group/en/repo/assets/6874-smartbird-2140x940px.jpg>. [Accessed January 2018].

- [10] Korean Aerospace Research Institute, TR-60. Retrieved from: <http://www.businesskorea.co.kr/news/articleView.html?idxno=10176>. [Accessed January 2018].
- [11] Northrop Grumman, LEMV. Retrieved from: http://www.northropgrumman.com/Photos/pgL_LM-10025_004.jpg. [Accessed January 2018].
- [12] AeroVel Corporation, Flexrotor. Retrieved from: http://aerovel.com/wp-content/uploads/2015/01/IMG_3626.jpg. [Accessed January 2018].
- [13] Arcturus UAV, Jump20. Retrieved from: http://arcturus-uav.com/sites/default/files/styles/grid_image/public/hometrio/JUMP_AirV%20Teaser.jpeg?itok=9eGrkFio. [Accessed January 2018].
- [14] NASA, GL-10. Retrieved from: <https://www.nasa.gov/sites/default/files/thumbnails/image/gl10-hover-02.jpg>. [Accessed June 2018].
- [15] Bell Textron Inc., Eagle Eye. Retrieved from: <https://www.naval-technology.com/wp-content/uploads/sites/5/2017/09/1-Image-01-29.jpg>. [Accessed September 2019].
- [16] Saeed, A. S., Younes, A. B., Islam, S., Dias, J., Seneviratne, L., & Cai, G. (2015). A review on the platform design, dynamic modeling and control of hybrid UAVs. In *Unmanned Aircraft Systems (ICUAS), 2015 International Conference on* (pp. 806-815). IEEE.
- [17] Zhao, H., & Bil, C. (2008). Aerodynamic design and analysis of a VTOL ducted-fan UAV. In *26th AIAA Applied Aerodynamics Conference* (p. 7516).
- [18] Matsumoto, T., Kita, K., Suzuki, R., Oosedo, A., Go, K., Hoshino, Y., Konno A. & Uchiyama, M. (2010). A hovering control strategy for a tail-sitter VTOL UAV that increases stability against large disturbance. In *2010 IEEE international conference on robotics and automation* (pp. 54-59). IEEE.
- [19] Kubo, D., & Suzuki, S. (2008). Tail-sitter vertical takeoff and landing unmanned aerial vehicle: transitional flight analysis. *Journal of Aircraft*, 45(1), 292-297.

- [20] Hochstenbach, M., Notteboom, C., Theys, B., & De Schutter, J. (2015). Design and control of an unmanned aerial vehicle for autonomous parcel delivery with transition from vertical take-off to forward flight—vertikal, a quadcopter tailsitter. *International Journal of Micro Air Vehicles*, 7(4), 395-405.
- [21] Hochstenbach, M., Notteboom, C., Theys, B., & De Schutter, J. (2015). Design and control of an unmanned aerial vehicle for autonomous parcel delivery with transition from vertical take-off to forward flight—vertikal, a quadcopter tailsitter. *International Journal of Micro Air Vehicles*, 7(4), 395-405.
- [22] Latitude Engineering. Hybrid Quadrotor Technology. Retrieved from <https://www.latitudeengineering.com/products/hq/>. [Accessed June 2019].
- [23] Krossblade Aerospace. SkyPowler 2. Retrieved from <https://www.krossblade.com/#skypowler-section>. [Accessed June 2019].
- [24] ALTI Company, Transition. Retrieved from <https://www.altiuas.com/transition>. [Accessed June 2019].
- [25] Liu, Z., He, Y., Yang, L., & Han, J. (2017). Control techniques of tilt rotor unmanned aerial vehicle systems: A review. *Chinese Journal of Aeronautics*, 30(1), 135-148.
- [26] Dickeson, J. J., Mix, D. R., Koenig, J. S., Linda, K. M., Cifdaloz, O., Wells, V. L., & Rodriguez, A. A. (2005, December). H_∞ hover-to-cruise conversion for a tilt-wing rotorcraft. In *Proceedings of the 44th IEEE Conference on Decision and Control* (pp. 6486-6491). IEEE.
- [27] Holsten, J., Ostermann, T., & Moormann, D. (2011). Design and wind tunnel tests of a tiltwing UAV. *CEAS Aeronautical Journal*, 2(1-4), 69-79.
- [28] Çetinsoy, E., Dikyar, S., Hançer, C., Oner, K. T., Sirimoglu, E., Unel, M., & Aksit, M. F. (2012). Design and construction of a novel quad tilt-wing UAV. *Mechatronics*, 22(6), 723-745.
- [29] Wikimedia Foundation Inc, Bell Eagle Eye TR911X. https://en.wikipedia.org/wiki/Bell_Eagle_Eye. [Accessed June 2019].

- [30] Korean Aerospace Research Institute, TR-60 and TR-100. https://www.kari.re.kr/eng/sub03_01_01.do. [Accessed June 2019].
- [31] Bell Textron Inc., Eagle Eye. Retrieved from: <https://www.flightglobal.com/news/articles/new-search-for-vtol-uavs-may-resurrect-bell-tiltroto-421075>. [Accessed September 2019].
- [32] Korean Aerospace Research Institute, TR-100. Retrieved from: https://www.kari.re.kr/eng/kariimg/view.do?idx=855&pageIndex=1&siteCode=eng&mno=sub05_01&img_gbn=PHO&img_tp=A. [Accessed June 2019].
- [33] Carlson, S. (2014). A hybrid tricopter/flying-wing vtol uav. In *52nd Aerospace Sciences Meeting* (p. 0016).
- [34] Ozdemir, U., Aktas, Y. O., Vuruskan, A., Dereli, Y., Tarhan, A. F., Demirbag, K., Erdem, A., Kalaycioglu, G.D. & Inalhan, G. (2014). Design of a commercial hybrid VTOL UAV system. *Journal of Intelligent & Robotic Systems*, 74(1-2), 371-393.
- [35] Vuruskan, A., Yuksek, B., Ozdemir, U., Yukselen, A., & Inalhan, G. (2014). Dynamic modeling of a fixed-wing VTOL UAV. In *2014 International Conference on Unmanned Aircraft Systems (ICUAS)* (pp. 483-491). IEEE.
- [36] Aktas, Y. O., Ozdemir, U., Dereli, Y., Tarhan, A. F., Cetin, A., Vuruskan, A., Yuksek, B., Cengiz, H., Basdemir, S., Ucar, M., Genctav, M., Yukselen, A., Ozkol, A., Kaya, M. O. & Genctav, M. (2014). A low cost prototyping approach for design analysis and flight testing of the turac vtol uav. In *2014 International Conference on Unmanned Aircraft Systems (ICUAS)* (pp. 1029-1039). IEEE.
- [37] Collins, N. S. (2016). *System Design and Nonlinear State-dependent Riccati Equation Control of an Autonomous Y-4 Tilt-rotor Aerobot for Martian Exploration* (Doctoral dissertation, University of Surrey).
- [38] Underwood, C., & Collins, N. (2017). Design and Control of a Y-4 Tilt-Rotor VTOL Aerobot for Flight on Mars. In *Proceedings of the 68th International Astronautical Congress (IAC)*. International Astronautical Federation (IAF).

- [39] BirdsEyeView Aerobotics, FireFly6 Pro. <https://www.birdseyeview.aero/>. [Accessed June 2019].
- [40] Ozdemir, U., Aktas, Y. O., Vuruskan, A., Dereli, Y., Tarhan, A. F., Demirbag, K., Erdem, A., Kalaycioglu, G. D., Ozkol I. & Inalhan, G. (2014). TURAC Preliminary Design. *Journal of Intelligent & Robotic Systems*, 74(1-2), 371-393
- [41] Underwood, C., & Collins, N. (2017). Hyperion II “Y4TR” Mars VTOL Aerobot. In *Proceedings of the 68th International Astronautical Congress (IAC)*. International Astronautical Federation (IAF).
- [42] BirdsEyeView Aerobotics, Firefly6. Retrieved from: <https://www.birdseyeview.aero/products/firefly6>. [Accessed June 2019].
- [43] Armutcuoglu, O., Kavsaoglu, M. S., & Tekinalp, O. (2004). Tilt duct vertical takeoff and landing uninhabited aerial vehicle concept design study. *Journal of aircraft*, 41(2), 215-223.
- [44] Onen, A. S., Cevher, L., Senipek, M., Mutlu, T., Gungor, O., Uzunlar, I. O., Kurtulus, D. F., & Tekinalp, O. (2015). Modeling and controller design of a VTOL UAV. In *2015 International Conference on Unmanned Aircraft Systems (ICUAS)* (pp. 329-337). IEEE.
- [45] Önen, A. S. (2015). Modeling and controller design of a VTOL air vehicle. *METU, M. Sc. thesis, Ankara*.
- [46] Papachristos, C., Alexis, K., & Tzes, A. (2012). Towards a high-end unmanned tri-tiltrotor: Design, modeling and hover control. In *2012 20th Mediterranean Conference on Control & Automation (MED)* (pp. 1579-1584). IEEE.
- [47] Papachristos, C., Alexis, K., & Tzes, A. (2013). The UPAT Tri-TiltRotor experimental platform. In *2013 IEEE International Conference on Robotics and Automation* (pp. 5425-5432). IEEE.
- [48] Onen, A. S., Cevher, L., Senipek, M., Mutlu, T., Gungor, O., Uzunlar, I. O., Kurtulus, D. F., & Tekinalp, O. (2015). Modeling and controller design of a

- VTOL UAV. In *2015 International Conference on Unmanned Aircraft Systems (ICUAS)* (pp. 329-337). IEEE.
- [49] Wikimedia Foundation, Inc. IAI Panther. https://en.wikipedia.org/wiki/IAI_Panther. [Accessed June 2019].
- [50] Chen, C., Zhang, J., Zhang, D., & Shen, L. (2017). Control and flight test of a tilt-rotor unmanned aerial vehicle. *International Journal of Advanced Robotic Systems*, *14*(1), 1729881416678141.
- [51] Carlson, S. (2014). A hybrid tricopter/flying-wing vtol uav. In *52nd Aerospace Sciences Meeting* (p. 0016).
- [52] Chao, C., Lincheng, S., Daibing, Z., & Jiyang, Z. (2016). Mathematical modeling and control of a tiltrotor UAV. In *2016 IEEE International Conference on Information and Automation (ICIA)*. IEEE.
- [53] Monterroso, A. (2018). *Preliminary Sizing, Flight Test, and Performance Analysis of Small Tri-Rotor VTOL and Fixed-Wing UAV* (Doctoral dissertation, San Diego State University).
- [54] Ta, D. A., Fantoni, I., & Lozano, R. (2012). Modeling and control of a tilt tri-rotor airplane. In *2012 American control conference (ACC)* (pp. 131-136). IEEE.
- [55] Carlson, S. (2014). The completed vehicle, dubbed the “Orange Hawk”. In *52nd Aerospace Sciences Meeting* (p. 0016).
- [56] Chao, C., Lincheng, S., Daibing, Z., & Jiyang, Z. (2016). Tilt-Rotor UAV prototype view. In *2016 IEEE International Conference on Information and Automation (ICIA)*. IEEE.
- [57] Monterroso, A. (2018). UAV layout and configuration. *Preliminary Sizing, Flight Test, and Performance Analysis of Small Tri-Rotor VTOL and Fixed-Wing UAV*

- [58] How, J. P., Frazzoli, E., & Chowdhary, G. V. (2015). Linear flight control techniques for unmanned aerial vehicles. *Handbook of Unmanned Aerial Vehicles*, 529-576.
- [59] Kendoul, F., Fantoni, I., & Lozano, R. (2006). Modeling and control of a small autonomous aircraft having two tilting rotors. *IEEE Transactions on Robotics*, 22(6), 1297-1302.
- [60] Chowdhury, A. B., Kulhare, A., & Raina, G. (2012). Back-stepping control strategy for stabilization of a tilt-rotor uav. In *2012 24th Chinese Control and Decision Conference (CCDC)*(pp. 3475-3480). IEEE.
- [61] Chowdhury, A. B., Kulhare, A., & Raina, G. (2012). A generalized control method for a Tilt-rotor UAV stabilization. In *2012 IEEE International Conference on Cyber Technology in Automation, Control, and Intelligent Systems (CYBER)* (pp. 309-314). IEEE.
- [62] Flores-Colunga, G. R., & Lozano-Leal, R. (2014). A nonlinear control law for hover to level flight for the quad tilt-rotor uav. *IFAC Proceedings Volumes*, 47(3), 11055-11059
- [63] Öner, K. T., Çetinsoy, E., Sırımoğlu, E., Hancer, C., Ayken, T., & Ünel, M. (2009). LQR and SMC stabilization of a new unmanned aerial vehicle.
- [64] Kim, B. M., Choi, K. C., & Kim, B. S. (2007). Trajectory tracking controller design using neural networks for tiltrotor UAV. In *AIAA Guidance, Navigation and Control Conference and Exhibit* (p. 6460).
- [65] Fang, X., Lin, Q., Wang, Y., & Zheng, L. (2012). Control strategy design for the transitional mode of tiltrotor UAV. In *IEEE 10th International Conference on Industrial Informatics* (pp. 248-253). IEEE.
- [66] Sato, M., & Muraoka, K. (2014). Flight controller design and demonstration of quad-tilt-wing unmanned aerial vehicle. *Journal of guidance, control, and dynamics*, 38(6), 1071-1082.

- [67] Muraoka, K., Okada, N., Kubo, D., & Sato, M. (2012). Transition flight of quad tilt wing VTOL UAV. In *28th Congress of the International Council of the Aeronautical Sciences* (pp. 2012-11).
- [68] Papachristos, C., Alexis, K., & Tzes, A. (2013). Model predictive hovering-translation control of an unmanned tri-tiltrotor. In *2013 IEEE International Conference on Robotics and Automation* (pp. 5425-5432). IEEE.
- [69] Hernandez-Garcia, R. G., & Rodriguez-Cortes, H. (2015). Transition flight control of a cyclic tiltrotor uav based on the gain-scheduling strategy. In *2015 International Conference on Unmanned Aircraft Systems (ICUAS)* (pp. 951-956). IEEE.
- [70] Papachristos, C., Alexis, K., & Tzes, A. (2011). Design and experimental attitude control of an unmanned tilt-rotor aerial vehicle. In *2011 15th International Conference on Advanced Robotics (ICAR)* (pp. 465-470). IEEE.
- [71] Papachristos, C., & Tzes, A. (2012). Modeling and control simulation of an unmanned tilt tri-rotor aerial vehicle. In *2012 IEEE International Conference on Industrial Technology* (pp. 840-845). IEEE.
- [72] Çetinsoy, E., Dikyar, S., Hançer, C., Oner, K. T., Sirimoglu, E., Unel, M., & Aksit, M. F. (2012). Design and construction of a novel quad tilt-wing UAV. *Mechatronics*, 22(6), 723-745.
- [73] Oner, K. T., Cetinsoy, E., Unel, M., Aksit, M. F., Kandemir, I., & Gulez, K. (2008). Dynamic model and control of a new quadrotor unmanned aerial vehicle with tilt-wing mechanism. *World Academy of Science, Engineering and Technology*, 45.
- [74] Papachristos, C., Alexis, K., & Tzes, A. (2013). Linear quadratic optimal trajectory-tracking control of a longitudinal thrust vectoring-enabled unmanned Tri-TiltRotor. In *IECON 2013-39th Annual Conference of the IEEE Industrial Electronics Society* (pp. 4174-4179). IEEE.

- [75] Anderson, J. D. (1999). *Aircraft performance and design*. McGraw-Hill Science/Engineering/Math.
- [76] Raymer, D. (2018). *Aircraft design: a conceptual approach*. American Institute of Aeronautics and Astronautics, Inc.
- [77] Selig, M. (2003). Low Reynolds number airfoil design lecture notes. *VKI Lecture Series, November, 24-28*.
- [78] Selig, M. S. (Ed.). (1995). *Summary of low speed airfoil data* (Vol. 3). SoarTech
- [79] Etkin, B. (2012). *Dynamics of atmospheric flight*. Courier Corporation.
- [80] Großekathöfer, K., & Yoon, Z. (2012). Introduction into quaternions for spacecraft attitude representation. *TU Berlin, 16*.
- [81] T-Motor, MN5212 KV420 motor & 15x5CF test data. Retrieved from: <http://store-en.tmotor.com/goods.php?id=378>. [Accessed January 2018].
- [82] METU, METUWIND, C3 Wind Tunnel. Retrieved from: <https://ruzgem.metu.edu.tr/en/experimental-aerodynamics-laboratory>. [Accessed July 2019].
- [83] Deperrois, A. (2009). About XFLR5 calculations and experimental measurements. *XFLR5 Documentation, October*.
- [84] Deperrois, A. (2011). Modal analysis and experimental validation.
- [85] Yüksek, B. (2013). *Sabit Kanatlı Bir İnsansız Hava Aracının Modellenmesi Ve Kontrolü* (Master thesis, Fen Bilimleri Enstitüsü).
- [86] Roskam, Jan. *Airplane flight dynamics and automatic flight controls*. DARcorporation, 1998.
- [87] Etkin, B., & Reid, L. D. (1996). *Dynamics of flight: Stability and control*. New York: Wiley.
- [88] Ogata, K. (2009). *Modern Control Engineering* (pp. 6142-6143). Upper Saddle River, NJ: Prentice Hall.

APPENDICES

A. Flight Testing

In this thesis a tilt-rotor tricopter with a conventional fixed-wing airframe UAV is designed. The designed UAV is manufactured in the workplaces of METU Aerospace Engineering department. In order to make flight tests of the developed hybrid design, first, a verified autopilot software should be used on the vehicle. After, new control algorithms could be developed and implemented to the used autopilot software. For this purpose, an open source autopilot software PX4 is chosen to make preliminary flight tests and thereafter, to design and implement control algorithms. Since this condition requires high coding experience, we leave this as a future work to update and develop controller algorithms for the software and to make new flight tests with the integrated control algorithms.

Unfortunately, the designed airframe (tilt-rotor tricopter with two tilting front rotors and a fixed rear rotor combined with a conventional airplane airframe) was not defined in the software. Thus, suitable configuration and mixer files were written and implemented into the PX4 software. In another words, a bridge between controller signals and the identified actuators were constructed. As an autopilot hardware, Pixhawk 2.1 (Cube) is used. The vehicle has GPS antenna and airspeed sensor for location and velocity measurements.

The flight tests were performed at the campus of METU, and the results are shown in the following figures. Despite to very windy weather the vehicle took off, cruised and landed successfully, including forward and back-transition stages. Unfortunately, there is a bias in airspeed readings so it gives less than real airspeed data. At the bottom side of the Figure A.2 – A.9, the blue region corresponds to multicopter (VTOL) mode, yellow region corresponds to fixed-wing mode and the pink region corresponds to the forward transition and back-transition stages. Some pictures from the flight test are presented in Figure A.10.



Figure A. 1. Flight path of the performed flight test

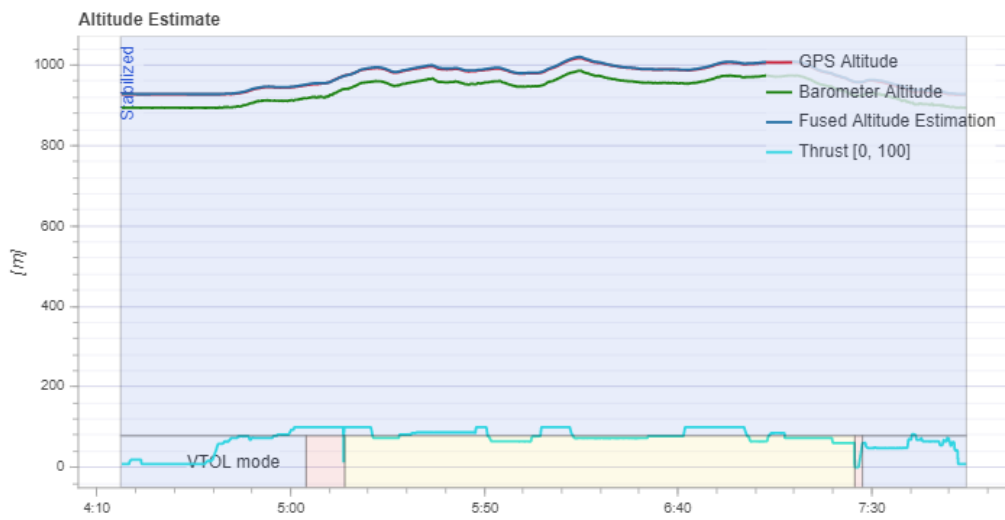


Figure A. 2. Altitude data



Figure A. 3. Roll angle variation

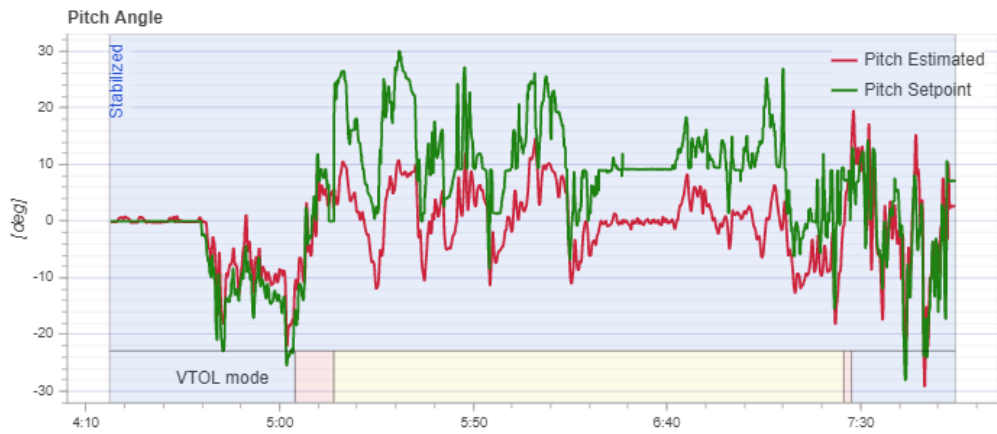


Figure A. 4. Pitch angle variation

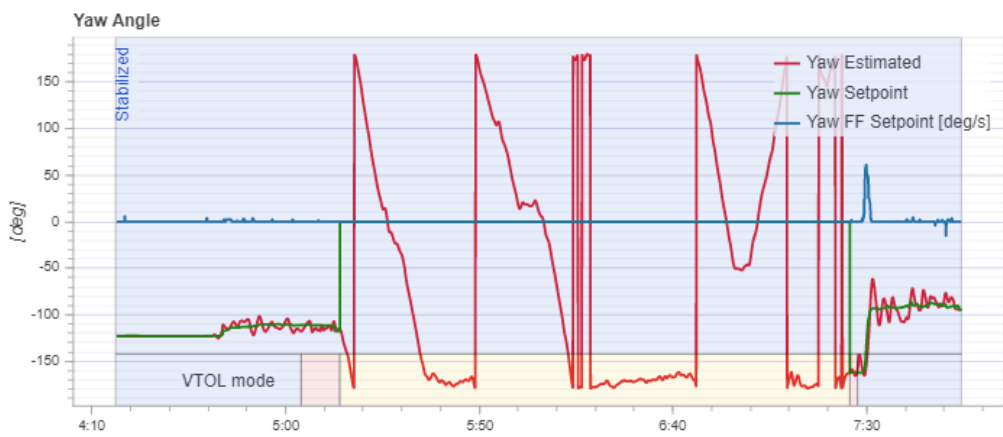


Figure A. 5. Yaw angle variation

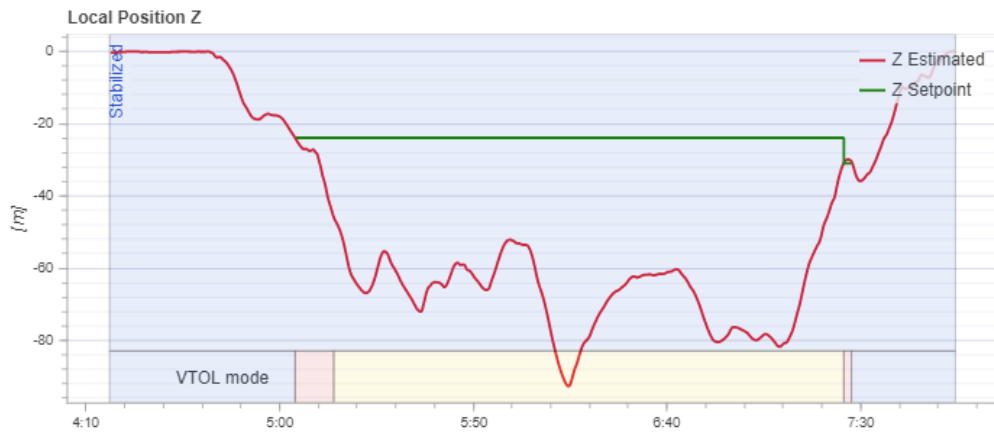


Figure A. 6. Data for the position in body z-axis



Figure A. 7. Variation of velocity in inertial axes

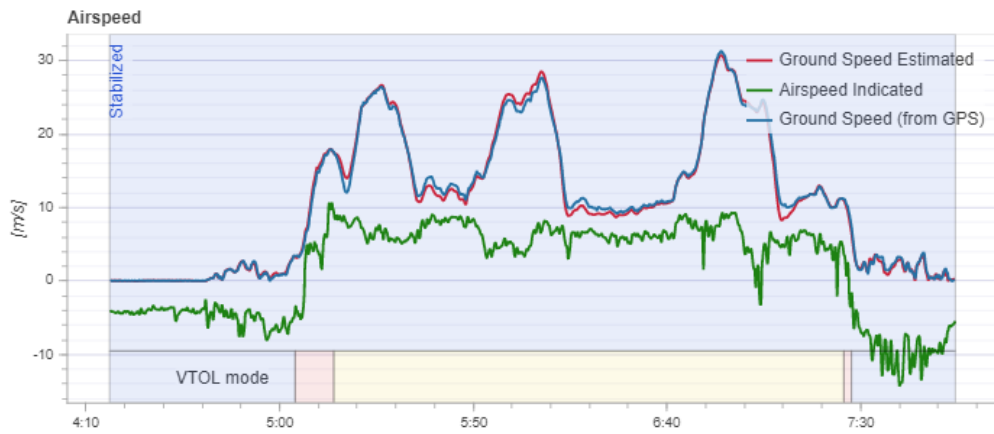


Figure A. 8. Variation of airspeed

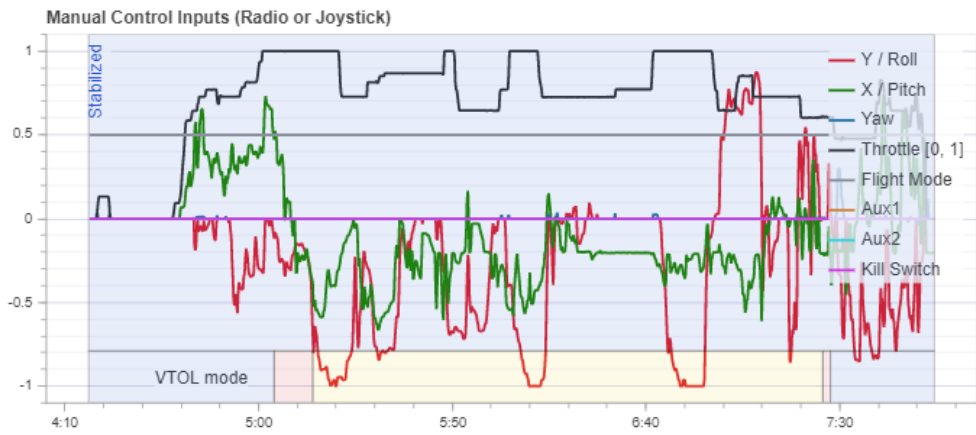


Figure A. 9. Pilot control commands sent by a remote controller



Figure A. 10. Pictures from flight test